7

The Design of DOAS Instruments

In recent years, a large variety of designs of active and passive DOAS systems (see Chaps. 6, 10, and 11) as well as of its optical, mechanical, electronic, and software subsystems were developed in response to the requirements of atmospheric research and monitoring. Many of the characteristics, design considerations, and trade-offs are common to several or all varieties of DOAS systems. In this chapter, we will describe the options and design criteria for the DOAS instrument, as well as for the required subsystems. In particular, we describe the various decisions that have to be made in design and operation procedures of a DOAS system, once the basic arrangement has been selected.

7.1 Design Considerations of DOAS Instruments

Obviously, the design of a particular DOAS system must be based on many requirements such as high sensitivity, spectral properties (resolution and spectral range), and practical aspects (cost, weight, and power consumption). In particular, the instrument must have the capability to detect very weak absorption features, as optical densities (see Chap. 6) around 10^{-3} are a typical signal. From the standpoint of intended application, we can identify the following requirements:

- Scientific (in situ) studies of atmospheric chemistry are frequently performed with ground-based active DOAS systems, although passive, in particular, multi-axis DOAS (MAX-DOAS) systems are gaining importance. Many scientific studies require high sensitivity (low detection limit), specific detection, and a large degree of flexibility (different light path lengths, wide range of species to be measured and thus a large accessible spectral range). Automated operation and simplicity of design is usually not a priority.
- Air pollution monitoring, and in particular long-term observations are, at present, usually performed with active DOAS systems.

U. Platt and J. Stutz, *The Design of DOAS Instruments*. In: U. Platt and J. Stutz, Differential Optical Absorption Spectroscopy, Physics of Earth and Space Environments, pp. 175–285 (2008)
DOI 10.1007/978-3-540-75776-4_7

Here, automated design, simple operation, and low cost are requirements. To some extent, this can be realised at the expense of outmost sensitivity and flexibility of the instrument.

- Monitoring of the stratospheric composition (e.g. as an 'early warning' system) for future changes, for instance by the 'network for detection of stratospheric change' (NDSC), is mostly performed by passive spectroscopy.
- Long-term (ground-based) studies of atmospheric gases require an automated design which needs little supervision. Thus, for the monitoring of stratospheric gases zenith scattered light (ZSL) (i.e. passive) DOAS is the method of choice. For tropospheric species active as well as passive instruments (e.g. MAX-DOAS) can be considered.
- Global and long-term observation of stratospheric and tropospheric trace gas distributions is achieved by satellite measurements, where the DOAS technique has been proven to lead to considerable progress, in particular with respect to the quantitative measurement of tropospheric species (e.g. Borrell et al., 2003). Naturally, unattended operation is a prerequisite for satellite instruments. But at the large data rates, rapid spectral evaluation can also be a challenge.

From a technical standpoint, the central aspects of any DOAS system can be summarised in the following groups.

1. Active or passive operation: Active systems can work in a wider spectral range (i.e. below 300 nm) and also in the absence of sunlight at night, but are relatively complex, both in technical design and logistic requirements. Passive instruments tend to require much simpler hardware (no light source, smaller telescope, etc.), but are usually restricted to operation during daylight hours.
2. The light throughput, i.e. the question how the amount of light reaching the detector can be maximised under the given boundary conditions: This is an important requirement due to the frequently low optical densities of trace gas absorption structures to be measured (see above). This, in turn, demands recording of the optical spectra at low noise levels, which are usually determined by photon noise. For active systems, the light throughput is determined by both light source and receiving optics. In passive systems only the latter can be optimised.
3. The spectral range observed, which determines the number of species to be observed: While a large spectral range is certainly of advantage, its selection will usually be a compromise because increasing the spectral range may affect spectral resolution. It may also be difficult to obtain a uniform signal throughout a large spectral range.
4. The spectral resolution, which should be sufficient to resolve the spectral structures to be observed: Again a compromise will have to be made. A better spectral resolution can improve the detection limit and the ability of the instrument to de-convolute overlapping bands of different species

(see Chap. 8); on the other hand, improvement of the resolution comes at the expense of light throughput and size (and therefore cost) of the instrumentation.

5. The spectral stability of the instrument: Since DOAS relies on the detection of weak absorptions, the instruments must have the capability to eliminate the effect of overlaying, stronger structures (due to Fraunhofer spectra, lamp emission spectra, or other atmospheric absorbers with strong, overlapping spectra) in the same wavelength range. If spectral shifts occur between the recording of the measurement spectrum and overlapping structures, e.g. the Fraunhofer reference, the performance in this area is degraded.

7.2 Key Components of DOAS Systems

Active instruments based on UV-visible absorption spectroscopy have been designed in a large variety of ways. For instance, broadband lasers were used as a light source (e.g. Rothe et al., 1974; Perner et al., 1976; Amerding et al., 1991; Dorn et al., 1993, 1996, 1998; Brauers et al., 1996, 1999; Brandenburger et al., 1998). However, the majority of the designs rely on arc lamps as light sources (e.g. Bonafe et al., 1976; Kuznetzov and Nigmatullina, 1977; Noxon et al., 1978, 1980; Platt, 1977; Platt et al., 1979; Platt and Perner, 1980, 1983; Johnston and McKenzie, 1984; Dorn and Platt 1986; Axelsson et al. 1990a,b, 1995; Plane and Smith 1995; Harder et al. 1997; Flentje et al., 1997; Allan et al., 1999, 2000; Geyer et al., 1999, 2001a,b,c; Hebestreit et al., 1999; Veitel et al., 2002; Yu et al., 2004; Saiz-Lopez et al., 2004a,b; Zingler and Platt, 2005). More details and examples are given in Chap. 10.

Passive instruments deriving trace gas column densities from the analysis of scattered or direct sunlight or direct moonlight have also been in wide use (e.g. Noxon, 1975; Bonafe et al., 1976; Kuznetzov and Nigmatullina, 1977; Millan, 1978, 1980; Noxon et al., 1978, 1980; Wagner, 1990; Burrows et al., 1999; Ferlemann et al., 1998, 2000; Pfeilsticker et al., 1999a,b; von Friedeburg et al., 2002, 2005; Wagner et al., 2002a,b,c; Galle et al., 2003; Bobrowski et al., 2003; Heckel, 2003; Heckel et al., 2005; Leser et al., 2003; Hönninger et al., 2004a,b,c; Wittrock et al. 2004; Heue et al. 2005; Lohberger et al. 2004; Wang et al. 2005). More details and examples are given in Chap. 11.

Depending on the particular type of application and desired measurement, a DOAS system consists of the following key components:

- Receiving optics (telescope)
- Spectrometer and connecting optics
- Detector, analogue-to-digital converter (ADC) and electronics
- Computer and auxiliary electronics
- Software for evaluation

- Database for absorption cross-sections of species (atoms or molecules) to be measured

In the case of artificial light source (active) DOAS, additional components are required:

- Artificial light source (lamp)
- Optics to arrange the light path (transmitting telescope, retro-reflector, or multi-reflection optics)

The components can be arranged in many different ways. For instance, a search-light type arrangement consisting of an artificial light source coupled to a transmitting telescope can project a light beam across a distance in the open atmosphere. The other end of the light path would be defined by a receiving telescope collecting (a usually small) part of the transmitted beam and transferring the light to a spectrometer coupled to a suitable detecting system. Details of the various possibilities are given in Sect. 7.9.

7.3 Light Sources for Active DOAS

To be suitable for DOAS applications, light sources must fulfill several important requirements:

1. Minimal spectral intensity variation [i.e. $I_0(\lambda) = \text{constant}$] is required, in particular at the scale of molecular vibrational bandwidths (i.e. around ≈1–10 nm see Chap. 6). In other words, the light sources should ideally emit 'white' light with a 'smooth' spectral characteristic.
2. As described earlier, the detection limit is improved if a large number of photons are recorded; thus, high intensity of the light source is required.
3. In active DOAS systems, the light has to be projected over a long path; therefore, a good beam collimation is required. For a thermal light source, this is equivalent to a request for high luminous intensity (high emitted power per unit area of the radiator and wavelength interval).
4. In particular, for long-term applications (e.g. in monitoring applications), long lifetime and low cost of light sources are also important.

Clearly, there is no ideal light source; thus, DOAS measurements are made using a variety of artificial light source types.

7.3.1 Characteristics of Artificial Light Sources

The advantage of artificial light sources is that they are always available, while sunlight, moonlight, or starlight can only be used under certain circumstances (day, full-moon, no cloud cover, etc.) and during certain periods of time. In addition, the useable spectral range of artificial light sources can extend further into the UV, as well as (in comparison to scattered light applications)

into the IR. For instance, light from extra-terrestrial sources that reaches the earth's surface always has to penetrate the ozone layer (see Chap. 2); thus, there will be virtually no intensity below 280 nm. Measurements with UV radiation at wavelengths as short as 200 nm can be made in the troposphere with suitable artificial light sources. On the other hand, the intensity of Rayleigh scattered sunlight for example as detected by ZSL–DOAS, becomes very small at near-IR wavelengths; thus, artificial light sources (or direct sunlight) can offer advantages in these situations. A summary of available light sources which have been used for DOAS applications and some of their properties is given in Table 7.1.

A basic distinction can be made between thermal light sources, such as incandescent lamps or arc lamps, and non-thermal light sources, such as light emitting diodes (LEDs), atomic emission lamps, fluorescent lamps, and laser light sources. Criteria for the selection of light sources are spectral brightness (W/unit of radiating area and wavelength interval) and spectral interval.

The radiation energy density $\rho(\nu, T)$ (in $\mathrm{J/m^3}$) as a function of frequency ν and temperature T in a cavity (Hohlraum) is given by:

$$\rho\ (\nu, \mathrm{T}) = \frac{8\pi\,\mathrm{h}\nu^3}{\mathrm{c}^3} \cdot \frac{\mathrm{d}\nu}{\mathrm{e}^{\mathrm{h}\nu/\mathrm{kT}} - 1}, \tag{7.1}$$

where h, k, and c denote Planck's and Boltzmann's constants and the speed of light, respectively. By substituting $\nu = \frac{c}{\lambda}$ and $d\nu = \frac{d\nu}{d\lambda} d\lambda = -\frac{c}{\lambda^2} d\lambda$, (7.1) can be converted into the corresponding wavelength-dependent expression:

$$\rho\,(\lambda, \mathrm{T}) = \frac{8\pi\ \mathrm{hc}}{\lambda^5} \cdot \frac{\mathrm{d}\lambda}{\mathrm{e}^{\mathrm{hc}/\lambda\mathrm{kT}} - 1}, \tag{7.2}$$

Table 7.1. Comparison of different light sources used for active DOAS applications

Type of lamp	Brightness	Typical input power W	Spectral range nm	Typical lifetime hours
High pressure Xe-Arc	High	75 to several 1000	<200–3000	200–2000
D-Arc	Medium	25	180–300	
Incandescent lamps	Low	10–500	300–3000	50–1000 depending on voltage
(Broadband) laser	Very high		<0.3 nm in a 200–3000 nm, interval	Dependent on type
Light emitting diodes (LED)	Low-medium	0.05–4.0	350[a] to several µm, certain wavelengths	>10000–100000

[a]Rapid technological advances towards lower wavelengths LEDs are being made.

Fig. 7.1 shows some examples of $\rho(\lambda)$ for cavities at different temperatures. For thermal emitters, the former quantity is essentially given by the Planck function, and thus the temperature T and the emissivity ε_{L} of the radiating area. The emissivity is unity for a perfect 'black body' i.e. an object that absorbs all incident light. Kirchhoff's law states:

$$\alpha_{\mathrm{L}}(\lambda) = \frac{\text{Radiation absorbed by the object}}{\text{Radiation incident on the object}} = \frac{\text{Radiation emitted by the object}}{\text{Radiation emitted by a black body}} = \varepsilon_{\mathrm{L}}(\lambda)\,. \tag{7.3}$$

Typical temperatures and emissivities are: $T \approx 3000\,\mathrm{K}$, $\varepsilon_{\mathrm{L}} = \varepsilon_{\mathrm{tung}} \approx 0.35$ for the tungsten filament of incandescent lamps and $T \approx 6000$–$10000\,\mathrm{K}$, $\varepsilon_{\mathrm{Xe}} \approx 0.03 \ldots 0.4$ for high pressure Xe arc lamps. Radiation energy density and radiation flux (in $\mathrm{W/m^2}$) from a surface are related by:

$$F_{\mathrm{p}}(\lambda, T) = \frac{\varepsilon_{\mathrm{L}} \cdot c}{4\pi} \cdot \rho(\lambda, T)\,. \tag{7.4}$$

This leads to the radiation flux from a radiating surface with the emissivity ε (from a lamp filament or arc) in units of $\mathrm{W/m^2}$, per steradian and wavelength interval $d\lambda$:

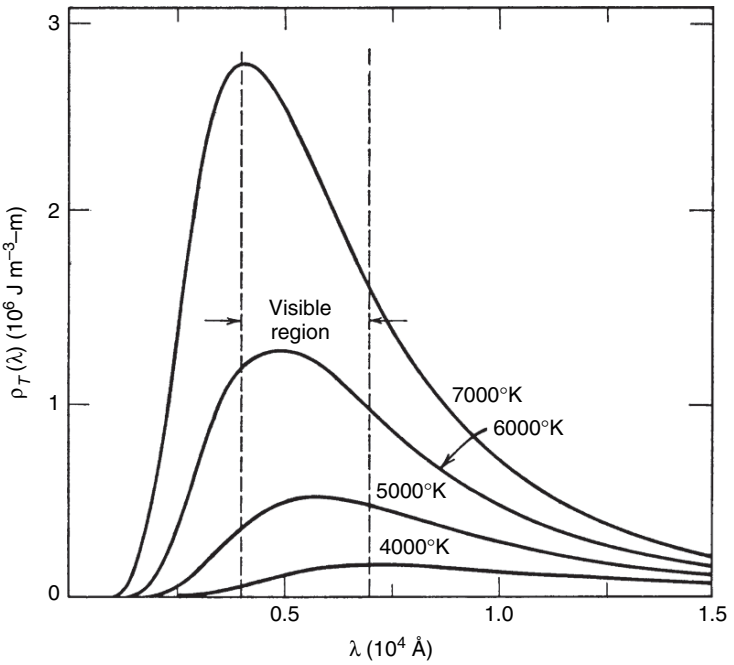

Fig. 7.1. Spectral intensity distributions of black bodies at 4000 K–7000 K (from Eisberg-Resnik, 1985)

$$F_p\ (\lambda, T) = \varepsilon_L \cdot \frac{2\,hc^2}{\lambda^5} \cdot \frac{d\lambda}{e^{hc/\lambda kT} - 1}, \tag{7.5}$$

or expressed as a function of ν in the frequency interval $d\nu$:

$$F_p\ (\nu, T) = \varepsilon_L \cdot \frac{2\,h\nu^3}{c^2} \cdot \frac{d\nu}{e^{h\nu/kT} - 1}. \tag{7.6}$$

Incandescent lamps are inexpensive, easy, and relatively safe to operate. The spectrum of incandescent lamps is very similar to that of a black-body radiator at 2800–3000 K, with a maximum in the near IR (1.0–2 µm, see Fig. 7.2). There is little emission in the UV below 400 nm. In practice, quartz–iodine lamps ('halogen lamps') are used because they reach somewhat higher filament temperatures and last longer than traditional incandescent lamps. However, the main advantage of quartz–iodine lamps for spectroscopy in the UV lies in the fact that their envelope is made of UV-transmitting quartz (as the name suggests). There is no problems with using quartz–iodine lamps of the type widely used for home illumination purposes, (if UV output is desired, care must taken that the lamps are not of the 'UV-protected' type). The output can be greatly increased by operating the lamps at 20–50% higher voltages than nominal, of course at the expense of a shortened lifetime (which normally

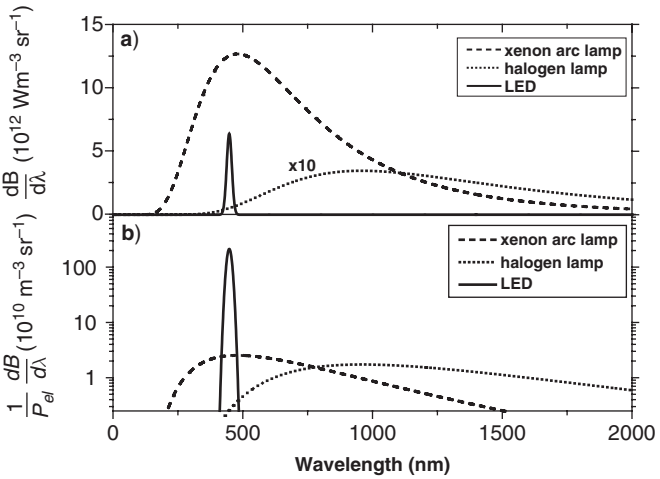

Fig. 7.2. Approximate intensity distributions of light sources. The **top panel** shows the spectral intensity distributions of three light sources: (1) An incandescent lamp (represented by a Planck's spectrum at $T = 3000$ K and an emissivity of $\varepsilon_{\text{tung}} = 0.35$). For clarity the intensity is multiplied by 10, (2) a Xenon-arc lamp (Osram XBO 450 W/2, represented by a Planck's spectrum at $T = 6000$ K and $\varepsilon_{\text{Xe}} = 0.4$), and (3) a LED (Luxeon LXHL-LR3C royal blue LED operated at 2.6 W electrical input power). **Bottom panel**: Same figures as above, intensity on a log scale and normalised to the electrical input power of the light sources (adapted from Kern et al., 2006)

is in the 50–1000 h range). In some cases, absorption lines due to I_2 were observed in quartz–iodine lamps (Senzig, 1995).

Since brightness is more important than total light flux, lamps of higher power than 20–50 W will be of no advantage. Higher-power lamps have larger radiating areas (i.e. filament sizes), but the emitted radiation per unit area stays the same.

Arc Lamps (Xenon and Deuterium): Due to their arc temperature ($T \approx 6000$–10000 K, $\varepsilon \approx 0.1$–0.4) being much higher than that of any filament, xenon-arc lamps (Fig. 7.3) have – compared to incandescent lamps – a much

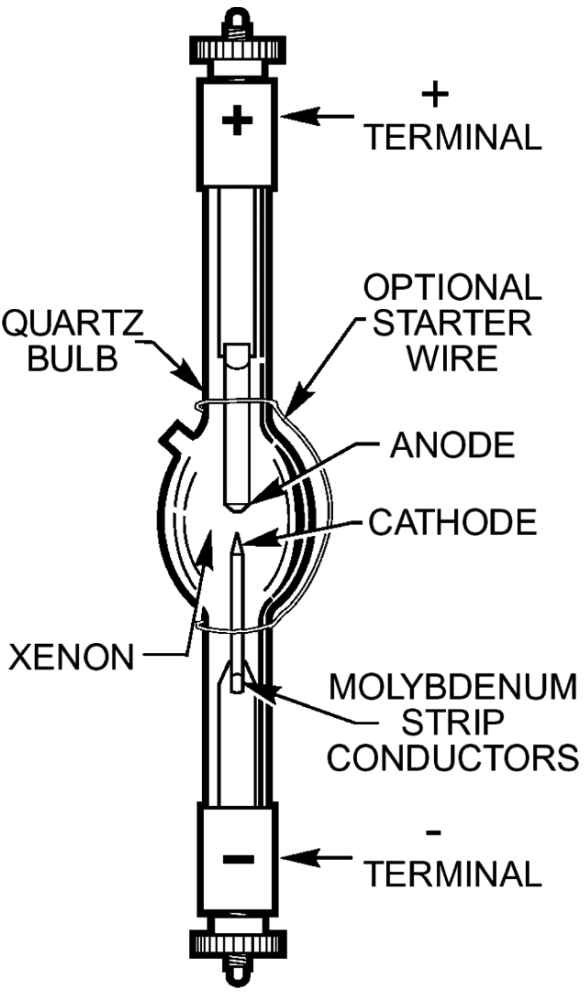

Fig. 7.3. Mechanical outline of a standard high-pressure Xe-arc lamp. The bulb of the lamp is made of quartz, the electrode terminals of metal. A very small arc (around a millimetre long, see text) develops at the centre of the 'bulb' (see Fig. 7.5) (figure courtesy of Hamamatsu Photonics)

larger brightness. They emit an essentially smooth spectrum in the spectral range of interest, with the exception of several weak lines and a group of emission lines between 400 and 450 nm (see Fig. 7.4; Larche, 1953). Xe-arc lamps are available with power ratings from about 75 W to 25 kW and more. As in the case of incandescent lamps, the brightness of the arc is (for a given type of design) largely independent of the absolute power of the lamp.

For special purposes other types of arc lamps are employed. For instance, good UV intensity is obtained from **Deuterium lamps**.

On the other hand, arc lamps, in particular Xe-arc lamps, are relatively difficult to operate. While running at about 18 V DC, they require high voltage (about 25 kV) for ignition, and about 60 V during the initial seconds of warm-up. As in any discharge lamp, there is a need to stabilise the lamp current. The high-voltage burst during ignition, typically provided by a Tesla transformer in the 'lamp igniter' circuit, leads to emission of a strong pulse of electromagnetic radiation, which can be dangerous for other electronic parts of the DOAS systems, such as nearby personal computers. In addition, the high internal pressure (30 atm and more in the cold lamp and two to three

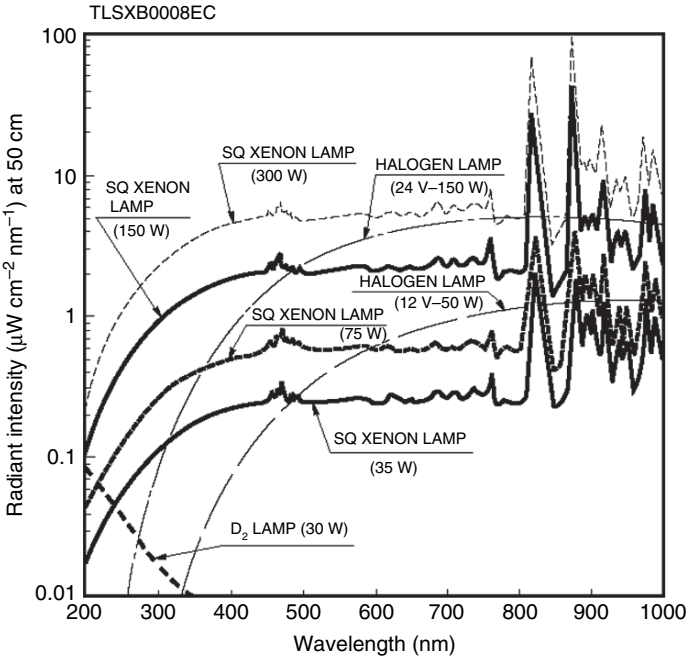

Fig. 7.4. Spectral intensity distribution (brightness) of high pressure Xe-arc lamps (Hamamatsu) in comparison to Deuterium and incandescent lamps. Note that the radiant intensity at 0.5 m distance is plotted. The luminous intensity of high-pressure short-arc Xe lamps is far superior to incandescent lamps throughout the visible and near IR spectrum (figure courtesy of Hamamatsu Photonics)

times as much during operation) of the lamps poses an explosion hazard. Therefore, precautions must be taken during operation, as well as when changing a burned out bulb. Typically, Xe-arc lamps are mounted on a lamp housing that provides electromagnetic shielding against the electromagnetic pulse generated during lamp ignition, as well as protection of the operators against UV radiation and consequences of possible lamp explosions.

Warning: Most arc lamps (including some atomic line calibration lamps) are powerful sources of UV light, with wavelengths in the UVA to UVC range. This radiation represents a severe hazard to eyes and can cause sunburn and ultimately skin cancer. Thus appropriate protection (goggles, radiation tight clothing, sun lotion) must always be used when operating these light sources.

Xe arc lamps are operated at very high internal pressure, thus there is a severe hazard of explosion (of the operating and non-operating lamps. Appropriate protection (safety goggles, protective clothing, etc.) must always be used when handling these light sources.

Xe-arc lamps come in several varieties (see, for example, Table 7.2):

- Standard lamps (e.g. Osram XBO 450 or Hamamatsu SQ – lamps, see Fig. 7.3) emit a Planck spectrum corresponding to a black body of about 6000–8000 K superimposed with some emission lines (see Fig. 7.4), which, due to their width (on the order of 1 nm), can interfere with the DOAS data evaluation. Typical bulb shapes are cylindrical with electrode connections at both ends. Electrode gaps are on the order of millimetres (for instance 4.5 mm in the case of a 450-W lamp). Cross-sections of the intensity distribution across the arc are given in Figs. 7.5 and 7.6. Normally, the lamps can only operate in vertical orientation with the anode at the top. Typical lifetimes are on the order of 1000–2000 h.
- High-intensity lamps (e.g. Osram XBO 500, Narva XBO 301) typically have a much smaller electrode gap than standard Xe-arc lamps, for

Table 7.2. Characteristics of several high pressure Xenon short-arc lamps (from Hermes, 1999)

Lamp manufacturer and type	Size of Arc (50% point) horiz. × vertical µm	Figure	Size of arc (data sheet) horiz. × vertical mm	Intensity in 200 µm circle around brightest spot
Osram XBO 450	770 × 530	7.6	0.9 × 2.7	5.910
Hanovia 959C 1980	380 × 220	7.7	0.3 × 0.3	87.500
Narva XBO 301	300 × 180	7.8	0.2 × 0.3	131.450

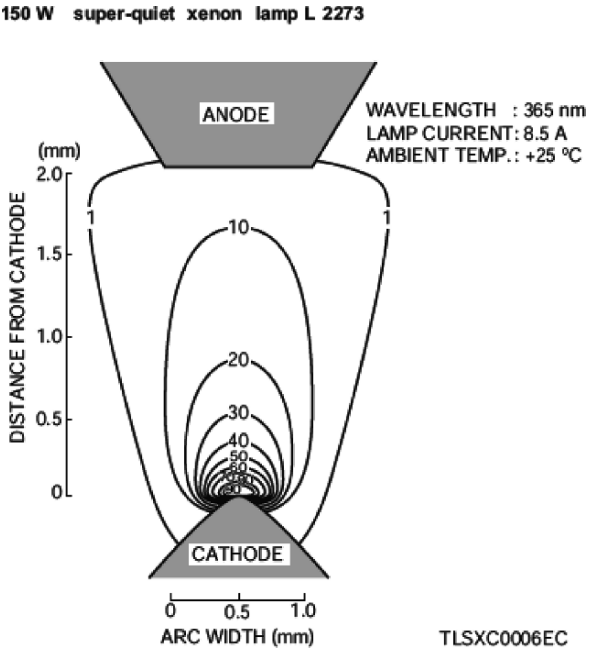

Fig. 7.5. Spatial intensity distribution of a high-pressure Xe-arc lamp. Lines indicate locations of equal luminance (in $10^3\,\mathrm{cd\,cm^{-2}}$) (figure courtesy of Hamamatsu Photonics)

instance <1 mm for a 500-W lamp. They also emit a Planck spectrum corresponding to a black body of about 8,000–10,000 K. More importantly, compared to standard lamps, the radiation is coming from a much smaller area. This can be seen from cross-sections of the intensity distribution across the arc in Figs. 7.7 and 7.8. In addition, the intensity of the emission lines superimposed on the continuum is typically much smaller, and their width is larger; thus, their interference with the DOAS data evaluation is greatly reduced. On the other hand, the lifetime of high intensity lamps is generally much shorter (on the order of 200 h) compared to standard lamps.

- In ozone-free lamps the bulb of the lamp is made of a specially doped type of quartz that blocks radiation below 242 nm (the threshold wavelength for O_2 photolysis). Depending on the type of lamp radiation, output may be degraded at wavelengths as long as 300 nm. Ozone-free lamps are usually more readily available (since they are now the standard in movie projectors). Absence of ozone pollution is also an advantage in the operation of DOAS instruments. On the other hand, care must be taken that the lamp output at short wavelengths is not compromised.

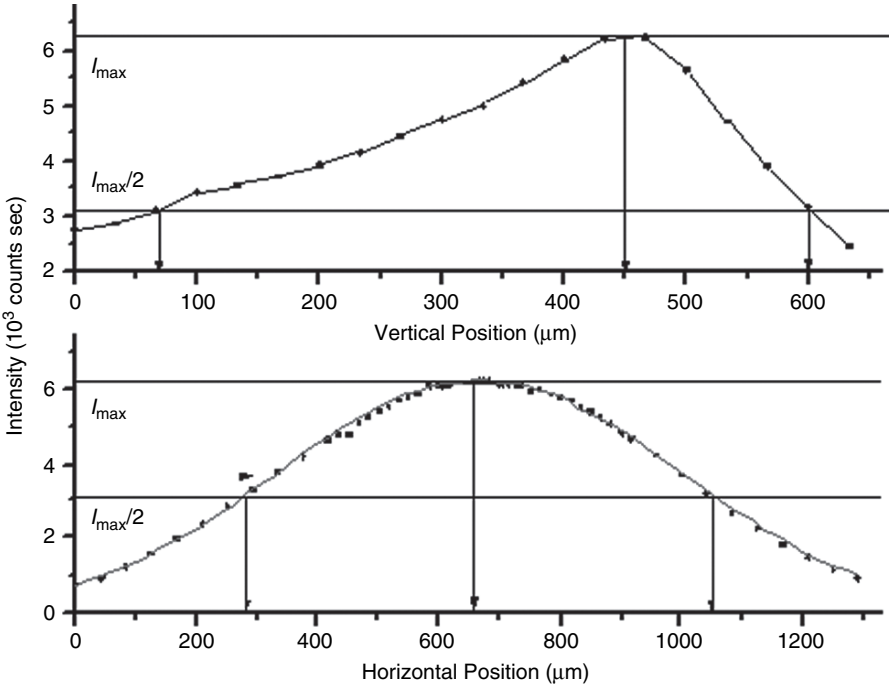

Fig. 7.6. Cross-sections (vertical: in the direction of the current, horizontal: perpendicular to current flow at the plane of highest brightness) of the intensity distribution of a standard 450 W high-pressure Xe-arc lamp (Osram XBO 450; from Hermes, 1999)

- Ozone-producing lamps are sometimes offered with different qualities (with respect to radiation absorbing impurities) of quartz (e.g. Suprasil and Infrasil).

Arc Lamp Stability: Short-term stability is measured over seconds, while long-term stability is measured over minutes, hours, or even days. Short-term stability is affected by arc 'wander', 'flare', and 'flutter'. Arc wander is the movement of the attachment point of the arc on the cathode surface. Typically, the arc circles around the conical cathode tip (see Fig. 7.5) and takes several seconds to complete a full circle. If arc flares occur, there are momentary changes in brightness as the arc moves to an area on the cathode with a better emissive quality than the previous attachment point. Arc flutter is the rapid side-to-side displacement of the arc column as it is buffeted by convection currents in the xenon gas, which are caused by the gas being heated by the arc and cooled by the envelope walls (Fischer, 1987). Arc wander and flare can sometimes be reduced by a slight decrease in the operating current.

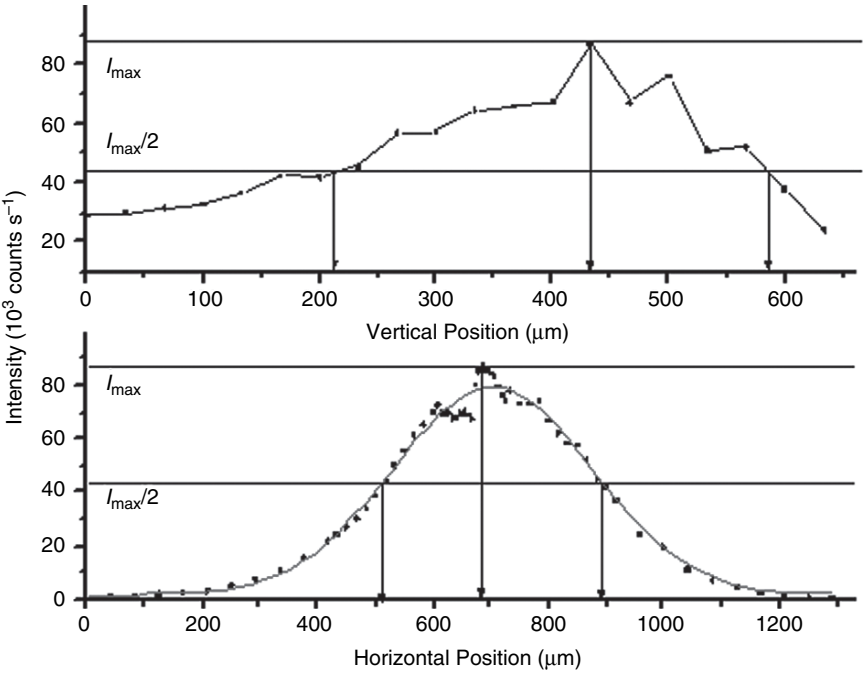

Fig. 7.7. Cross-sections (vertical: in the direction of the current, horizontal: perpendicular to current flow at the plane of highest brightness) of the intensity distribution of a 'high brightness' 500-W high-pressure Xe-arc lamp (Hanovia 959C 1980; from Hermes, 1999)

Xe-arc Lamp Lifetime: Lamp life varies dependent on the type. Specified lifetimes usually range from 200 to 2000 h. The useful life of compact arc lamps is determined by several factors: (1) The decrease of luminous flux due to deposit of evaporated electrode material at the inner wall of the envelope (bulb). The lamp bulb visibly 'blackens', (2) The increase of arc instability, and/or (3) Failure of the lamp to ignite or burn within specified parameters.

Frequent ignition accelerates electrode wear and blackening of the envelope. Usually, the average quoted lamp life is based on approximately 20 min of operation for each ignition. The end of the lamp life is the point at which the UV output has decreased by approximately 25%, the arc instability has increased beyond 10%, or the lamp has ceased to operate. Lamps should be replaced when the average lamp life has been exceeded by 25%.

As the lamp ages, the operating voltage will increase. Lamp current should be decreased to maintain output until the minimum operating current is reached. At this time the lamp should be replaced.

LEDs are potentially useful light sources since they generally emit a smooth spectrum with an emission bandwidth of 10–60 nm. There is a steady improvement of LED brightness and an extension of the spectral range (of

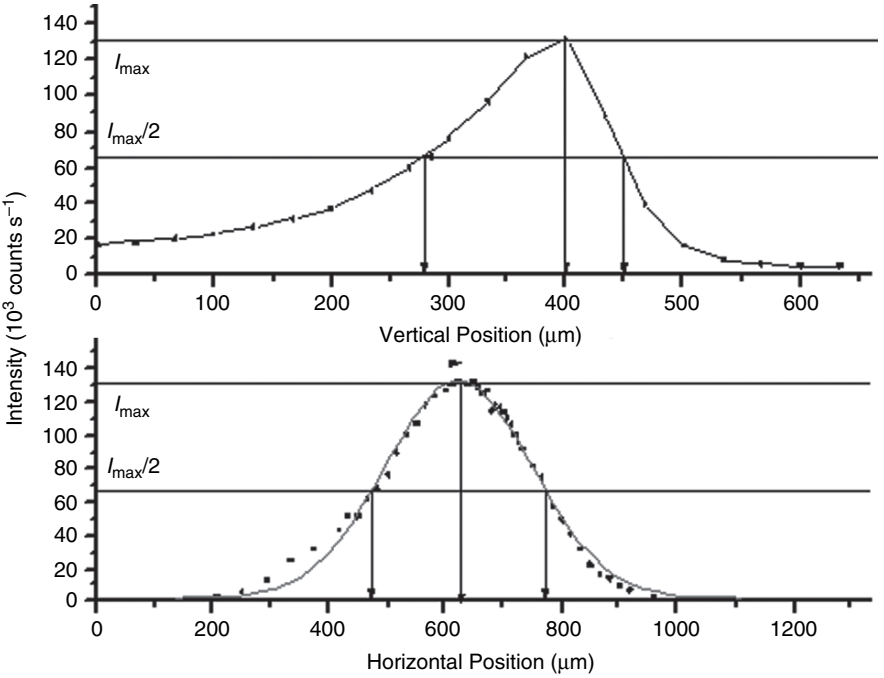

Fig. 7.8. Cross-sections (vertical: in the direction of the current, horizontal: perpendicular to current flow at the plane of highest brightness) of the intensity distribution of a 'high brightness' 300-W high-pressure Xe-arc lamp (Narva XBO 301; from Hermes, 1999)

room-temperature devices) from the original near-IR towards shorter wavelengths (e.g. recently marked by the introduction of GaN devices) (Hermes, 1999; Kern, 2004; Kern et al., 2006).

Presently, LED's are commercially available from the near-UV (about 350 nm) throughout the visible spectral range (starting with blue at about 450 nm) and into the near-IR. Spectral intensity distributions are given in Fig. 7.9. While the emitted total power is orders of magnitude smaller than that of thermal light sources and most laser types, it has to be kept in mind that emission only occurs in a relatively narrow spectral band and, more importantly, from a very small area on the order of 100 μm diameter (Kern, 2004; Kern et al., 2006). In fact, the energy emitted per unit area from many modern LEDs can be comparable to at least that of incandescent lamps. Compared to the electrical input power, LEDs probably give the best spectral intensity (Fig. 7.2) of any light source, with the exception of lasers.

Lasers (broadband) give a far lower beam divergence and higher spectral intensity than thermal light sources, but are usually much more complex devices (although this may change with the availability of room-temperature diode lasers for the visible and UV spectral regions). However, the spectral

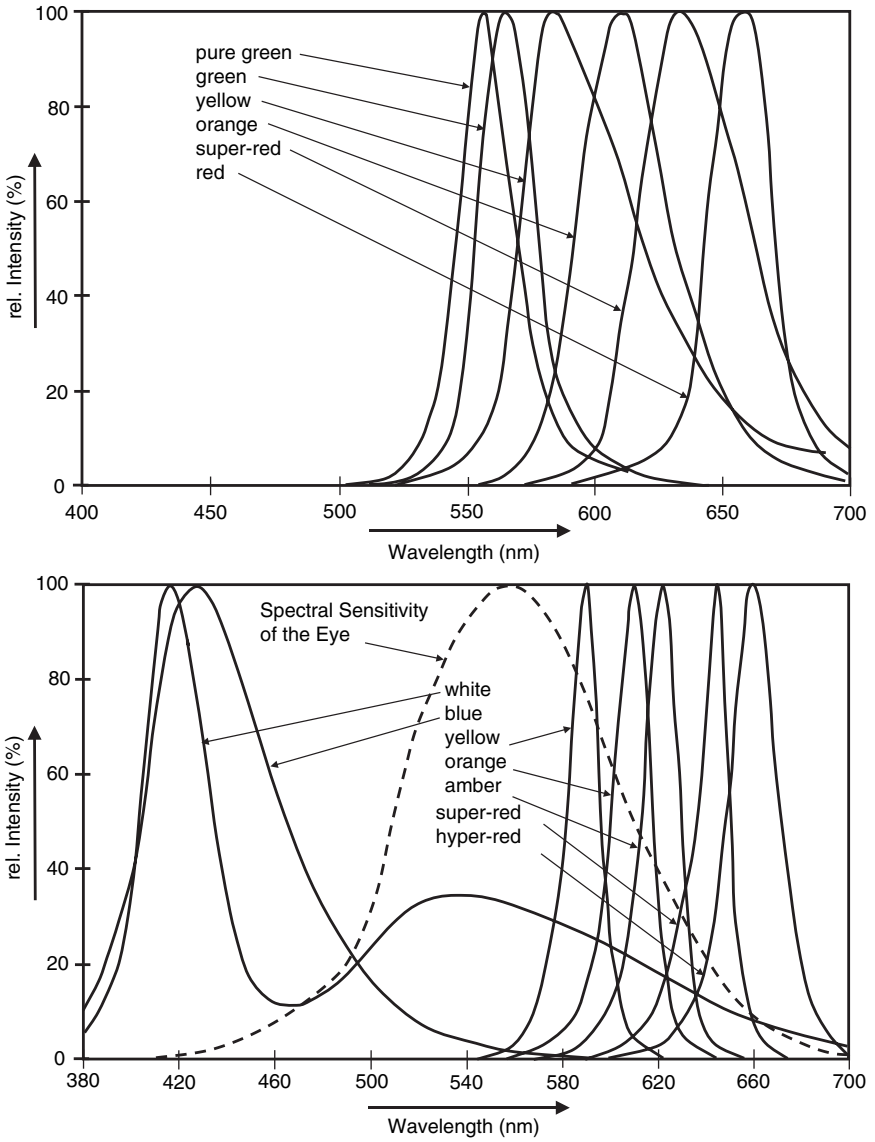

Fig. 7.9. Spectral intensity distribution of a series of LEDs. **Upper panel**: Standard LEDs. **Lower panel**: High brightness GaN LEDs. The dashed line indicates the eye sensitivity

emission bandwidths and tuning ranges of lasers are usually quite narrow. Since the standard DOAS operation requires 'white light' sources, it is usually difficult to observe molecular absorption bands with laser light sources. Therefore, lasers have rarely been used as DOAS light sources. A notable exception is the measurement of OH radicals (together with SO_2, CH_2O, and naphthalene, see Chap. 6), where several rotational lines (of 1–2-pm spectral width) are observed in a spectral interval of about 0.2–0.3 nm, which can be covered by a 'broadband' laser. Presently, developments are under way to improve the spectral emission ranges of dye lasers (Dorn et al., 1996; South et al., 1998) for this, or similar, applications.

7.3.2 Natural Light Sources

Natural light sources include light sources outside the atmosphere i.e. sun, or moon, or even starlight. These light sources provide a light path through the entire atmosphere. The instrument becomes simpler, since no provisions for operating a light source have to be made (see Chap. 11).

The largest problem with natural light sources is the fact that their structured spectrum contains many Fraunhofer lines (see Chap. 9). In addition, the brightness of natural light sources is less than that of good artificial light sources. Other limitations come from the fact that sun, moon, or starlight can only be used under certain circumstances (day, full moon, no cloud cover, etc.) and during certain periods of time (see Sect. 7.3.1).

Direct sunlight allows the determination of the total column density of atmospheric trace gases. The average trace gas concentration measured along the line of sight from the instrument to the sun can be converted to the vertical column density (see Chap.9). Due to the high brightness of the solar disk, the solar intensity is very high. Sun-following optics with moving parts are required to direct the sunlight into the instrument. However, measurements are only possible if the direct sunlight is not blocked by clouds.

A complication with sunlight in comparison with most artificial light sources is the presence of strong absorption features due to the solar atmosphere, the so-called Fraunhofer lines (see Fig. 7.10). Fraunhofer lines are quite strongly structured, and the spectral width of the structures is narrower than the resolution of low-resolution DOAS instruments. The structures are more prominent in the UV, and have large optical densities.

Further complications arise from the fact that the optical densities of the Fraunhofer lines are not constant across the solar disk. This effect is known as 'centre-limb darkening' (Bösch, 2002; Bösch et al., 2003). Therefore, care has to be taken to always observe the full solar disk This can constitute a problem in occultation studies where radiation originating from the (lower) rim of the solar disk is passing through denser parts of the atmosphere, and thus will be more strongly attenuated (Bösch, 2002; Bösch et al., 2003).

Since the contribution of scattered light in direct sunlight is very small, there is no noticeable 'ring effect' (see Chap. 9) in the spectra.

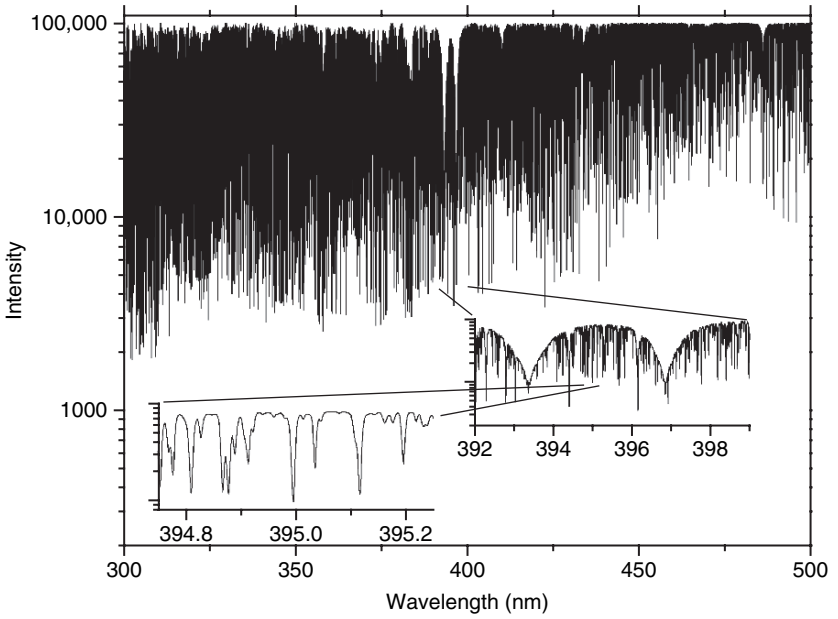

Fig. 7.10. Section of a high-resolution solar spectrum between 300 and 500 nm (from Kurucz et al., 1984)

Direct moonlight observations are subject to essentially the same advantages and restrictions as direct sunlight. However, compared to direct sunlight, the intensity of moonlight is by about five orders of magnitude lower. Of course moon-following optics are required. In addition, moonlight can only be used around the time of full moon. If the moon is not full, brightness (in addition to the smaller visible area) rapidly diminishes because of the large illumination and observation angles under which the lunar surface is seen. On the other hand, moonlight measurements offer the advantage of night-time measurements that allow the study of the abundance of photo-labile species, which cannot be observed with direct or scattered sunlight. Since moonlight is scattered sunlight, the spectral features with respect to Fraunhofer lines are the same as in direct sunlight. Since the moon reflects light from all parts of the solar disk, the centre-limb darkening effect (Bösch et al., 2003) should be absent.

Sunlight scattered in the atmosphere is weaker in intensity than direct sunlight by about four orders of magnitude. Nevertheless, DOAS measurements using scattered sunlight have several advantages. No sun-following optics and hence no moving parts are required, which makes unattended operation very simple. In addition, measurements are also possible in the presence of clouds. Disadvantages include much more complicated calculation of vertical trace gas column densities from the primary 'slant-' (or in this case

rather 'apparent') column densities, particularly if Mie scattering (due to haze or clouds) is involved. These conversions typically involve detailed radiation transport calculations. In addition, the observed spectra are distorted due to (rotational) Raman scattering, leading to a 'filling in' effect of solar Fraunhofer lines at large SZA, the 'ring effect' (Grainger and Ring, 1962), see Sect. (9.6).

Since the atmosphere scatters light very uniformly from all parts of the solar disk in the same way, the centre-limb darkening effect should not be large.

In principle, scattered light from each part of the sky can be used. However, certain arrangements have proven to be particularly popular (see Sects. 7.10.2 and 7.10.3), i.e. ZSL-DOAS and off-axis DOAS. The term 'off axis' refers to a viewing direction 'off' the zenith direction (e.g. Smith and Solomon, 1990; Sanders et al., 1993). The term MAX-DOAS was also recently introduced (e.g. Hönninger and Platt, 2002; Wittrock et al., 2004; Hönninger et al., 2004a). More details are given in Chaps. 9 and 11.

7.3.3 Calibration Light Sources

Wavelength calibration of DOAS spectrometers and determination of their instrument function (see Sect. 7.5) are usually done by recording light with known, usually narrowband, spectral features. This can either be accomplished by subjecting white light to structured and spectrally stable absorption by (sufficiently inert) trace gases in absorption cells (cuvettes), or by suitable glasses, e.g. holmium glass. Alternatively, light sources emitting spectrally structured radiation, such as lasers, atomic emission lamps, or the Fraunhofer structure of sunlight, can be used.

Lasers, in particular gas lasers and some solid-state lasers, can have well-defined emission wavelengths; thus, they are ideally suited for precise wavelength calibration. In addition, the narrow spectral bandwidth ($<10^{-3}$ nm in the visible), is a good approximation of a single wavelength, the response to which directly gives the instrument function of the spectrometer–detector combination. On the other hand, many types of lasers are still expensive and bulky. Some small and inexpensive laser types, such as semiconductor lasers, show a large variation of the emitted wavelength with temperature; thus, they can only be used for determining the instrument function, not the wavelength calibration. For the latter purpose, He–Ne lasers or some solid-state lasers (Nd:Yag) are useful, since their wavelength is determined by atomic transitions.

Atomic emission lamps are a very inexpensive tool for both wavelength calibration and instrument function determination of DOAS spectrometers. They consist of a small glass or quartz envelope filled with a small amount of the particular element. Two electrodes allow flow of current in a low-pressure discharge. In the case of noble gases (He, Ne, Ar, Kr and Xe), a few millibars of the gas are the only component. For lamps showing metal lines (e.g. Hg,

Na, and Cd), Ne is also usually added in order to sustain an initial discharge current to heat the lamp until the metal exhibits sufficient vapour pressure to show emission lines. Depending on the active filling, the lamps emit many discrete emission lines of well-known (usually to a few pm or better) spectral positions (see Table 7.3). Line widths are typically on the order of 1 pm, but depend somewhat on operating conditions (they tend to be wider if the lamp is operated at higher temperature). Some care has to be taken to avoid using lines that are actually multiplets, and which might not be resolved at the spectral resolution of typical DOAS instruments (typically 0.1 nm). It should also be noted that the relative intensities of the various lines can vary considerably from lamp to lamp and also with the operating conditions of a particular lamp. Atomic emission lamps are available in many different configurations and fillings from industry. A simple variety of Ne-discharge lamps is used to illuminate operating indicators in electric devices. Most widely used are mercury, neon, and cadmium lamps. Spectral positions of selected lines of cadmium, mercury, hydrogen, neon, and zinc are given in Appendix A. Some mercury

Table 7.3. Recommended wavelengths (air) and wave numbers (vacuum) for selected Hg spectral lines emitted by pencil-type lamps (adapted from Sansonetti et al., 1996)

Line intensity[a]	Wavelength[b] (nm) in air	Wave number (cm^{-1}) in vacuum
3000000	253.6521	39412.236
160	289.3601	34548.888
2600	296.7283	33691.025
280	302.1504	33086.464
2800	312.5674	31983.828
1900	313.1555	31923.765
2800	313.1844	31920.819
160	334.1484	29918.220
5300	365.0158	27388.271
970	365.4842	27353.171
110	366.2887	27293.096
650	366.3284	27290.138
4400	404.6565	24705.339
270	407.7837	24515.883
34	434.7506[b]	22995.229
10000	435.8335	22938.095
10000	546.0750	18307.415
1100	576.9610	17327.389
1200	579.0670	17264.372

[a]Intensities are relative values based on irradiance values from Reader et al. (1996) with the intensity of 436 nm set arbitrarily to 10,000

[b]The wavelength uncertainty is 0.0001 nm, with the exception of that of the 434.7506-nm line

line positions, together with approximate intensities (Sansonetti et al., 1996), are summarised in Table 7.3. More line positions may be found in the literature, e.g. in the CD-ROM and internet database by Kurucz and Bell (1995).

7.4 Optical Elements for DOAS Systems

Besides a light source, telescope, spectrometer, and detector, a DOAS system also requires further optical components to efficiently transfer the radiation energy from one component to the next. Most of the above listed building blocks consist of elementary optical elements such as plane or curved mirrors, lenses, prisms. In this section, we give a brief overview of these elements, their principles of operation, and some properties. A full treatment of the subject is clearly beyond the scope of this book, and the reader is referred to textbooks of optics such as Smith and King (2000), Hecht (2002), and Bergman (1966).

7.4.1 Some Principles of Optics

Electromagnetic radiation, propagating as electromagnetic waves, may conveniently be represented as rays, which are geometric lines giving the direction along which the electromagnetic energy flows. Optical elements change the direction of these rays. Alternatively, electromagnetic waves may be characterised by their wave fronts, which are perpendicular to the direction of the rays. The action of optical elements may be regarded as changing the shape of the wave fronts. Visualisation, design, and calculation of optical systems (i.e. systems consisting of optical elements) are conveniently done by 'ray tracing'.

In the approximation of optical elements being large compared to the wavelength of the radiation, we can use a 'geometrical optics' approach. Radiation propagates along *straight lines* until *reflected* by mirrors or *refracted* by dense, but transparent material. Accordingly, important optical elements are plane and curved surface mirrors, prisms, and lenses.

Radiation incident on a surface is either absorbed, reflected, or transmitted. Neglecting absorption and transmission, the reflection from a flat surface is said to be either specular from a very smooth mirror-like surface, or diffuse from a matte-finish surface. Of course the terms specular or diffuse denote extreme cases, which can only be approximated in real reflectors, as shown in Fig. 7.11.

In the case of specular reflection (Fig. 7.11, left diagram), the light is reflected at the surface like an elastic sphere bouncing back from a hard surface. Incoming and reflected rays are in a plane with angle of incidence α between the normal of the surface and the incident ray. α is equal to the exit angle α' between the normal of the surface and the exiting ray.

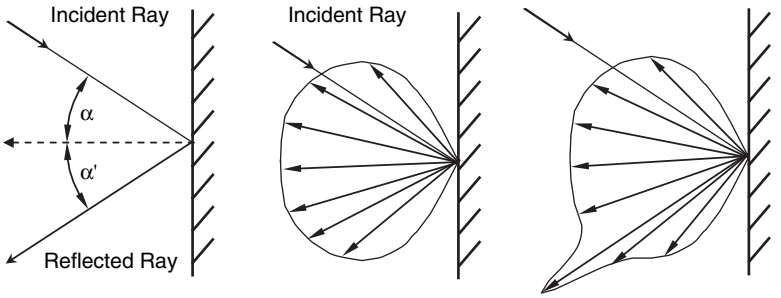

Fig. 7.11. Purely specular (**left**) and purely diffuse (**centre**) reflection from a flat surface are idealised cases. In reality, these cases can only be approximated and usually a combination is observed (**right**)

Radiation incident on transparent surfaces is only partially reflected. Another part of the radiation intensity enters the medium and its direction of propagation is refracted. The direction of the refracted beam (see Fig. 7.12) is given by Snell's law (Snellius law):

$$\frac{\sin\alpha}{\sin\beta} = \frac{n_2}{n_1} \quad \text{or} \quad \sin\alpha = \sin\beta \cdot \frac{n_2}{n_1}. \tag{7.7}$$

The degree of refraction is determined by the indices of refraction (refractive indices) n_1 and n_2 of the two materials. A ray approaching the surface from within the material with the higher index of refraction (n_2 in our example) will exit at $\alpha \geq 90°$, and therefore not exit the material at all if:

$$\sin\alpha = \sin\beta \cdot \frac{n_2}{n_1} \geq 1 \quad or \quad \sin\beta \geq \frac{n_1}{n_2}. \tag{7.8}$$

The ray will undergo **total internal reflection**. Total internal reflection is essentially loss free, if the reflecting surface (boundary between materials with

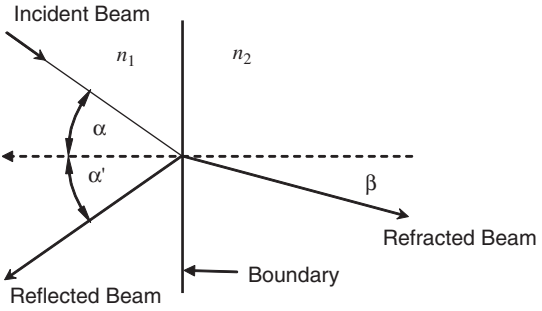

Fig. 7.12. Refraction and (specular) reflection from transparent surfaces. In this example, $n_1 < n_2$; for instance, the ray may enter from air (**left**) through the boundary between the media into glass (**right**)

different index of refraction) is clean. It is used in retro-reflector prisms (see Sect. 7.4.9)

Reflected Intensity: The reflectance $R(\lambda) = I_{reflected}/I_{incident}$ is different for the two polarisation directions; parallel to the plane of incidence and perpendicular to the plane of incidence. It is given by the Fresnel equations:

$$R(\alpha,\beta,\lambda)_{perpendicular} = \left(\frac{n_1\cos\alpha - n_2\cos\beta}{n_1\cos\alpha + n_2\cos\beta}\right)^2 = \left(\frac{\sin(\alpha-\beta)}{\sin(\alpha+\beta)}\right)^2 \quad (7.9a)$$

$$R(\alpha,\beta,\lambda)_{parallel} = \left(\frac{n_2\cos\alpha - n_1\cos\beta}{n_1\cos\beta + n_2\cos\alpha}\right)^2 = \left(\frac{\tan(\alpha-\beta)}{\tan(\alpha+\beta)}\right)^2, \quad (7.9b)$$

where the wavelength dependence is derived from the wavelength dependence of the index of refraction $n(\lambda)$. The last term in (7.9a, b) is derived by introducing Snell's law (7.7) into the preceding term. The total reflectance (for unpolarised light) is given by:

$$R(\alpha,\beta,\lambda) = \frac{1}{2}(R_{parallel} + R_{perpendicular}) = \frac{1}{2}\left(\frac{\sin^2(\alpha-\beta)}{\sin^2(\alpha+\beta)} + \frac{\tan^2(\alpha-\beta)}{\tan^2(\alpha+\beta)}\right), \quad (7.9c)$$

Note that the dependence on the indices of refraction in (7.9a – c) is implicit, since the equations depend on both angles α and β. The dependence on β may be eliminated by introducing $\cos\beta = \sqrt{1-\sin^2\beta} = \sqrt{1-\frac{n_1^2}{n_2^2}\cdot\sin^2\alpha}$ into (7.9a – c).

The transmittance $T(\lambda) = I_{transmitted}/I_{incident} = 1 - R(\lambda)$ is given by:

$$T(\lambda)_{perpendicular} = \left(\frac{2n_1\cos\alpha}{n_1\cos\alpha + n_2\cos\beta}\right)^2 = \left(\frac{2\sin\beta\cdot\cos\alpha}{\sin(\alpha+\beta)}\right)^2, \quad (7.9d)$$

$$T(\lambda)_{parallel} = \left(\frac{2n_1\cos\alpha}{n_1\cos\beta + n_2\cos\alpha}\right)^2 = \left(\frac{2\sin\beta\cdot\cos\alpha}{\sin(\alpha+\beta)\cdot\cos(\alpha-\beta)}\right)^2, \quad (7.9e)$$

At normal incidence, i.e. $\alpha = 0$ (7.9a – c) coincide and simplify to:

$$R(n_1,n_2) = \left(\frac{n_1-n_2}{n_1+n_2}\right)^2, \quad (7.9f)$$

For typical indices of refraction of $n_1 = 1.0$, $n_2 = 1.5$ (e.g. refraction at an air–glass interface), and normal incidence ($\alpha = 0$), a reflectance of $R = 0.04$ is obtained. Fig. 7.13 shows an example of the variation of $R_{parallel}(\alpha)$, $R_{perpendicular}(\alpha)$, and $R(\alpha)$ with α for the above indices of refraction. At small angles of incidence (up to about 20°), the reflectance stays near 4%, sharply increasing to unity as α approaches 90°. Note that $R_{parallel}$ has a minimum with $R_{parallel} = 0$ at some angle of incidence α_B. This angle, where polarised light is not reflected and hence $R_{parallel}(\alpha_B) = 1$, is called the Brewster angle.

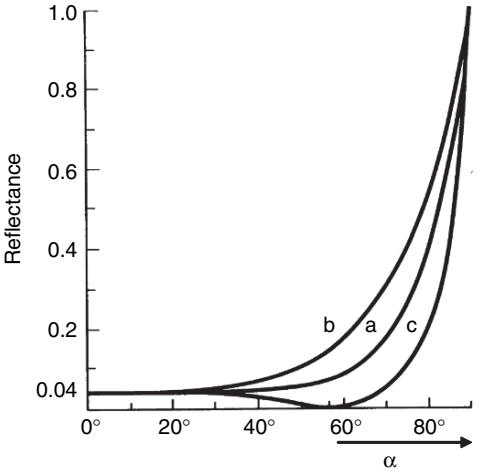

Fig. 7.13. Intensity reflected from a flat, dielectric surface. Curve (**a**) shows total reflectance $R(\alpha)$ for the unpolarised incident light. Curves (**b**) and (**c**) show the reflectances for polarised light with perpendicular and parallel polarisation, respectively. Note the zero reflectance, and thus 100.00% transmission, for parallel-polarised light at the Brewster angle

The index of refraction of (transparent) materials varies as a function of wavelength. Some examples of various glass and quartz types are shown in Fig. 7.14.

The index of refraction of gases is a function of their density, which in turn are functions of temperature T and pressure p.

$$n\,(p,T) = \frac{p}{p_0} \cdot \frac{T_0}{T} \cdot (n_0 - 1) + 1. \tag{7.10}$$

For dry air, $n_0 \approx 1.000293$ denotes the index of refraction at 589 nm, standard pressure and temperature, $p_0 = 1\,\text{atm}$ (101325 Pa) and $T_0 = 273.15\,\text{K}$ (0°C), respectively.

Reflection on Metals: Metals can be treated as materials having a given index of refraction, but also an attenuation coefficient due to the electric conductivity of metals. In the case of a zero attenuation coefficient and a very high index of refraction, Snell's law (7.7) would be applicable and the reflectivity would become very high. The sketch of a typical metal reflectivity as a function of polarisation (parallel or perpendicular to the plane of incidence) in Fig. 7.15 shows that the reflectance of metals indeed behaves qualitatively similarly to the reflectance of dielectric materials.

Fig. 7.16 shows reflectance curves R as a function of wavelength for the popular mirror coatings silver, gold, copper, and aluminium. In the red and infrared spectral regions, gold has superior reflectance (R $\approx$ 0.99, hence its reddish colour). Silver is almost as good a reflector (R $\approx$ 0.98) in the visible

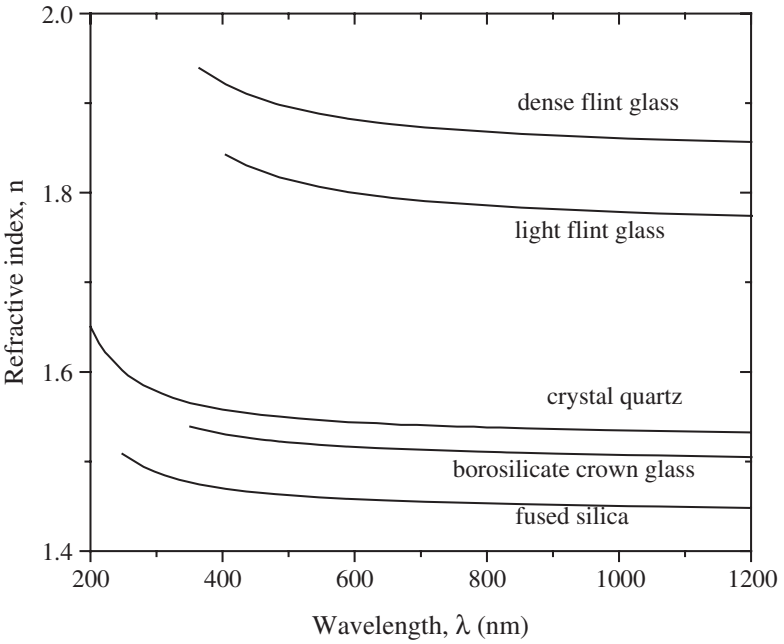

Fig. 7.14. Index of refraction as a function of wavelength for various glasses, quartz, and acrylic plastic (data courtesy of Schott)

and near-IR spectral ranges. Aluminium is much less reflective than the noble metals, but superior in the UV. Note that optical mirrors are usually first surface mirrors, i.e. the reflective coating is on the surface oriented towards the incident radiation. Therefore, the metal surfaces, e.g. silver and to an even larger extend aluminium mirrors, are susceptible to corrosion and normally require protective layers, usually a thin overcoat of SiO or MgO.

7.4.2 Mirrors

The reflection by plane mirror surfaces is shown in Fig. 7.11, with the angle of incidence equal to the angle of reflection. Curved mirror surfaces, however, can have imaging properties. Here, we discuss the imaging properties of a spherical, concave mirror shown in Fig. 7.17. A sufficiently small surface element of any curved mirror can be considered plane.

A ray entering parallel to the mirror axis (solid line in Fig. 7.17) at distance d will hit a mirror with a curvature of radius r, at point A. It is incident at an angle α with the normal to the mirror surface at A (dashed line AM in Fig. 7.17). The ray is reflected at an angle of α and intersects the mirror axis at point F. The reflected ray forms an angle of $\alpha' = \alpha$ with the normal intersecting the mirror axis at point M. Thus, AMF is an isosceles triangle with $a = f$ and:

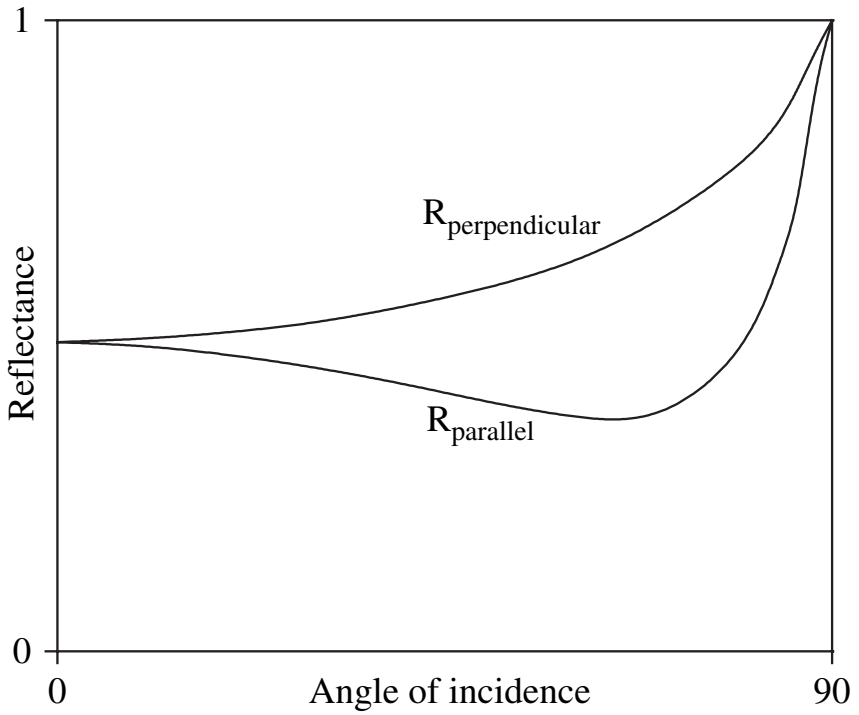

Fig. 7.15. Typical reflectance ($R_{perpendicular} = R_{\perp}$) for linearly polarised beams of radiation incident on a metal as a function of angle of incidence. $R_{parallel}$ drops to a minimum at the so-called 'principal angle of incidence', marked by a dot

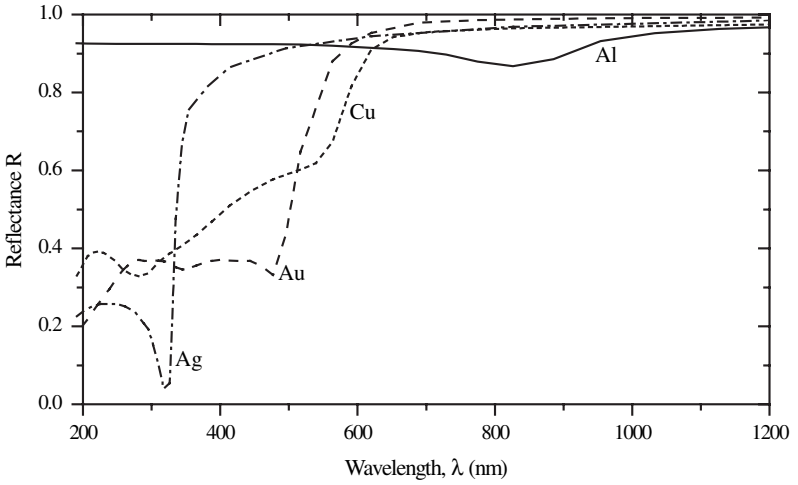

Fig. 7.16. Reflectances of silver, gold, copper, and aluminium as a function of wavelength (CRC, 2008)

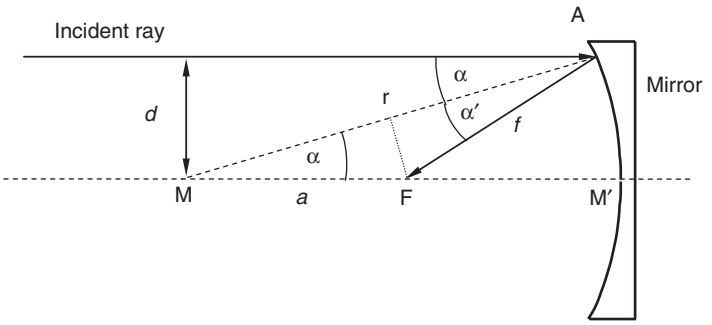

Fig. 7.17. Imaging by a (concave) spherical mirror, with radius of curvature r. Line AM denotes the normal to spherical surface at point A. The angle of incidence is α. In the paraxial approximation ($\cos\,\alpha \approx 1$), all rays incident parallel to the optical axis (MM′) of the mirror (at distance d) will be reflected such that they cross the focal point F at the focal length (AF = FM′ = f) of $f = r/2$

$$\cos\alpha = \frac{r/2}{a} \quad a = f = \frac{r}{2\cos\alpha} \quad \text{and also } \sin\,\alpha = \frac{d}{r}. \tag{7.11}$$

For rays entering very close to the optical axis ('paraxial' rays), α will become very small, and thus $\cos\,\alpha \approx 1$. In this 'paraxial approximation', a spherical mirror has the focal length $f = r/2$.

As a more general case, we consider a concave mirror, as shown in Fig. 7.18. All rays incident at an arbitrary distance d from the optical axis must travel the same distance from points B on plane BB′ via A to F. Thus, the distances BA + AF must be equal to BC (where C is on plane CC′) for all values of d. A curve containing all points with the same distance between a line (i.e. CC′)

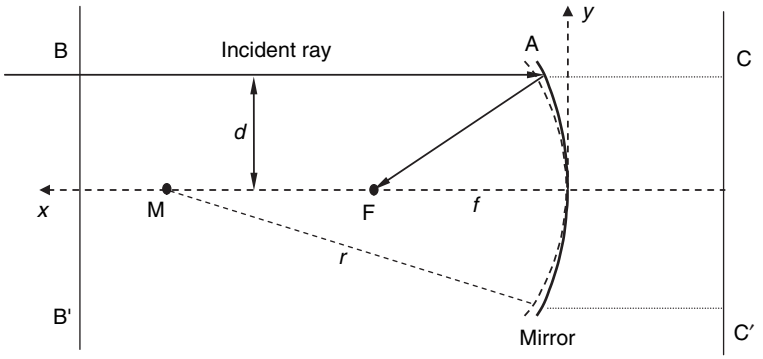

Fig. 7.18. Imaging by a parabolic mirror. For any ray incident parallel to the optical axis the distance BA + AF must be equal to BC i.e. constant. A parabolic mirror can be aproximated by a spherical surface as shown by the dashed line

and a point (F in this case) is a **parabola**. The points of the parabola are related by the formula:

$$x = \frac{1}{4f} \cdot y^2; \quad y = \sqrt{4f\,x} = 2\sqrt{f\,x}. \tag{7.12}$$

A parabola can be approximated by a sphere given by $y^2 + (x - r)^2 = r^2$ (centre of the sphere M is shifted from the origin by r) or $x^2 - 2rx + y^2 = 0$. Solving for x gives:

$$x = r \pm \sqrt{(r^2 - y^2)}. \tag{7.13}$$

Expansion in a binominal series gives:

$$x = \frac{y^2}{2r} + \frac{y^4}{2^2 2! r^3} + \frac{3y^6}{2^3 3! r^5} + \ldots \tag{7.14}$$

The first term of the expansion corresponds to the equation of a parabola (7.12) with $f = r/2$; the remaining terms describe the deviation between a sphere and a parabola:

$$\Delta x = \frac{y^4}{8r^3} + \frac{3y^6}{48r^5} + \ldots \tag{7.15}$$

For small values of y (i.e. paraxial rays), the deviation will be relatively small and spherical, and parabolic curves will be indistinguishable.

A reflecting parabolic (concave) mirror with the focal length f images any object (size: G) further away from the surface than $2f$ in reduced size (B) at a distance between f and $2f$ (see Fig. 7.19). The relationship between focal length f, distance of object and image from the vertex of the parabola g and b, respectively is given by:

$$\frac{1}{f} = \frac{1}{g} + \frac{1}{b}. \tag{7.16}$$

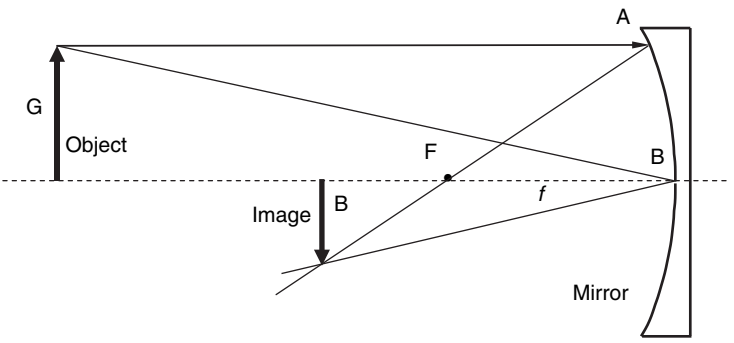

Fig. 7.19. Imaging by a parabolic mirror. An object (G) further away from the surface than $2f$ will be imaged in reduced size (B) at a distance between f and $2f$

7.4.3 Prisms

Prisms change the direction of rays by refraction. There are two refracting surfaces (see Fig. 7.20, apex angle γ). A ray entering at an angle of incidence, i.e. the angle between the direction of the ray and the normal on the surface, β_1 at the left surface is refracted and continues at an angle β_2 inside the prism, until exiting at angle β_3 at the right surface, thereby being refracted again outside of the prism at an angle β_4. The different angles are connected by Snell's law of refraction (7.7):

$$n_1 \sin \beta_1 = n_2 \sin \beta_2 \text{ and } n_2 \sin \beta_3 = n_1 \sin \beta_4,$$

where n_1 and n_2 denote the indices of refraction outside and inside the prism, respectively. The total deviation β between the incoming and outgoing beam is $\beta = \beta_1 - \beta_2 - \beta_3 + \beta_4$. Since in the triangle OAB, $\gamma = \beta_2 + \beta_3$, we obtain $\beta = \beta_1 + \beta_4 - \gamma$.

For small angles γ we have:

$$\beta = (n-1) \cdot \gamma$$

Prisms can be used to separate radiation of different wavelengths in spectrometers. Putting polychromatic light through a prism will result in the rays being refracted in different directions with the total angular deviation:

$$\frac{d\beta}{d\lambda} = \gamma \cdot \frac{dn}{d\lambda}, \tag{7.17}$$

where $dn/d\lambda$ denotes the change of the refractive index with wavelength, the dispersion (see Fig. 7.14), which for most glass types is on the order of $10^{-4}\,\mathrm{nm}^{-1}$.

7.4.4 Lenses

Treating a lens as a series of thin prisms leads to an expression relating the radii of curvature of both lens surfaces to the focal length of the lens, the 'lensmaker's formula':

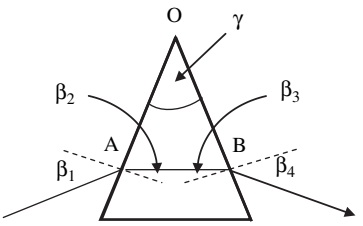

Fig. 7.20. Sketch of ray propagation through a prism

$$\frac{1}{f} = (n-1) \cdot \left(\frac{1}{r_1} - \frac{1}{r_2} \right). \tag{7.18}$$

Note that the difference in the indices of refraction n of the lens material and the material around the lens (here set to unity) enters the equation. For lenses, the Cartesian **sign convention** of r_1 and r_2 is such that the radii of surfaces, for which the centre of curvature is on the opposite side of the light source, are defined as positive. If the centre of curvature is on the same side as the light source, r is defined as negative. For instance, for the lens in Fig 7.21, r_1 would be defined as positive, while r_2 would be negative. Therefore, in the case of a biconvex lens, the focal length would be:

$$\frac{1}{f} = (n-1) \cdot \left(\left| \frac{1}{r_1} \right| + \left| \frac{1}{r_2} \right| \right).$$

Thus, (7.18) also can also be applied to biconcave or concave–convex lenses. An important property of lenses is the relatively strong dependence of the focal length on the index of refraction, with $f \propto 1/(n-1)$, and thus on the wavelength of the radiation, since n varies considerably with the wavelength, in particular in the UV (see Fig. 7.14).

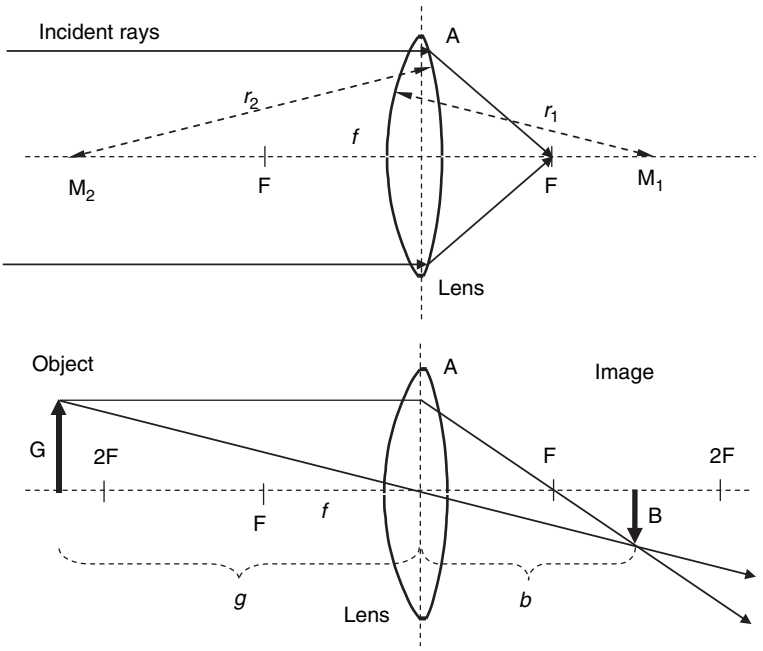

Fig. 7.21. Imaging by a thin biconvex lens. **Upper panel**: relationship between radii of curvature and 'focal length (see 'lensmaker's formula'). **Lower panel**: Imaging of object with extension G into image with extension B. The vertical dashed lines indicate the 'principal plane' of the lens i.e. the position of an idealised, infinitely thin lens

A convex lens can produce an image of an object. The Gaussian lens formula relates the distance g between the object and the lens to the distance b between lens and image:

$$\frac{1}{f} = \frac{1}{g} + \frac{1}{b}, \tag{7.19}$$

where f denotes the focal length of the lens. An example is outlined in Fig. 7.21. Note that the formula is the same as (7.16), but object and image are on opposite sides of the optical element (lens). The size B of the image can be calculated from the relationship:

$$\frac{\mathrm{B}}{\mathrm{G}} = \frac{b}{g} = \mathrm{M}, \tag{7.20}$$

with the magnification M. The angular extents of object and image (i.e. the angle under which the object or image are seen from the position of the lens) are given by:

$$\tan\beta = \frac{\mathrm{B}}{b} \quad \text{and} \quad \tan\gamma = \frac{\mathrm{G}}{g}. \tag{7.21}$$

7.4.5 Apertures, Entendue, Lagrange Invariant

The amount of radiation power gathered by an optical system (e.g. consisting of mirrors or lenses) will be directly proportional to its entrance area. A large 'clear entrance' area will usually gather more light than a smaller one. Of course, this will only be true if all of the entrance area is illuminated by the source. The size (linear extent) of the image produced by an optical system will vary proportional to its focal length f. Since a given amount of light enters through the entrance area, the irradiance in the focal plane of an optical system of given entrance area, will be inversely proportional to the image area, and hence f^2.

Most optical elements are circular in shape, and thus their area is proportional to the square of their diameter $D = 2R$ (R: radius of the optics). The ability to produce a bright image is therefore proportional to $(D/f)^2$. A customary way to specify this ability is thus the relative aperture D/f or its inverse, the focal ratio or **f-number** f/D. Frequently, the f-number is written as $f/\#$. Optical systems with a smaller f-number will therefore produce a brighter image. In fact, comparing a system with a given $(f/\#)$ to one having $(f/\#)/2$ will result in four times the brightness of the image in the system with $(f/\#)/2$. Another way to specify the ability of an optical system is its **numerical aperture** (NA), which is defined as R/f. Both quantities are related by:

$$F = {}^{f}/_{\#} = \frac{1}{2\,(\mathrm{NA})}. \tag{7.22}$$

The **entendue**, which is defined as the product of the entrance area A times the aperture solid angle Ω: $E = A \cdot \Omega$, is a constant of optical systems. In

other words, the entendue of the light entering an optical system is as large as the entendue of the light leaving it. For example, reduction of the size B (and thus the area in proportion to B^2) of an image e.g. by a lens, will increase the aperture solid angle, thus keeping the entendue constant.

Object and image, respectively, see the lens in Fig. 7.21 under the angles α_{G} and α_{B}. Using the lens radius R_{L} we derive:

$$\tan\alpha_{\mathrm{G}} = \frac{R_{\mathrm{L}}}{g} \quad \text{and} \quad \tan\alpha_{\mathrm{B}} = \frac{R_{\mathrm{L}}}{b},$$

Considering $g \cdot \tan\alpha_{\mathrm{G}} = R_{\mathrm{L}} = b \cdot \tan\alpha_{\mathrm{B}}$ and (7.20) we get:

$$G \cdot \tan\alpha_{\mathrm{G}} = B \cdot \tan\alpha_{\mathrm{B}} = \mathrm{L}, \tag{7.23}$$

where L denotes the **Lagrange invariant**. L is another conserved quantity.

7.4.6 Diffraction at Apertures

Radiation passing through apertures of finite size or grazing edges will undergo diffraction, meaning that part of the incident radiation deviates from its original direction.

In the case of a parallel beam passing through a **circular aperture** (i.e. a circular hole in a piece of non-transparent matter oriented perpendicular to the propagation direction of the radiation, or a circular mirror) with radius R, there will be concentric rings of diffracted radiation around the centre beam. The angle ϑ between the diffracted radiation and the original beam direction and its intensity $\mathrm{I}(\vartheta)$ is given by:

$$I(\vartheta) = I_0 \left(\frac{2\mathrm{J}_1(x)}{x} \right)^2 \quad with\ x = \frac{2\pi R}{\lambda} \cdot \sin\vartheta. \tag{7.24}$$

$\mathrm{J}_1(x)$ denotes the Bessel function of first degree, λ the wavelength, and I_0 the original intensity. The diffraction angles and intensities of the first few minima and maxima are given in Table 7.4

Table 7.4. First maxima and minima of radiation diffracted at a circular aperture

Maximum/minimum no.	I/I_0	$\frac{\sin\vartheta}{\lambda/R} = \sin\vartheta \cdot \frac{R}{\lambda}$
Min. 1	0	0.61
Max. 1	0.0175	0.815
Min. 2	0	1.08
Max. 2	0.00415	1.32
Max. 3	0.00160	1.85

For a very long rectangular aperture with width d (i.e. a slit with a length $>> d$), the diffracted intensity is given by:

$$I(\vartheta) = I_0 \frac{\sin^2 x}{x^2} \text{ with } x = \frac{\pi d}{\lambda} \cdot \sin\vartheta. \tag{7.25}$$

Thus, the first minimum is at $x = \pi$ with $\sin\vartheta = \lambda/d$.

7.4.7 Quartz-fibres, Mode Mixers, and Cross-section Shaping

Quartz (or glass) fibres rely on total internal reflection (see Sect. 7.4.1) to conduct radiation. In practice, the total reflection does not occur between the quartz (or glass) and the surrounding air, but rather between the (relatively) high index of refraction (n_f) core of a fibre clad with a outer layer of material with a lower index of refraction (n_c) (see Fig. 7.22).

A maximum angle of incidence $\alpha_\mathrm{i} = \alpha_\mathrm{max}$ exists below which the light entering the fibre is actually transmitted by total internal reflection. The external α_i corresponds to an internal α_t due to refraction at the boundary between the ambient medium (e.g. air, index of refraction $n_0 \simeq 1$) and the core of the fibre (index of refraction n_f). A detailed calculation yields:

$$\sin\alpha_\mathrm{max} = \sqrt{n_f^2 - n_c^2}.$$

The NA and f-number of a glass fibre are given by:

$$\mathrm{NA} = \sqrt{n_f^2 - n_c^2} \qquad f/\# = \frac{1}{2\sqrt{n_f^2 - n_c^2}}. \tag{7.26}$$

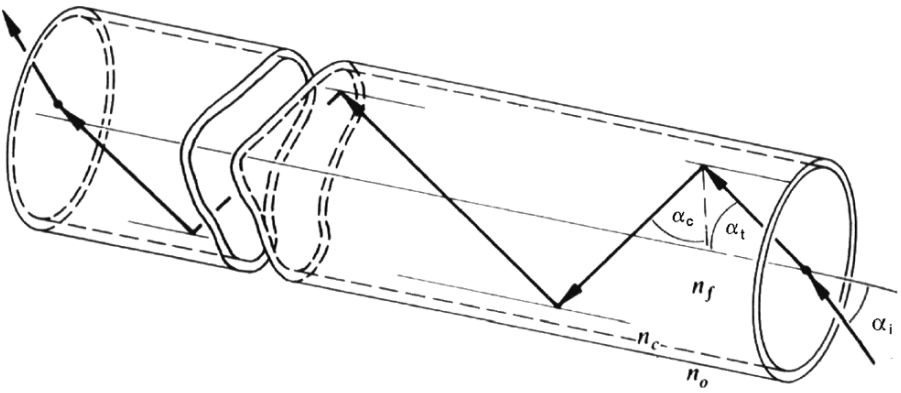

Fig. 7.22. Propagation of radiation in an optical fibre

Fibres are conveniently employed to connect optical elements within DOAS systems, for example the receiving telescope to the spectrometer. This arrangement gives freedom in the placement of the components; for instance, the telescope can be placed outside, while the spectrometer is sheltered. The spectrometer does not need to be physically attached to the telescope (see also Sect. 7.9.3).

Optical fibres can in fact be an important optical component, improving the overall sensitivity of the system considerably. This is due to several properties of optical fibres:

1. Non-uniform illumination of the field of view of the spectrometer can cause residual structures in the spectra, which may limit the minimum detectable optical density to $2 - 10 \times 10^{-3}$ (Stutz and Platt, 1997a). Introducing 'mode mixers' into the quartz fibre connecting the receiving telescope to the spectrometer can greatly reduce this effect. Figure 7.23 shows a sketch of a mode mixer arrangement.
2. Most fibres scramble the polarisation state of the transmitted radiation, thus effectively removing the polarisation sensitivity of DOAS instruments. Polarisation sensitivity can be a problem in DOAS instruments; in particular in passive, scattered light applications, where the incoming radiation is, in general, partially polarised, see Chap. 4.
3. Fibre bundles can be used to change the cross-section of a light bundle. This property can be used to match the approximately circular (see Sect. 7.3.1) shape of e.g. a Xe-arc light source to the rectangular aperture of the spectrometer entrance slit. Figure 7.24 shows an example in which a bundle of 19 fibres is arranged in an approximately circular shape at the entrance and a column at the exit.

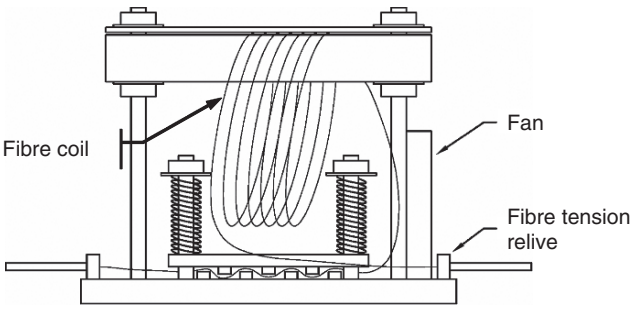

Fig. 7.23. Sketch of a fibre-mode mixer after. The device consists of two elements: (1) A fibre coil (top part of the figure), which is slightly 'shaken' by an air stream generated by the fan and (2) a section of the fibre that is put under mechanical stress by a spring loaded plate introducing several sharp bends in the fibre (bottom part of the figure) (adapted from Stutz and Platt, 1997a)

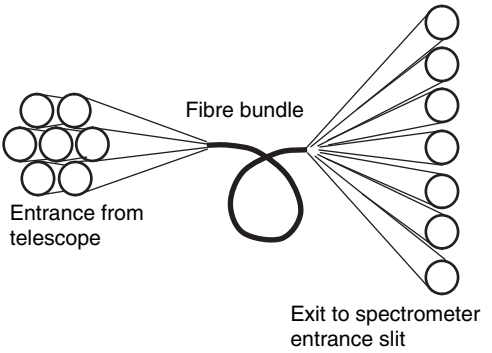

Fig. 7.24. Cross-section change from a circular entry to a column at the exit by an optical fibre bundle

7.4.8 Filters

In DOAS systems spectral filters are usually required for several purposes. These include blocking unwanted spectral orders (see Sect. 7.5.1) or reducing the amount of stray light in the spectrometer (see Sect. 7.5.4) by limiting the spectral bandwidth of the radiation entering the instrument. In addition, it is desireable to eliminate the visible part of the light from the light source in order to avoid blinding humans and make the radiation emitted by the DOAS instrument less visible.

Filters can either be 'colour glass' type (e.g. Schott UG5), thin film partially reflecting filters, or thin-film interference filters. Figure 7.25 shows the transmission curve for a several UG-type colour glass filters used to block visible light and thus reduce spectrometer stray light.

Under certain circumstances the radiation intensity may be too large for a given detector, for example when observing direct sun signals by an instrument optimised for scattered light operation. In these cases, optical attenuation is required. While this can be achieved by several measures, such as defocusing or reducing the aperture, grey filters offer a simple and clean way to reduce the signal level essentially without changing other properties of the optical system. Grey filters are usually characterised by an attenuation factor $A = \mathrm{I}/\mathrm{I}_0$ (I_0 and I denoting incident and transmitted intensities, respectively), frequently expressed as optical density base 10 [$\log^{10}(A)$ or $\lg A$]. The attenuation A should ideally be independent of the wavelength. There are three popular types of optical attenuators, grey glass filters, which rely on the optical absorption by suitable glass types, thin-film partial reflective surfaces, and mesh-type devices. The latter attenuator types are useable from the UV to near-IR, while grey glass filters are usually limited to the visible spectral range. A potential difficulty (in particular for DOAS applications)

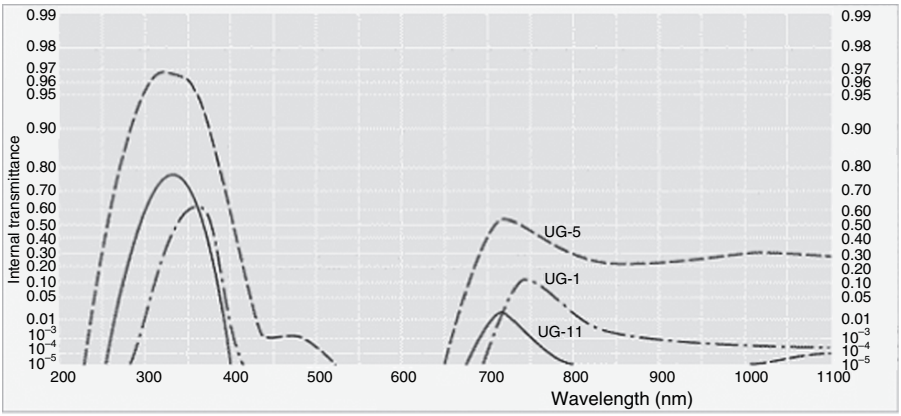

Fig. 7.25. Sample transmission curve of colour glass filters (UG-1, UG-5, UG-11 from Schott, Mainz, 2 mm thickness). These filters are used to reduce spectrometer stray light in DOAS applications. Note that the second transmission maximum in the red/near-IR region is where the sensitivity of silicon detectors usually reaches its maximum (figure courtesy of Schott)

of reflective attenuators is the Fabry–Perot etalon effect, which is caused by interferences in the thin optical reflective layer.

7.4.9 Retro-reflectors

The purpose of retro-reflectors is to return a beam of light back to the sending-receiving telescope of the DOAS instrument. While, in principle, plane mirrors could be used [see e.g. Perner et al. (1976) and Hübler et al. (1984)], there are several types of optical arrangements that return the incident light exactly (although with some lateral offset) into the direction of incidence, see Fig. 7.26 (Eckhardt, 1971; Sugimoto and Minato, 1994). The most popular design is the 'corner-cube' retro-reflector, also called 'trihedral' retro-reflector or triple retro-reflector [see e.g. Eckhardt (1971)]. It consists of three plane, reflecting surfaces arranged at right angles (Fig. 7.26). Thus, the reflecting surfaces can be viewed as being arranged like the three surfaces that meet in the corner of a cube. The radiation would incite from the direction of the cube's main diagonal. In a typical active DOAS instrument, a light beam from a search light-type light source would be directed towards one or several retro-reflectors mounted at a distance equal to half the total desired light path (see Fig. 6.2). The necessary angular precision of the retroreflectors, measured as the angle between incoming and outgoing beams, is on the order of a few seconds of arc (about 10^{-5} radians), which usually requires specially made high-precision devices. An additional property of retro-reflectors is reduction of the effect of atmospheric turbulence on the light beam. As illustrated in

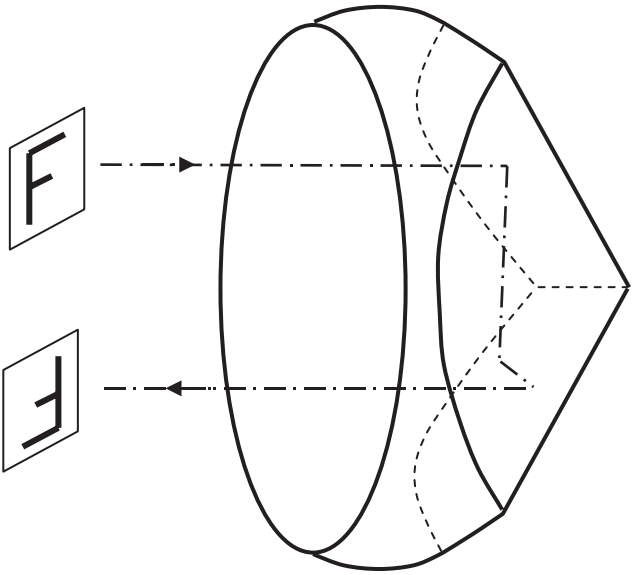

Fig. 7.26. Reflections in a corner cube retro-reflector prism

Fig. 7.27, this is due to the capacity of corner cube retro-reflectors to return the incident light exactly (although with some lateral offset) into the direction of incidence.

There are two varieties of the 'corner cube' retro-reflector design in use: Hollow corner cubes made of three flat (first surface) mirrors mounted at very precise 90° angles. In order to protect the mirror surfaces, which are difficult to recoat without taking the assembly apart, quartz front panes are sometimes added. These front panes represent four additional surfaces to the

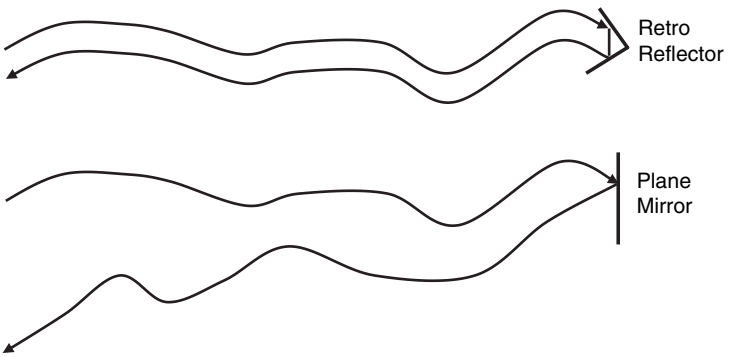

Fig. 7.27. Compensation of turbulent beam dispersion by a (corner cube) retro-reflector arrangement (**upper panel**), in comparison to reflection by a plane mirror (**lower panel**).

light returned by the retro-reflector leading to additional light loss due to Fresnel reflection [see (7.9) and Table 7.5].

In contrast, prism-type retro-reflectors need no additional protection of front surfaces. The reflection at the rear surfaces of prism-type retro-reflector elements can either be due to total internal reflection or by a coating applied to the outside of the flat corner cube surfaces of the prism. Both approaches have advantages and drawbacks. In the case of internal reflection, the efficiency of returning light is the highest of all types described here, the only loss being the reflection off the (usually circular) surface of the prism. On the other hand, the useable range of acceptance angles is smallest because the limiting angle of total reflection is exceeded at higher incidence angles (Rityn, 1967). In contrast, the coated corner cube prism has relatively large reflectance losses, in particular in the UV wavelength range. Typical reflectivities are on the order of $R \approx 0.8$–0.9 (see Fig. 7.16); for three reflections, this amounts to an overall efficiency of 40–50% including the 4% losses ($R_S \approx 0.96$) occurring twice at the surface of the prism, see Table 7.5. On the positive side, the coated corner cube prism features the largest acceptance angle range (much larger than in the internal reflectance case, but also larger than the hollow cube corner), since all incident rays are diffracted towards the symmetry axis, i.e. become lower inside the prism (Rityn, 1967).

In order to save weight, an array of small retro-reflector elements is typically used, rather than a single large unit. Typically, reflector prism sizes

Table 7.5. Characteristics of different corner cube retro-reflector designs

Type of retro-reflector	Reflectance	Acceptance angle range Degrees	Comment
Hollow cube corner	R^3 typ. 50 %	≈ 32–56	Least expensive type for a given aperture. Vulnerable to dirt
Hollow cube corner with protective pane	${R_S}^4 \cdot R^3$ typ. 40 %	≈ 32–56	Protected, but more expensive, while being less efficient
Corner cube prism, coated	$R_S^2 \cdot R^3$ typ. 45 %	60–90	Type of choice for wide angle applications
Corner cube prism, total internal reflection	R_S^2 typ. 92 %	20–60	Good compromise between protection and economy, most widely used type

R = reflectance of one of the corner cube surfaces, R_S = reflectance of a surface perpendicular to the light beam, e.g. of a protective (quartz) cover pane

are on the order of 60 mm diameter. Special design variants have also been explored (Minato et al., 1992; Minato and Sugimoto, 1998).

There are several limitations to watch, however: For most applications the reflectors must be of very high precision. For instance, if a deviation of the returning beam of a typical retro-reflector diameter (60 mm, see above) over a distance of 5 km is desired, this corresponds to an angle between incoming and outgoing light beams of about $\delta = 0.06\,\mathrm{m}/5000\,\mathrm{m} \approx 1.2 \times 10^{-5}$ radian ($\approx 7 \times 10^{-4}$ degrees or about 2 s of arc).

Another limitation is due to diffraction at the retro-reflector aperture. The angle of diffraction for the first maximum of a circular aperture, see Table 7.4, is $\alpha \approx \sin\alpha \approx 0.815 \cdot \lambda/R$. This results in $\alpha \approx 1.25 \times 10^{-6}$ radians at a wavelength of $\lambda = 500$ nm, and a diameter of a retro-reflector element of $D = 2R = 63$ mm (2.5 inches). Thus, for the customary size of retro-reflector elements, diffraction limitation is already close to the tolerable limits for long light paths.

7.5 Spectrometers/Interferometers for DOAS Systems

A central and critical component of all DOAS systems is a device which serves to separate the individual wavelength intervals, so that the intensity in these intervals can be measured. There are two fundamentally different approaches in use, spectrometers and interferometers.

Spectrometers separate radiation of different wavelengths into different spatial directions, where the spectrum can be measured by a spatially resolving detector (see Sect. 7.6). Spectrometers are based on two basic physical principles:

(a) Refraction by prisms (see Sect. 7.4.3), which rely on the dispersion in transparent optical materials such as quartz, glass, or plastic. Advantages of prism spectrometers are the absence of overlapping orders (as in the case of grating spectrometers). In addition, their wavelength separation (linear dispersion) is larger at shorter wavelengths. Disadvantages are limited resolution ($\lambda/\Delta\lambda <$ a few 10,000 for practical purposes) and a non-linear wavelength scale. Today, prism spectrometers are rarely used, although there may be many advantages in DOAS applications.

(b) Diffraction by gratings (see Sect. 7.5.1), which make use of spatial interference effects. Advantages of gratings are potentially very high resolution ($\lambda/\Delta\lambda$ in excess of 100,000 is possible), approximately linear dispersion, and the ability to build very simple instruments with concave gratings (see below). One disadvantage is the overlapping orders, i.e. a given point in the focal plane simultaneously receives light with wavelengths of $N \cdot \lambda$ (where $N = 1, 2, 3, \ldots$ denotes a positive integer).

Interferometers make use of interferometric principles to effectively produce (and record) the Fourier transform (FT) of the spectral intensity distribution of the received radiation. Although, in principle, spatial as well as temporal interferograms can be produced, in practice only the latter principle is in widespread use, see Sect. 7.5.3.

7.5.1 Diffraction Gratings

A grating can be viewed as a series of equally spaced slits (distance between slits = d), which transmit or reflect light, while the area in between does not. The angles β at which the rays, incident under angle α, from the slits interfere constructively are given by:

$$d\,(\sin\alpha + \sin\beta) = N\lambda. \tag{7.27}$$

The left side of (7.27) gives the optical phase difference (see Fig. 7.28) which, for constructive interference, must be equal to an integer (N) multiple of the wavelength λ. The integer N is called the **order** of the spectrum. In practice, reflective gratings are used instead of transmission gratings, as illustrated in

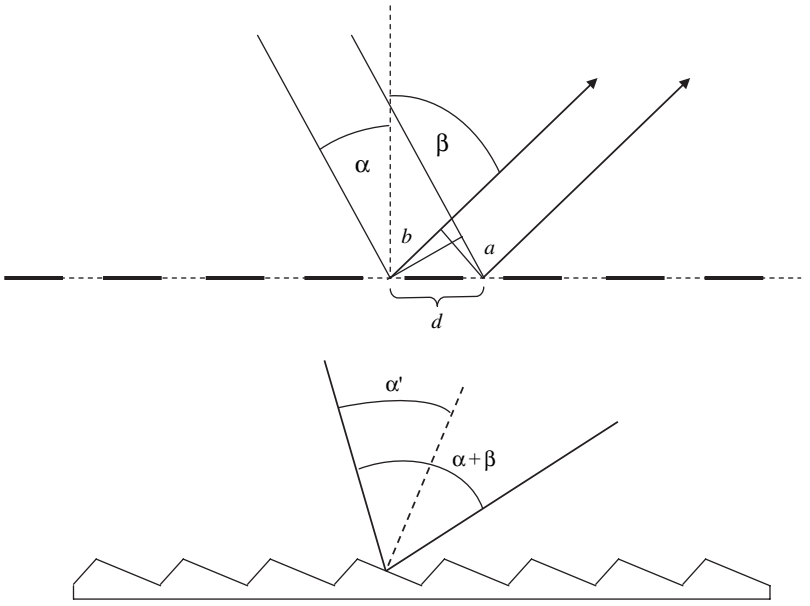

Fig. 7.28. Reflective diffraction grating. **Upper panel**: The optical path differences for the incident ray are $a = d \cdot \sin\alpha$, for the exiting ray $b = d \cdot \sin\beta$. The total path difference is $a + b$. **Lower panel**: The blaze angle of a grating is defined as the angle $\alpha + \beta$ where the refracted beam has the same direction as a specular reflected beam would have

Fig. 7.28. Orders with $N\lambda/d < 2$ can be observed, i.e. in first order d should be larger than $\lambda/2$.

The **angular dispersive power** is defined as the rate of change $\partial\beta/\partial\lambda$ of the angle of emergence β versus wavelength. For a given angle of incidence α and a given order N, we obtain:

$$\frac{\partial\beta}{\partial\lambda} = \frac{1}{d} \cdot \frac{N}{\cos\beta} = g \cdot \frac{N}{\cos\beta}. \tag{7.28}$$

The number of grooves per unit length (e.g. grooves per millimetre) $1/d$ is also known as **grating constant** g. Thus, $\partial\beta/\partial\lambda$ is independent of the angle of incidence, but increases with order and grating constant. It also becomes larger at large angles of emergence, where cos β is small. For instance, for an angle of emergence $\beta = 60°$ ($\cos\beta = 0.5$), $g = 1200$ grooves per millimetre ($d = 0.8333\,\mu\text{m}$ or $1/d = 1.2 \times 10^6\,\text{m}^{-1}$), and for first order one obtains $\partial\beta/\partial\lambda = 2.4 \times 10^6$ radians m^{-1} or 2.4×10^{-3} radians nm^{-1}. Thus, two parallel bundles of radiation with wavelength 1 nm apart will emerge as two bundles propagating at an angle of 2.4 mradians.

Ruled Versus Holographic Gratings: Depending on the manufacturing process, there are two popular types of gratings: ruled gratings and holographic gratings. The former are produced by mechanically drawing grooves into a suitable substrate. Since this is a lengthy process, the gratings commonly used in spectrometers are replicated from a ruled 'master' grating (sometimes in several generations). In contrast, holographic gratings (interference gratings) are produced by recording the interference pattern of two (laser) light beams, e.g. Lerner and Thevenon (1988). Since all grooves are formed simultaneously, holographic gratings are virtually free of random and periodic deviations in line positions, and thus they have no 'ghosts' (see below) and low levels of stray light. In addition, holographic techniques allow more freedom in producing gratings with uneven (continuously varying) line spacing. On the other hand, ruled gratings are more easily blazed, see below.

Gratings can be produced such that the reflecting surfaces are inclined with respect to the plane of the grating, as shown in the lower panel of Fig. 7.28. These gratings are known as 'blazed' gratings. The **blaze angle** of a grating is defined as the angle $\alpha + \beta$ where the refracted beam has the same direction as a beam, which is specular reflected from the sawtooth-shaped grooves of the grating (see Fig. 7.28, lower panel). For conditions where the angle between incident and refracted beam equals the blaze angle, the highest grating efficiency is achieved.

In principle, a grating distributes the incident radiation energy into an infinite number of orders. In practice, most of the energy is diffracted in a few or only one order (see blaze angle). The fraction of the incident energy reaching the strongest order is called the **efficiency** of the grating. Generally, the grating efficiency is a function of wavelength and the polarisation of the light. Typical maximum grating efficiencies are on the order of 20–80%.

For a particular application, it must be ensured that the grating efficiency is sufficient in the desired spectral range. Note that a low grating efficiency not only reduces the light throughput of the spectrometer, but may also considerably increase its stray light level, since low efficiency usually means that the missing radiation is diffracted in other orders.

Another point to watch, in particular in scattered light applications, where the incident radiation is usually partially polarised, is the polarisation dependence of the grating efficiency.

Grating Anomalies (Wood's Anomaly): Real gratings can exhibit a number of prominent deviations from the ideal behaviour described earlier. In particular, individual grooves (or groups of grooves) can be misplaced randomly or periodically. The latter imperfection gives rise to **grating ghosts**. An example for grating ghosts is the Rowland ghost caused by periodic misplacement of lines in the ruled grating. If we assume that each nth line is displaced by an amount $\Delta d << d$ from its nominal distance d to its neighbouring line, then the resulting grating can be viewed as an overlay of three gratings with slightly different line spacing $d - \Delta d$, d, and $d + \Delta d$. Such a grating will consequently produce two additional spectra, or 'ghosts', i.e. each spectral line will have two satellites.

An anomaly of a different kind is the **Wood anomaly** (discovered by R. W. Wood, 1902). Many gratings show sharp changes of the diffracted intensity within narrow spectral regions. Typical reflection gratings produce a series of orders of diffracted light. At some critical wavelength, the diffracted light falls back into the plane of the grating. The light which would be sent into the forbidden region is redistributed back into the allowed orders, and appears as an addition to the spectral response, with a sharp increase at the critical wavelength and a steep decline to the red. This effect acts as an enhancement of the grating efficiency, as if the light from two orders are combined. A Wood's anomaly is almost entirely polarised perpendicular to the grating grooves.

7.5.2 Spectrometers

The purpose of a **spectrometer** is to separate and re-image radiation of different wavelengths in order to record spectral signatures. In principle, this can be done in several ways. For instance, by a scanning **monochromator**, which selects and transmits a narrow spectral interval of the incoming radiation, in connection with a suitable detector. A monochromator can be thought of as an (usually adjustable) optical band-pass filter. Alternatively, a **spectrograph**, which images a range of wavelengths at the exit focal plane for detection by multi-channel detector or photographic film, can be used. Since spectrometer is the more general term, we shall use this term in the following.

Traditionally, the spectrometer of a DOAS instrument produces a 'spectrum' i.e. spatially separates the radiation into wavelength intervals, so that the intensity in the different wavelength intervals can be recorded by a suitable detector capable of resolving spatial differences in radiation intensity. The latter task can be performed by detectors using moving parts to convert spatial separation in temporal separation (e.g. a moving exit slit), or – in recent designs – by a collection of many sensors (detector arrays) that simultaneously record spatial variations in intensities.

It should be noted, however, that generation of classical spectra is not really required for DOAS applications, rather a discernible signature must be generated that allows distinction between relevant atmospheric absorbers and recording of their presence in the light path with sufficient sensitivity.

A step in this direction was made by early COSPEC spectrometers (e.g. Millan, 1972), which used multiple entrance slits paced to superimpose periodic trace gas (e.g. SO_2) spectra in phase.

As mentioned earlier, the 'classic' spectrometer design rests on the two optical principles of prism spectrometers and grating spectrometers, which are used in several design variants.

The Prism Spectrometer: In the early days of optical spectroscopy (e.g. Dobson, 1926), prism spectrometers (see Fig. 7.29) were the instrument of choice. The angular dispersion is given by (7.17). In recent decades, the grating spectrometer has become the dominating spectrometer design principle. This is due to its inherent advantages, such as the almost linear dispersion curve [see (7.28)], and the higher resolution at a given size of the instrument combined with great advances in manufacturing of diffraction gratings. Nevertheless, it should be said that the prism spectrometer has some merits which may make it worthwhile to consider its future use in DOAS systems: The non-linearity of the dispersion can be corrected with modern software, in fact higher resolution would usually be required in the UV than in the visible spectral range. Also the absence of higher orders could be an advantage.

Plane Grating Spectrometers: The Czerny–Turner-type spectrometer (see Fig. 7.30a) and variants have been traditionally selected for DOAS instruments (e.g. Platt et al., 1979; Platt and Perner, 1983). Besides the grating, it requires at least two additional reflecting surfaces (collimating and camera

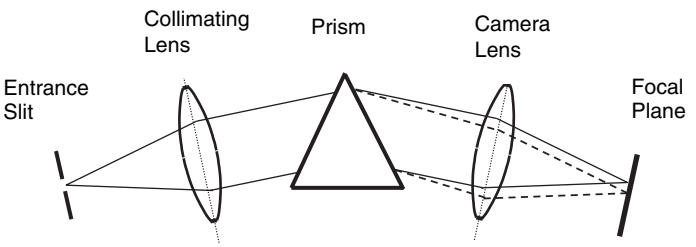

Fig. 7.29. Optical outline of a typical prism spectrometer

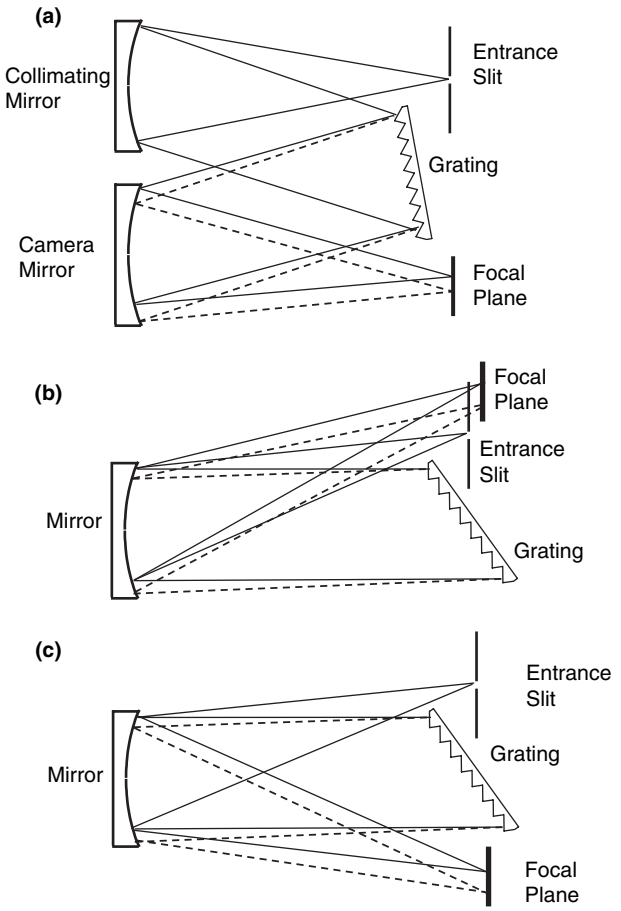

Fig. 7.30. Optical outlines of different variants of grating spectrometers. (**a**) Czerny–Turner; (**b**)Littrow; (**c**) Fastie–Ebert

mirror). The additional reflection losses at these surfaces are usually offset by high-efficiency (60–80%) plane blazed gratings. Furthermore, the wavelength range is readily selected by rotating the grating.

Since most of the incident light is directed into the desired diffraction order, stray light caused by reflection of unwanted orders off the spectrometer housing is minimised. The linear dispersion $\partial s/\partial\lambda$ of a grating spectrometer is given by $\partial\beta/\partial\lambda$ (7.28) multiplied by the focal length of the camera mirror:

$$\frac{\partial s}{\partial\lambda} = f\frac{\partial\beta}{\partial\lambda} = \frac{f}{d}\cdot\frac{N}{\cos\beta} = fg\cdot\frac{N}{\cos\beta}. \tag{7.29}$$

In special applications, for example if only a small aperture is required, Fastie–Ebert-type (Fig. 7.30c) or Littrow-type spectrometers (Fig. 7.30b) are also

often used. While the design of these spectrometer types appears to be simpler, since a single mirror doubles as collimating mirror and camera mirror, the disadvantages include larger size (in the case of Fastie–Ebert) and the requirement to work at a wavelength where the angle of incidence and the angle of refraction of the grating are equal (Littrow-type spectrometer).

Concave (Holographic) Grating Spectrometers: Modern holographic grating technology (see Sect. 7.5.1) allows the design of spectrometers only consisting of entrance slit, concave grating, and detector (i.e. optomechanical scanning device (OSD) or diode array, see Fig. 7.31 and Sect. 7.6). In contrast to the traditional Rowland mounting, that also uses a concave grating as the only imaging element in the spectrometer, modern concave holographic gratings can produce a flat spectrum over a certain range (hence the name flat-field spectrometers).

The partly low efficiency of most holographic gratings (20–40%, see Sect. 7.5.1) is compensated by the reduced losses due to the low number of optical surfaces. While the stray light produced by holographic gratings is lower compared to ruled gratings, the higher intensity of unwanted orders may increase the stray light level in the spectrometer. On the other hand, the unused orders are also focused and can thus be removed relatively easily by light traps. A disadvantage of most flat field gratings is their limitation to a relatively small spectral range that cannot normally be changed.

Imaging Spectrometers: The term 'imaging spectrometer' refers to spectrometers that can image a position along the entrance slit onto a corresponding position in the focal plane. The imaging direction is perpendicular to the dispersion direction. Thus, usually two-dimensional detectors (typically 2D CCD detectors) in the focal plane record multiple spectra and each point along the entrance slit corresponds to an individual spectrum in the

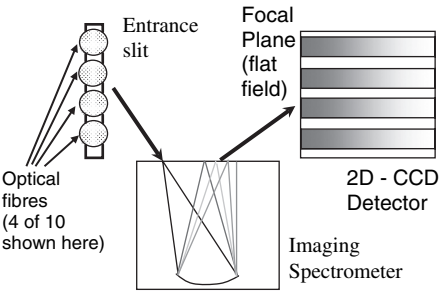

Fig. 7.31. Sketch of an imaging spectrometer. Here, a concave grating spectrometer is shown. But, in principle, any type of spectrometer can be used. In this example, $n_y = 4$ optical fibres could connect to four individual telescopes looking at different viewing angles. In reality, frequently larger numbers of fibres (e.g. 10; Heismann, 1996) are present (figure courtesy of T. Wagner)

focal plane. As illustrated in Fig. 7.31, there are n_x pixels in the 'dispersion direction' determining the spectral sampling, similar to a one-dimensional diode array (or CCD detector). In the 'slit direction', n_y rows of n_x pixels each provides spatial resolution. Theoretically, the imaging spectrometer behaves like n_y individual spectrometers, each with a spectral sampling of n_x pixels (the spectral resolution of course will depend on dispersion and instrument function). In practice, the imaging qualities of most spectrometers perpendicular to the dispersion direction are limited to many pixels in y direction.

To date, imaging spectrometers are used in several applications:

- MAX-DOAS (see also Sect. 7.10.3). In this application, a column of fibre exits illuminates the entrance slit. Each fibre (or set of fibres) is coupled to a telescope observing the sky under an individual angle.
- One-dimensional imaging in order to resolve e.g. vertical trace gas profiles.
- Two-dimensional spectral imaging. Since only one dimension is covered by the slit, other scanning mechanisms (e.g. mechanical; Lohberger et al., 2004) must be employed by the other dimension. An example is a satellite or aircraft, the movement of which provides the second scanning dimension (e.g. Laan et al., 2000; Levelt et al., 2000).

Applications such as these can be seen as generating 'super colour images', where each pixel has not just three colours, but encompasses an entire spectrum with several hundred (or more) spectral elements.

7.5.3 Interferometers (FT Spectrometry)

Interferometers make use of the wave properties of electromagnetic radiation in order to effectively produce (and record) the Fourier Transform (FT) of the spectral intensity distribution in the received radiation. Therefore, interferometers are frequently called FT spectrometers. Although, in principle spatial as well as temporal interferograms can be produced in practice essentially all instruments are based on the latter principle (see Fig. 7.32).

FT spectrometers have been in use for IR absorption spectroscopy for a long time (FT-IR) (e.g. Tuazon et al., 1980; Galle et al., 1994; Notholt et al., 1997; Hanst and Hanst, 1994). However, technological advances have only recently made their application in the UV/visible spectral range (now called FT-UV), and thus for DOAS, possible (Colin et al., 1991; Vandaele et al., 1992).

7.5.4 Characteristics of Spectrometers

As shown earlier, there are a large variety of spectrometer designs with widely varying characteristics, such as:

Spectral dispersion – The spatial separation of radiation of different wavelengths in the focal plane of the instrument is referred to as spectral

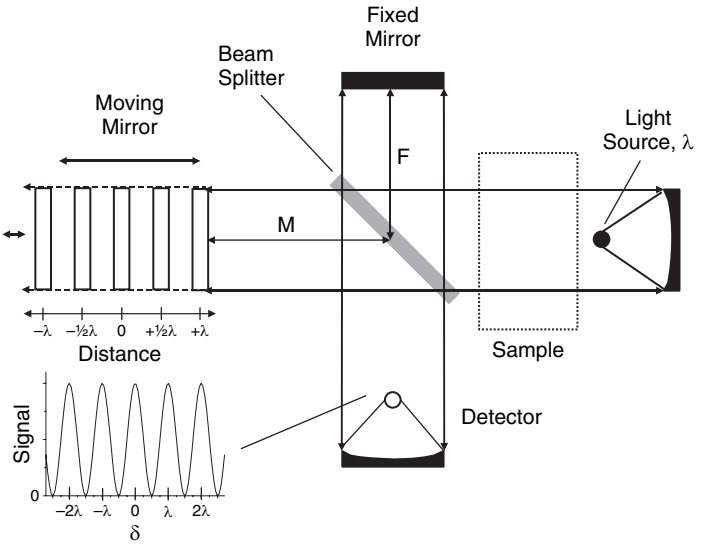

Fig. 7.32. Optical outline of a FT spectrometer

dispersion. This dispersion is given by $ds/d\lambda$ measured in, e.g., mm/nm, where s denotes the linear distance in the focal plane and λ the wavelength, see (7.29).

Spectral resolution – The capability of the instrument to separately measure the radiation intensity at different wavelengths is characterized by the spectral resolution, $\Delta\lambda_R$. There are several definitions of the spectral resolution, usually based on the capability to separate the intensity of two monochromatic light sources (atomic emission lines) simultaneously observed by the instrument. A more general and meaningful term is the instrument function [or slit function $H(\lambda–\lambda_0)$ at the wavelength λ_0], which is defined as the instrument's response to a delta function $\delta(\lambda–\lambda_0)$ as input intensity distribution. The **spectral resolution** $\Delta\lambda_R$ at the wavelength λ_0 can be seen as e.g. the half-width of $H(\lambda–\lambda_0)$.

Flatness – Flatness of the focal plane determines how the spectral characteristics change in the focal plane. This determines how well a 1D or 2D detector of a given size can be accommodated. Typically the focal plane is reasonably flat in the dispersion direction (i.e. over ∼25 mm or more). Imaging spectrometers are necessary to achieve a flat field perpendicular to the dispersion direction.

Thermal Stability – Experience and theoretical calculations show that even slight variations in the position of a recorded atmospheric spectrum with respect to a reference spectrum can lead to relatively large errors in the spectral fit (see Chap. 8). Changes in dispersion have the same effect, since they lead to spectral shift of one portion of the spectrum compared to another.

In practice, shifts or dispersion changes as small as 0.01, spectral pixels can lead to noticeable degradation of detection limits and accuracy of DOAS instruments. Although shift and change in dispersion can be compensated for by evaluation software (see Chap. 8), occurrence of these effects will always degrade the result. It is, therefore, of great advantage to minimise spectral shift and change in dispersion. In practice, these effects are largely caused by a change in the temperature of the spectrometer. Thus, either the susceptibility of spectrometers to temperature changes should be minimised (e.g. by use of material with low thermal expansion) and/or the temperature changes must be kept at a minimum. However, air density changes due to changes in temperature also lead to a small drift as is explained below.

Although efforts are being made to design spectrometers, with low thermal effects (e.g. made from Zerodur), the most widely used approach is to thermostate the entire spectrometer subsystem. This is usually accomplished by insulating the instrument and heating it to a temperature above the highest expected ambient temperature. Typical temperature stabilities reached in field experiments are on the order of ±0.1–1 K. Typical wavelength shifts are 0.05 nm/degree. Thermostating the detector is usually reached as a by-product of the necessary cooling. In some designs, both functions were combined by cooling and thermostating at a low temperature the entire spectrometer–detector assembly (Hönninger, 2002; Bobrowski et al., 2003).

Pressure (Air Density) Effects – Changes in ambient atmospheric pressure (and temperature) will usually also lead to a wavelength shift since the index of refraction of air n_{air} (p, T), the speed of light, and thus the wavelength of the radiation changes, see (7.10).

$$\lambda = \frac{c}{\nu} = \frac{c_0}{\nu} \cdot \frac{1}{n_{\mathrm{air}}}. \tag{7.30}$$

In a grating spectrometer, this will alter the dispersion of the instrument.

Stray Light – Stray light requires careful consideration when selecting or designing a spectrometer. Sources of stray light include: Light scattered from optical elements (grating and mirrors), reflection of unused diffraction orders off the spectrometer walls, reflection of unused portions of the spectrum from walls near the focal plane, and reflections from the detector surface (e.g. Pierson and Goldstein, 1989). A particular form of stray light is due to 'grating ghosts', i.e. portions of radiation diffracted in unwanted directions (see Sect. 7.5.1). An important source of stray light is due to incorrect illumination of the spectrometer. If the F-number of the illumination exceeds that of the spectrometer, radiation will overfill the collimating mirror and hit interior walls of the spectrometer, where it can be reflected to the detector.

Note that stray light tends to be comparatively high in spectrometers filtering a relatively broad wavelength interval from a continuous spectrum, as in DOAS applications. To illustrate this point, we consider a typical stray

light level of 10^{-5} for a Czerny–Turner spectrometer (Pierson and Goldstein, 1989). This figure gives the fractional light intensity found anywhere in the spectrum when a single (laser) line of very narrow spectral width enters the spectrometer. The actual width of the line seen in the focal plane will then be equal to the spectral resolution of the instrument. Continuous light entering the spectrometer can be thought of being composed of a series of lines spaced at center-to-center distances equal to their width (i.e. the spectral resolution of the instrument). Since the total spectral range of light entering the spectrometer (for instance from 300 to 600 nm) is on the order of 1000 times larger than the spectral resolution (of typically 0.3 nm for a low resolution DOAS instrument) the level of stray light (per wavelength interval) is roughly three orders of magnitude larger than would be expected from the single line definition usually considered. Thus, in DOAS applications, stray light levels I_{SL}/I can be expected to be closer to 10^{-2} than to 10^{-5}. The effect of stray light is to reduce the recorded optical density D, as shown in Sect. 8.7.2.

Reentrant Light: In many spectrometers (irrespective of type) where a linear or matrix solid-state detector array is used, there might be reflection of radiation from the detector surface back to the grating. The solution is to either tilt the array up to the point that the resolution begins to degrade or, if the system is being designed for the first time, to work out of plane.

In some Czerny–Turner spectrometers, a diffracted wavelength other than that at which the instrument is set may hit the collimating mirror (see Fig. 7.30) and be reflected back to the grating, where it may be rediffracted and directed to the detector. If this problem is serious, a good solution is to place a mask perpendicular to the grooves across the centre of the grating. The mask should be the same height as the entrance slit (and detector array). If the wavelength is known, it is possible to calculate the point on the grating where the radiation of the reflected wavelength hits. In this case, the only masking necessary is at that point.

Light Throughput of Spectrometers – An important characteristic of any spectrometer is its light throughput, L_{t}. It is defined as the product of acceptance solid angle Ω, effective entrance aperture A (i.e. the area of the entrance slit), and the light transmission T of the instrument:

$$L_{\mathrm{t}} = \Omega \cdot A \cdot T = E \cdot T \,(E = \text{Entendue, see Sect. 7.4.5})$$

In principle, L_{t} is affected by many parameters including:

- The aperture ratio ($f/\#$) of the instrument
- The entrance slit dimensions
- The light losses inside the instrument.

It is interesting to note that the light throughput is approximately inversely proportional to the square of the spectral resolution, which scales with the

width, and thus the areas A of both the entrance slit and the detector pixels. Thus, $L_t \propto 1/\Delta\lambda_R$.

7.6 Detectors for UV/Visual Spectrometers

The basic function of detectors for UV/vis spectrometers is to convert spatial radiation intensity differences $I(\lambda)$ into a signal $I_D(\lambda)$ that can be transferred to a computer for further evaluation.

$$I_D(\lambda) = \alpha \cdot I(\lambda), \tag{7.31}$$

where α denotes the detector sensitivity. Detectors must rapidly capture a spectrum (quasi-) simultaneously in order to minimise additional noise due to atmospheric turbulence. Good quantum efficiency is also desirable. However, the most significant requirement is the capability to reliably detect relative intensity differences within the spectrum on the order of 10^{-4}. This latter requirement implies low noise and excellent linearity (see below), as well as sufficient sampling of the information. Presently, several different detector designs are in use for DOAS spectrometers. OSDs, which record the spectra sequentially, make use of only a small fraction of the light, and thus can be regarded as outdated for scientific applications. However OSDs are still found in several commercial DOAS instrument designs. Recent scientific instruments employ solid-state detector arrays known as photo diode array (PDA) detectors, CCD array detectors, and complementary metal oxide semiconductor (CMOS) array detectors.

7.6.1 Geometrical Focal Plane Sampling Requirements

The requirements for DOAS sensors can be described by a number of properties:

Geometry – For spectroscopic purposes, pixels with an aspect ratio that is ratio narrow in the direction of the scan (i.e. dispersion direction of the spectrometer) and wide in the direction perpendicular to the scan are required. Typically, a pixel width of a fraction (say 1/6th, see below) of the width of the spatial instrument function is desirable. The spatial instrument function is the resulting spatial intensity distribution in the focal plane of a spectrometer as a response to a delta peak of monochromatic light at the entrance of the spectrometer.

Taking an entrance slit width of 50 µm corresponding to, for example, a width of the spatial instrument function of 75 µm, a detector pixel width on the order of $w_D = 15\,\mu m$ would be required.

On the other hand, the 'height' (extension perpendicular to scan direction or dispersion direction) of each pixel should be at least as large as the height

h_S of the illuminated area in the focal plane. For a typical case of a one-to-one imaging spectrometer, h_S is at least as large as the illuminated height of the entrance slit. For active DOAS systems employing an optical fibre (or fibre bundle) to transfer the light from the receiving telescope to the spectrometer h_S (and therefore the detector height h_D), is around 100 µm to 500 µm (see Sect. 7.4.7). For passive systems observing the scattered sky light, the imaged object (i.e. the sky) is very large and the light throughput is limited by the entrance area of the spectrometer (and its aperture ratio, which we shall not consider here). Since the slit width is determined by the required spectral resolution, the only free parameter is the slit height, which should be maximised. Thus, large pixel heights h_D of the order of several millimetres are of advantage.

Readout Time – In active DOAS applications with large optics (see Sect. 7.9.3) a signal level in the spectrometer focal plane of 10^9 photoelectrons per second and 25 µm resolution element can be reached. For passive DOAS systems observing scattered sunlight (zenith or off-axis geometry), typical signal levels are about two orders of magnitude longer. The detector readout has to be fast enough to keep up with the signal accumulation. In fact it would be desirable that the actual readout time is short compared to the exposure time required to fill the detector pixels near full-well capacity. The full-well capacitance of a typical (one-dimensional) CCD detector is of the order of 10^5 electrons (see Table 7.6), this means that in active DOAS applications, up to 10^4 complete readout processes per second may be required. For a 2000-element linear CCD sensor, this figure would correspond to about 20 MHz pixel frequency. This might be by a factor of 4 better for the CCD's listed in Table 7.6, because their pixel width – and thus signal intensity – is a factor of 2 lower than assumed (13 or 14 µm instead of 25 µm as assumed earlier), but still some CCDs fall short by a factor of 5 from the above requirement. In particular for 2D-CCD arrays, which have comparable full well capacities, the readout time can be a limitation.

Photodiode arrays have a much larger full well capacity of $6\times10^7-1.2\times10^8$ electrons per pixel and the read out times can be considerably lower. However, due to their electronic layout, the readout frequency is typically limited to ∼100 kHz.

Co-adding Readouts and Exposure Time – In order to achieve the desired signal-to-noise ratios (e.g. $R = 10^4$), a sufficiently large number N of photoelectrons needs to be recorded so that $N > R^2$ and $N > B$(B = combined effects of all fixed noise sources, e.g. detector readout noise and preamplifier noise), see (7.50). Frequently, the desired number of photoelectrons cannot be accumulated in a single scan, and thus several scans have to be co-added (see Sects. 7.6.2 and 7.6.3). For a good N/B ratio of a single scan, a signal level not too much below the maximum detector signal is desirable. On the other hand, 'overexposure' e.g. a signal larger than the maximum allowable detector signal (e.g. due to pixel saturation or ADC overload) must be avoided. Various schemes for 'exposure control' have been developed, mostly

Table 7.6. The characteristics of PDAs versus CCD and CMOS sensors

Type	PDA	CCD	CMOS
Characteristic Geometry	1-D only	Available in 2-D (usually) and 1-D	Available in 2-D (usually) and 1-D
Readout Noise (electrons)	High readout noise (several 10^3 electrons)	Low readout noise ($\approx$ 1–20 electrons)	Low readout noise ($\approx$ 10 electrons)
Typical pixel capacity (electrons)	10^8	10^5	10^5
Typical noise due to photoelectron statistics, relative S/N	10^4	300	300
	10^{-4}	3×10^{-3}	3×10^{-3}
Dominant noise source	Photoelectron statistics, if full well capacity can be used	Usually photoelectron statistics	Usually photoelectron statistics
Dark current	100–1000 s to saturate pixel	100–1000 s to saturate pixel	100–1000 s to saturate pixel
Signal-dependent dark current	Yes	Yes	Unknown
Typical readout time	20 ms	10 ms to 1 s (2-D)	10 ms to 1 s (2-D)
Spectral range	NIR (Silicon limit) to UV (200 nm)	NIR (Silicon limit) to UV, many types	
Quantum efficiency	Good	Excellent (back-thinned arrays)	Good
On-chip ADC available	No	No	Yes

based on predicting the future signal on the basis of the already recorded signal. The magnitude of the signal is usually controlled by PMT high voltage (for optomechanical detectors) or exposure time (for solid-state detectors). If radiation signals are fluctuating in intensity, as can occur in many active and passive DOAS applications, overexposure cannot always be avoided. In this case, overexposed spectra must be discarded. Note that each individual spectrum must be checked for overexposure, since it may not be detectable

after a few overexposed spectra are 'buried' under a large number of (properly exposed) co-added spectra.

Spectral Sensitivity – Detector must be sufficiently sensitive in the spectral range of interest. For most classical DOAS applications, a spectral range from about 200 to 800 nm is required to cover typical applications (see Chap. 6 and Appendix B). Recent applications, however, extend this range into the near-infrared. Silicon allows measurements from below 200 nm up to about 1100 nm, where the upper wavelength end is set by the band gap of silicon. For measurements at longer wavelengths, detectors based on other semiconductor materials are used. A popular material for wavelengths, up to 1600 nm or even 2400 nm is InGaAs. Single elements and linear arrays based on this material are available.

For PMTs, the long wavelength end of the sensitivity range is given by the requirement that the photon energy must exceed the work function, i.e. work to release an electron from the cathode material. Modern cathode materials (e.g. multi-alkali) give sensitivities to about 600 nm. In contrast, the short wavelength end of the sensitivity range is set by the window material. Glass windows will give about 400 nm, quartz windows <200 nm range.

The detector spectral sensitivity is frequently expressed in terms of the quantum efficiency Q:

$$Q = \frac{\text{Number of photoelectrons}}{\text{Number of photons}}. \tag{7.32}$$

Spectral Sampling – In order to obtain a true digital representation of the spectrum projected into the focal plane of the spectrometer, sufficiently fine spectral sampling is required. Obviously, the spatial frequency (e.g. density of detector pixels) should match the spectral resolution of the dispersing instrument. In other words, there must be a sufficient density of pixels compared to the spectral resolution. A rule of thumb is that the spectral width of a detector pixel should be about 10–20% of the FWHM of the instrument function (see Chap. 8). Details are discussed in the following and e.g. by Hofmann et al. (1995), Stutz (1996), Roscoe et al. (1996), and Chance et al. (2005).

Aliasing problems – Aliasing problems are well known from many areas of electronic signal evaluation. Aliasing will arise in cases where the spectral resolution is too high for a given number of detector pixels in the focal plane of the spectrometer (or if there are too few pixels in the focal plane sensor in comparison with the spectral resolution of the spectrometer). Fig. 7.33 illustrates this problem for the case of discrete absorption lines. In this example, the position of an emission line (smooth Gaussian in A) is shifted by the half-width of a pixel (B). As can be seen, there can be a drastic change in line shape of the digitised representation, shown as a histogram-like curve in panels A and B, which actually describe the same line shape.

It is tempting to make 'best possible use' of a given number of pixels and thus to specify only the minimal twofold oversampling (Nyquist criterion). However, practical experience and numerical modelling show there must be

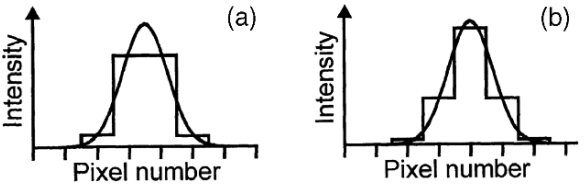

Fig. 7.33. Aliasing problems occur if there are too few pixels in the focal plane sensor in comparison with the spectral resolution of the spectrometer. If in this example, the position of an emission line (**a**) is shifted by a half width of a pixel (**b**), there can be a drastic change in line shape of the digitised representation. The histogram-like curve in panels A and B actually describe the same line shape

a sufficiently large number of signal samples $I(i)$ (or detector pixels) across one 'resolution interval'. Sample calculations demonstrate that on the order of 5–10 samples per resolution interval lead to acceptable errors (Hofmann et al., 1995; Stutz, 1996; Roscoe et al., 1996; Platt et al., 1997). In principle, advanced interpolation techniques and other procedures can be used to correct for this problem (e.g. DOAS evaluation of GOME spectra, Chance et al., 2005).

Detector Linearity – Detector linearity is a prerequisite for good sensitivity and measurement precision of DOAS systems. It can be described as:

$$I_{\mathrm{D}}(i) = \alpha \cdot I(i) \quad or \quad \frac{dI_{\mathrm{D}}(i)}{dI(i)} = \alpha = \text{constant}, \tag{7.33}$$

where $I_{\mathrm{D}}(i)$ denotes the signal generated by the ith detector pixel, while $I(i)$ is the radiation intensity reaching this pixel (see Chap. 8). The effect of nonlinearity, i.e. the sensitivity α varying as a function of the radiation intensity I, is illustrated by the following consideration. In the limit of small optical densities, the (differential) optical density D of a spectral structure is given by:

$$D = \ln \frac{I_0}{I} \approx \frac{I_0}{I} - 1 = \frac{I_0 - 1}{I} = \frac{\Delta I}{I}. \tag{7.34}$$

In a practical measurement, however, I can only be estimated from the detector signal I_{D}:

$$D_{\mathrm{D}} \approx \frac{\Delta I_{\mathrm{D}}}{I_{\mathrm{D}}}.$$

Assuming for the sake of simplicity, two different sensitivities α_1 and α_2 for low and high signals, respectively (see Fig. 7.34), we obtain:

$$D_{\mathrm{D}} \approx \frac{\Delta S_{\mathrm{D}}}{S_{\mathrm{D}}} = \frac{\alpha_2 \Delta I}{\alpha_1 I} = \frac{\alpha_2}{\alpha_1} \cdot D. \tag{7.35}$$

Thus, the measured optical density (and consequently trace gas level) would deviate from the true value by the factor α_2/α_1. This could be interpreted as

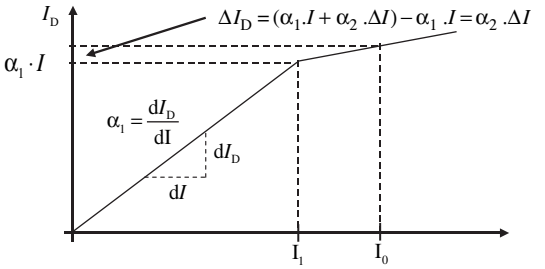

Fig. 7.34. Insufficient linearity of a detector can cause incorrect determinations of the optical density

the following requirement: If a 1% precision of the trace gas level is desired, the sensitivity $\alpha(I)$ cannot deviate more than 1% from its average value at any I. While this may be sufficient if there is only one dominating absorber present, there might be problems if weak spectral structures are to be detected in the presence of strong ones. For instance, in passive DOAS systems most absorbers are weak compared to the Fraunhofer bands. Here, distortion of the strong spectral structure due to non-linearity of the detector can introduce large errors in the determination of weak spectral absorption structures. Consequently, a much better detector linearity than estimated above might be required.

7.6.2 Optomechanical Scanning Devices and Photomultiplier Tube

Optomechanical scanning devices scan a section of the dispersed spectrum, typically several nanometres to 100 nm, in the focal plane of the spectrograph by a moving exit slit, as shown in Fig. 7.35. In the most common design, radial slits are etched in a thin metal disk ('slotted disk') rotating in the focal plane (see Fig. 7.36). At a given time, one particular slit serves as an exit slit. The start of a scan is determined by an infrared light barrier. The light passing through this slit is received by a photomultiplier tube (PMT), the output signal of which is digitised by a high-speed ADC and recorded by a computer. The signal is adapted to the ADC range by variable preamplifier gain and/or changing the PMT high voltage. During one scan (i.e., one sweep of an exit slit over the spectral interval of interest), several hundred digitised signal samples are taken. Consecutive scans are performed at a rate of typically 100 scans per second, and are digitised into 500–1000 'channels', which are signal averaged by the software (thus individual samples of the signal are recorded at 50–100 kHz frequency), thereby meeting the requirement of detection of very small signal differences.

Alternatively, vibrating exit slits can be used. However, disadvantages include less uniform scanning speed and possible influences of the vibration on other parts of the optics.

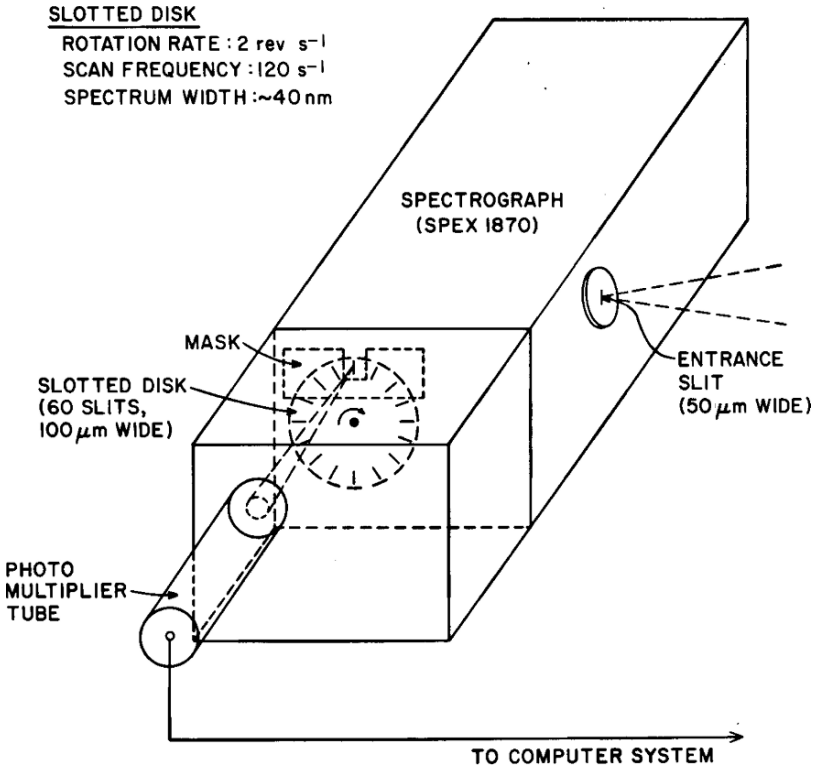

Fig. 7.35. Sketch of an OSD, the 'slotted disk' design. A series of (in this case 60) radial slits are etched in a thin metal disk (*'slotted disk'*) rotating in the focal plane.

Since a single scan takes ≈10 ms, the effect of atmospheric scintillations is negligible, because the frequency spectrum of atmospheric turbulence close to the ground peaks around 0.1–1 Hz and contains very little energy at frequencies above 10 Hz. In addition, typical spectra obtained during several minutes of integration time represent an average over 10,000–40,000 individual scans. Thus, effects of noise and temporal signal variations are very effectively suppressed. In fact, even momentarily blocking the light beam entirely (e.g., due to a vehicle driving through the beam) has no noticeable effect on the spectrum.

The main disadvantage of the optomechanical scanning of absorption spectra is the large multiplex loss, since only the section of the spectrum passing through the exit slit reaches the detector. Only on the order of 1% of the light is utilised, making relatively long integration times necessary.

The conversion of the radiation intensity to a detector signal is performed by the PMT. The design of the voltage divider chain supplying the voltages for the dynodes of the PMT is important. Since DOAS detectors are 'high anode current' applications (anode currents can reach $I_A = 100\,\mu A$), relatively high

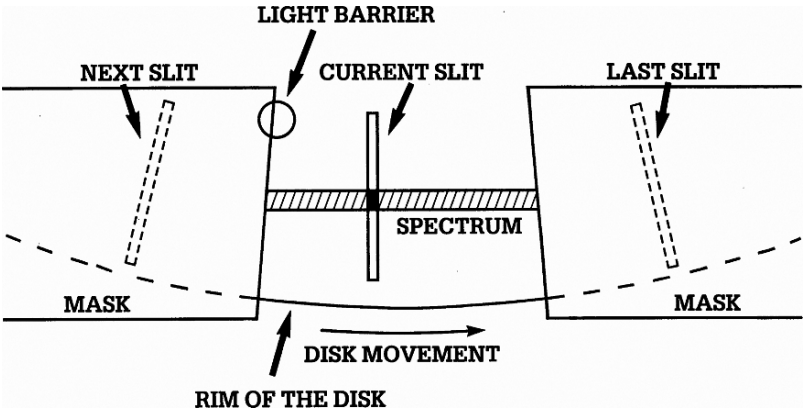

Fig. 7.36. OSD, the'slotted disk'. A mask allows only one slit to serve as an exit slit at any given time. The start of a scan is signalled by an infrared light barrier. The light passing through this slit is received by a PMT. (from Platt and Perner, 1983)

currents in the voltage divider (at least $10 \cdot I_A$) are required in order to not compromise detector linearity (see Sect. 7.6.1). Alternatively 'active voltage dividers' using transistors can be employed. Another important aspect is the response of the PMT electronics to transients. Commercial voltage dividers frequently employ capacitors between dynodes to improve response for light pulses; this is not needed or desirable for DOAS applications. However, PMT detectors are inherently fast response devices, so a low-pass filter is usually required before or within the preamplifier, supplying a time constant roughly equivalent to the time to record one detector pixel (typically $\tau \approx 20\,\mu s$). Finally, PMT photocathodes must be chosen according to the desired long wavelength end of the response. In general, cathodes with higher sensitivity at longer wavelength have higher dark currents. Available cathodes (e.g. multialkali, S20) limit the spectral range to the long wavelength end of the visible range.

7.6.3 Solid-state Array Detectors and Characteristics

Solid-state detector arrays consist of a large number, typically several hundred or more, of individual photodetectors (i.e. photodiodes) arranged in a linear row or in a two-dimensional, matrix-like fashion. They are, in principle, far superior to OSD in recording absorption spectra, since radiation of all wavelengths is recorded simultaneously rather than sequentially. This so-called 'multiplex advantage' amounts to about two orders of magnitude more photons recorded in typical systems. Accordingly, the measurement time can be shortened by the same factor or, alternatively the photon noise be reduced by about one order of magnitude. Additional advantages include the absence

of moving parts, and nearly simultaneous sampling of all wavelength intervals. In addition, no high voltage is required and the quantum efficiency (at least in the red and near-infrared spectral regions) is better than that of most PMT cathodes (see e.g. Yates and Kuwana, 1976).

There are three basic designs of solid-state multi-element photodetectors, which are sketched in Fig. 7.37: PDA, CCD, and CMOS devices. Either design principle allows construction of linear or two-dimensional arrangements of hundreds to many thousands of individual photosensors, which can be read out sequentially.

In the case of **PDAs**, individual photodiodes are arranged on a silicon chip, and are read out by sequentially connecting them (via a field effect transistor) one by one to a common readout line, that conducts the accumulated charge to a readout amplifier. There may be more than one readout line (e.g. one for all even numbered, one for all odd-numbered diodes), and thus the readout time is reduced accordingly. PDAs are usually only available as one-dimensional (linear) arrays.

In contrast, **CCDs** have no readout line. Rather, the charge of each sensor is sequentially transferred through all pixels until it reaches a readout amplifier connected to the very last pixel in the row. Advantages of CCDs over PDAs include a simpler design, since no readout transistors and associated driving circuits are required, combined with much smaller output capacitance. The output capacitance is equivalent to one pixel, while the capacitance of a typical PDA readout line is equivalent to dozens or hundreds of pixels. As a consequence, the readout noise of a typical CCD is about two orders of magnitude lower than that of a PDA (see Table 7.6). On the other hand, the charge transfer efficiency of CCDs is limited to values of typically 99.999%, leading to some cross-talk between pixels, which is absent in PDAs. Usually, CCDs are produced as linear (1D) or area (2D) sensors. In the latter case, they provide additional information, which can be utilised e.g. to simultaneously record several spectra. However, the capacitance of the individual elements is much larger in PDAs, as outlined in Table 7.6. Therefore, the total noise can be limited by photoelectron shot noise, despite the higher readout noise of PDAs.

CMOS sensors are similar to PDAs, in that they are read out by sequentially connecting the individual pixels (via a field-effect transistors) one by one to a common readout line, which conducts the accumulated signal to a readout terminal. In contrast to PDAs, amplifiers (and sometimes reset gates) are frequently integrated directly at each pixel. Another advantage is that the CMOS process allows integration of other devices such as amplifiers and ADC directly on the sensor chip. There is also typically random access to each pixel. If amplifiers are attached to each pixel non-destructive readout is possible, allowing simple 'exposure control'.

A more subtle point concerns possible differences in exposure times for the different pixels. In PDAs, all pixels have the same length of exposure, but the time intervals do not quite overlap since exposure takes place from

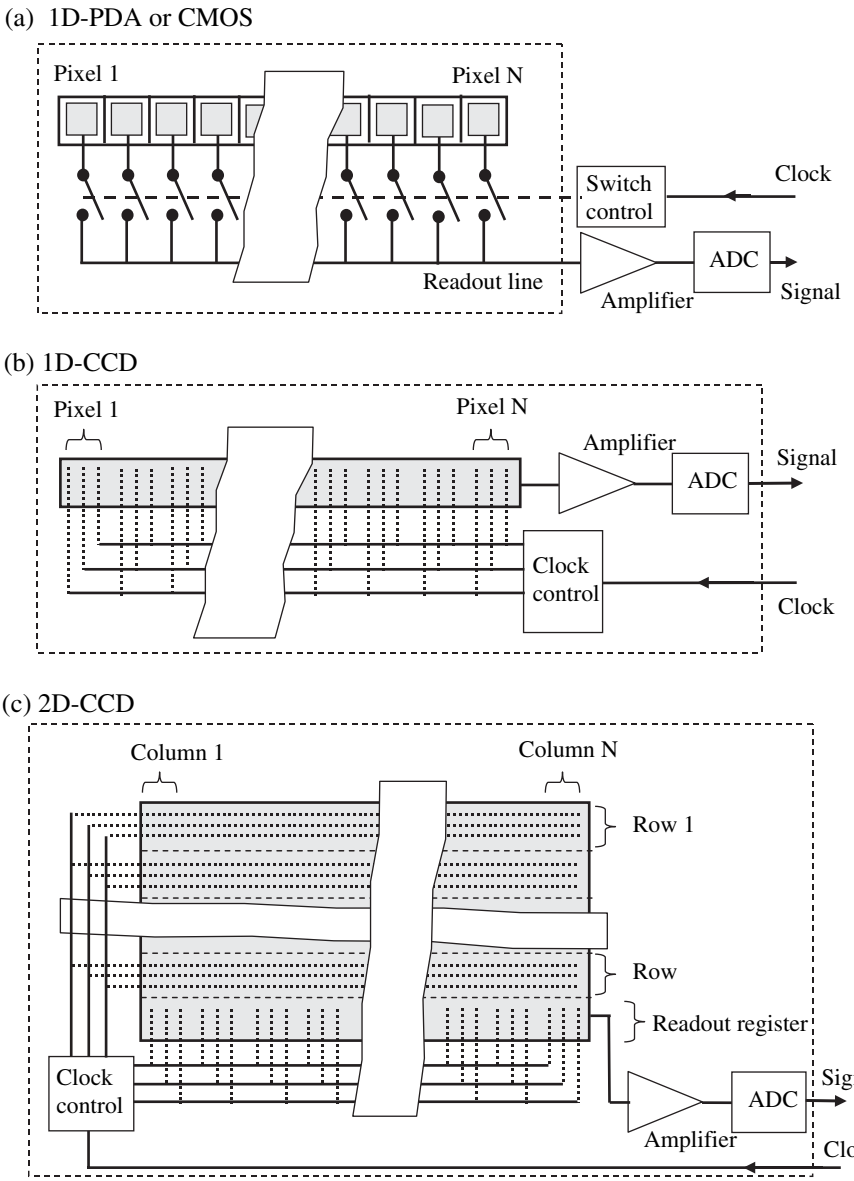

Fig. 7.37. Comparison of linear and two-dimensional solid-state photodetector array design principles. Shown are (**a**) layout of PDA or CMOS, (**b**) One-dimensional CCD, (**c**) Two-dimensional CCD devices

readout to readout. Readout is thus earlier for the first diode than the last, and thus the exposure time interval for the last diode is shifted in time (later) by the readout time. This may be of consequence at relatively short exposure times (compared to the readout time) and varying light levels. On the other hand, linear CCD detectors usually have a readout gate that transfers the charge of all pixels simultaneously into the readout CCD register, which is not exposed to light. Therefore, exposure time for all pixels covers exactly the same interval. In particular, in 2D sensors exposure to radiation during readout can be a problem. These problems can be overcome by using a shutter to darken the detector during readout.

Although there are clear advantages of solid-state array detectors, these devices pose some problems when used to record weak absorption features in DOAS instruments. First, the signal dependence of the dark current of the photodiodes has to be considered (see below). Another problem is the presence of **Fabry–Perot etalon structures** in the recorded spectra, which are caused by the protective overcoat of many commercially available detector arrays and also by possible vapour deposits on the array (Mount et al., 1992; Stutz and Platt, 1992, 1996), see Fig. 7.38 for an example.

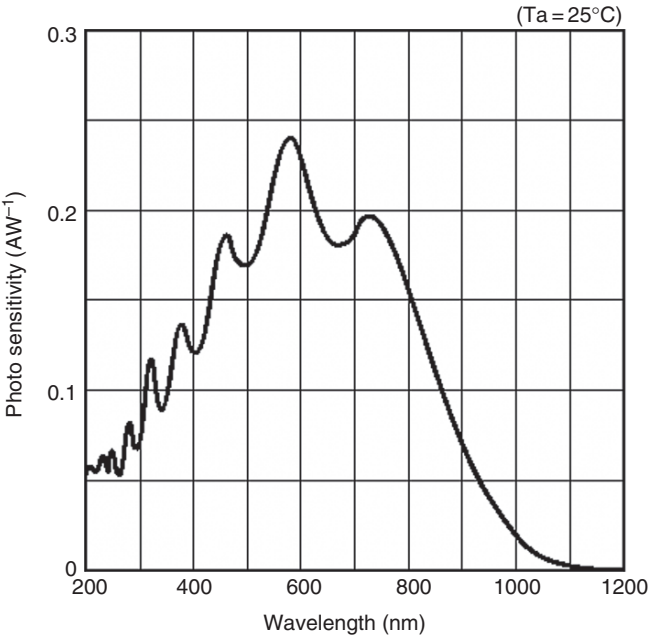

Fig. 7.38. Typical spectral response (in ampere photocurrent per watt of incident radiation) of a PDA detector (Hamamatsu Model S3904-1024). Note strong modulation of response due to the Fabry–Perot etalon effect of the overcoat of the detector chip (from Hamamatsu data sheet NMOS Linear Image Sensors S3900, 3901-1024Q, 3904-2048Q, figure courtesy of Hamamatsu Pholonics)

Particular problems are due to changes in the thickness of the layer of vapour deposit causing continuous changes in the 'etalon' modulation of the array sensitivity. In any case, diode sensitivity (and dark current) varies $>\pm 1\%$ between individual diodes. This usually constant fixed pattern must be compensated for.

Presently, solid-state array detectors have clear advantages, in particular in applications where only low-light levels are available (as in ZSL observation of stratospheric species). For the observation of low optical densities ($D \approx 10^{-3}$–10^{-4}) OSDs appear to give comparable results, however, at inferior light utilisation and thus much longer exposure times. Solid-state array detectors can be described by a number of characteristic features:

Spectral Sensitivity (Quantum Efficiency) – The most popular semiconductor material for solid-state detectors is silicon. Its spectral response extends from <200 nm to about 1100 nm, see Fig. 7.38. The long wavelength (or lower photon energy) end of the range is set by the band gap of silicon, while there is no hard limitation at the short wavelength end. In practice, thin active Si layers are required to obtain good UV sensitivity. While UV-optimised silicon devices (in particular back-illuminated CCDs, see below) can have >20% quantum efficiency below 300 nm, many detectors show little sensitivity below 400 nm. A simple way to obtain UV sensitivity consists of applying an UV-fluorescent coating (such as Metachrome II or Lumogene) on the surface of the device that converts the UV to visible (largely green) light at a wavelength near the maximum of the Si response. Disadvantages of this approach include the relatively low UV quantum efficiency of these coatings (around 10%), their limited lifetime, and the reduction of the sensitivity at longer wavelengths. It should be noted that, in some cases, a glass window with little transmission below ≈370 nm can be the limiting factor in the UV sensitivity.

Memory Effect – Illuminating the PDA with light of high intensity generates a signal which can sometimes also be observed (commonly at much lower intensity) in subsequently recorded spectra, although the detector is completely darkened. This effect is called memory effect. It was e.g. studied by Stutz (1996), but its origin is not quite clear. By waiting a few seconds and/or recording some spectra with the shortest possible integration time, it is usually possible to remove this effect (Alicke, 1997; Geyer, 2000).

Dark Current – As the name indicates, the 'dark current' of an optical detector is the current (or more generally speaking its output signal) which is still present if no radiation (within the detectors spectral sensitivity range) is admitted to the device. The dark current can be minimised by detector design and, for a given detector, by reducing its temperature. The dark current decreases exponentially with temperature, and can always be reduced to negligible levels by cooling the array low temperatures (−40°–80°C). The remaining dark signal can, in principle, be determined by observing the detector signal without illumination and then be subtracted from the signal.

Signal-dependent Dark Current – Naive subtraction of the diode array dark signal determined by recording the signal without illumination leads to wrong results. The origin of this observation can be found by inspection of the (simplified) circuit diagram of an individual diode (Fig. 7.39). It shows that the average voltage across the p-n junction is largest (approximately equal to U_o) if the diode is not illuminated. Under illumination (i.e. during an actual measurement), the voltage across the junction necessarily decreases. This apparent paradox is due to the different average voltages across the diode junctions during exposures, when the array is darkened or irradiated. At an exposure close to saturation, the average voltage during the signal integration period will be about $U_o/2$. In consequence, the 'dark signal' obtained by a measurement with no light admitted to the detector will overestimate the actual dark signal by up to a factor of two (Stutz and Platt, 1992). In fact, the effect can be even larger, since the diode capacitance increases with decreasing voltage. Note that this effect occurs with linear diode arrays (using readout switches), as well as with CCD arrays. A detailed explanation of this effect and procedures for its elimination is given by Stutz and Platt (1992).

Fixed Pattern 'Noise': Another potential problem when using solid-state detectors is the high variability of the sensitivity from diode to diode. The diode sensitivity depends on the wavelength of the incoming light and can vary from 1% up to several percent between the diodes of one array (Stutz, 1996). Usually, however, this sensitivity variation is systematic, (the popular term 'fixed pattern noise' is a misnomer), and can be readily corrected. Since DOAS is intended to observe optical densities down to well below 10^{-3}, it is necessary to accurately remove the diode sensitivity structure from a spectrum.

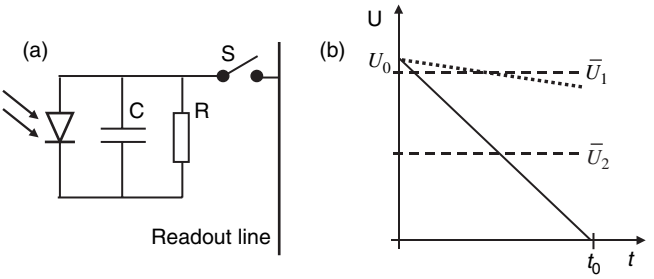

Fig. 7.39. (**a**) Simplified circuit representation of a single pixel in a diode array (or CCD) detector. During readout switch S is closed; (**b**) Temporal evolution of the voltage of a pixel: During acquisition of a dark spectrum the average voltage $\bar{U}_1$ across the capacitance C of the diode is close to the initial voltage U_0, and the dark current $I_{DC} = U/R$ is relatively high. However, in an actual measurement the average voltage $\bar{U}_2$ is always lower (in fact $\bar{U}_2 \approx U_0/2$) if the signal is close to saturation. Therefore, the dark current during a typical measurement will be considerably lower than indicated by a measurement with an un-illuminated detector

An easy way would be the division of each spectrum by a 'white light' lamp reference spectrum scanned just before each spectrum. However, this procedure can lead to additional lamp structures in the spectrum, in particular when Xe high-pressure lamps are used, since Xe emission lines differ in both spectra, due to differences of the illumination of the detector. Note that, in passive DOAS systems, the diode sensitivity structure is usually removed while eliminating the Fraunhofer structure (see Sect. 7.14.3). A common method to eliminate diode sensitivity structures in active long path DOAS spectra is the 'multi-channel scanning technique' (MCST) introduced by Knoll et al. (1990). The basic idea of the MCST is the combination of a multi-channel detection system (e.g. a PDA) with the scanning technique generally used to cover a larger spectral region with a single channel detection system. This technique is described in detail in Sect. 10.5.

7.6.4 PDA Detectors

Figure 7.40 shows the layout and cross-section of a typical silicon PDA detector (S3904-1024 by Hamamatsu) encompassing 1024 diodes, each measuring 0.025 by 2.5 mm, integrated on a single silicon chip. Thus, the total sensitive area measures 25 mm (in dispersion direction) by 2.5 mm. Note that there are two sets of diodes, 'active diodes' and 'dummy diodes'. The latter are read out separately. Taking the difference of 'active' and 'dummy' signals reduces the fixed pattern noise of the device. Data of some popular PDA types are summarised in Table 7.7.

7.6.5 CCD Array Detectors

Another type of solid-state photodetector is the charge coupled device CCD detector. Its name is derived from the readout mechanism. The charge generated by the radiation impinging on the detector is stored in potential wells

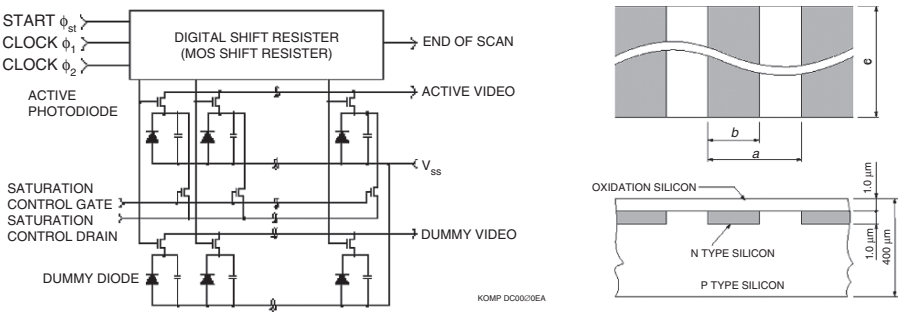

Fig. 7.40. Circuit schematic and layout of a PDA detector (Hamamatsu Model S3904-1024) (from Hamamatsu data sheet NMOS Linear Image Sensors S3900, 3901-1024Q, 3904-2048Q, figure courtesy of Hamamatsu Photonics)

Table 7.7. Characteristics of some linear Photo-Diode Arrays (PDA) for spectroscopic applications

Type (Manufacturer)	Pixel aspect ratio $(h_D \times w_D)$µm	No. of elements N	Sensitive Area mm × mm	Saturation Charge electrons	Max. pixel rate MHz	Dark current pA
S3900-1024, NMOS (Hamamatsu)	2500 × 25	1024	25.6 × 2.5	10^8	2	0.1
S3904-2048, (Hamamatsu)	2500 × 25	2048	51.2 × 2.5	1.6×10^8	2	0.1
S3904-1024Q (Hamamatsu)	5000 × 50	1024	51.2 × 5	6.3×10^8	2	0.4

generated by electrodes on the surface of the semiconductor (silicon). By applying suitable waveforms to the electrodes, the charge can be moved across the semiconductor, usually towards one edge of the device where it is fed to an electrode connected to a readout amplifier. While PDAs are usually one-dimensional (i.e. the individual photodiodes are arranged in a linear row), CCD's are typically two-dimensional. However, one-dimensional devices are also available (e.g. ILX-511 from SONY, see Table 7.8).

Geometry of Linear CCD Detectors: In principle, linear CCDs are in widespread use in the industry, for instance in fax machines, computer scanners, bar code scanners, modern (electronic) copiers, etc. However, in most of these applications two-dimensional originals are scanned, so the CCD line sensor pixels must be (at least approximately) quadratic. Typical pixel dimensions (h_D by w_D) are, therefore, 15 µm by 15 µm or 7 µm by 7 µm (see Table 7.9). For special purposes, some linear CCDs with aspect ratios (h_D by w_D) of about 10 are available (see Table 7.8).

Geometry of Area CCDs: The problem of insufficient pixel height can be overcome by using two-dimensional CCDs and summing up all pixels of a column.

Readout Speed: Readout speed is on the order of 10^6–10^7 pixels per second (1–10 MHz, see Table 7.8). Thus, total readout of a linear CCD takes about 2–0.2 ms. Taking the above requirements for readout speed (about 0.1 ms for a complete readout in active DOAS systems), presently only the fastest systems can match the requirements. Typical devices/systems fall short by about one order of magnitude. Using CCD sensors with *multiple readout taps* (e.g. 8 as in the case of DALSA IT-F6 TDI, see Table 7.8) could provide the required speed, although at the expense of additional electronics (8 ADCs plus associated electronics are required). For two-dimensional CCDs, readout time is an even more severe limitation. For instance, a CCD with 2000 by 100 elements (dispersion direction by vertical) would require 200 ms

Table 7.8. Some CCD sensors for linear spectroscopic applications

Type (Manufacturer)	Pixel aspect ratio ($h_D \times w_D$) µm	No. of elements N	Sensitive area mm × mm	Saturation Charge electrons	Max. pixel rate MHz	Separate readout shift register
ILX 511 (SONY)	200×14	2048	28.67×0.2	1.6×10^5	2	Yes
TCD 1205D (Toshiba)	200×14	2048	28.67×0.2	$\approx 2 \times 10^5$	2	Yes
TCD1304AP (Toshiba)	200×8	3648	29.18×0.2	?	0.6	Yes
IL-C6 (DALSA)	500×13	2048	26.6×0.5	$\approx 2 \times 10^5$	15	Yes
IT-F6 TDI[a] (DALSA)	$13 \times 1248(13 \times 96 \times 13)$	2048	26.6×1.3	4.6×10^5	8×20	Yes
S7030-1007 (Hamamatsu)	24×24	1024×122	24.58×2.93	3×10^5		

[a]UV sensitive to 250 nm.

Table 7.9. Some CMOS sensors for spectroscopic applications

Type (Manufacturer)	Pixel aspect ($h_D \times w_D$) µm	No. of elements N × M	Sensitive area mm × mm	Saturation charge electrons	Dark current electrons/s	Max. pixel rate MHz	Readout noise electrons
Star250[a] (fill factory[b])	25 × 25	512 × 512	12.8 × 12.8		4750	8	74
Star1000[a] (fill factory[b])	15 × 15	1024 × 1024	15.4 × 15.4	120,000	3500	12	39
ACS-1024[a](PVS[c])	13 × 13	1026 × 1026	13.21 × 13.21	300,000	< 3000	30 fps	≈ 100
ELIS-1024[d](PVS[c])	125 × 7.8125 × 64.4	1024 × 128	0.125 × 7.998	800,000–6.4×10^6	12,000	30	1600
LIS-1024[d] (PVS[c])	125 × 7.8	1024 × 1	0.125 × 7.998	8×10^6	?	20	≈ 500
LNL2048R[e] (pixel devices[f])	200 × 7	2048 × 1	0.2 × 14.34	187,500	8000	32	17
S8378-1024Q[d,e] (Hamamatsu)	500 × 25	1024 × 1	25.6 × 0.5	3.9×10^7	2.5×10^5	0.5	≈ 6000

fps = frames per second
[a]On chip 10-bit ADC
[b]Fill factory: http://www.fillfactory.com/index2.htm
[c]Photon vision systems: http://www.photon-vision.com/p-lis.htm
[d]UV sensitive
[e]On chip amplifier(s)
[f]Pixel devices

for a complete readout at 1 MHz. Thus, up to two orders of magnitude are missing. Some help could come from the ability to 'bin' pixels, i.e. combine the charge of several pixels (ideally all) of a column in the analogue readout shift register.

Points to Consider When Using CCDs for DOAS Applications

There is a large and growing variety of CCD detectors available. While in principle linear CCDs are ideally suited for DOAS, a number of crucial parameters have to be evaluated.

1. The pixel width w_D and height h_D of most standard scanner CCDs is appropriate for practically all DOAS applications. For passive DOAS applications higher h_D would be desirable.
2. The UV sensitivity of linear CCDs is frequently not sufficient. Linear CCDs are not available in back illuminated versions. This can partly be circumvented by adding UV fluorescent coating (such as Metachrome II or Lumogene) that converts the UV to visible (largely green) light at a wavelength near the maximum of the Si response. Limitations are due to relatively low quantum efficiency (near 10%) compared to >20% for special UV Si devices or back illuminated (two-dimensional) CCDs.
3. Readout time can be a problem, in particular in active DOAS systems. The fastest linear CCD systems or multiple tap CCDs appear to be just fast enough for active DOAS applications. Two-dimensional CCDs are frequently too slow by about two orders of magnitude for active DOAS applications.
4. The charge transfer efficiency has to be considered. While stated efficiencies >99.999% may sound impressive it has to be kept in mind that the charge generated in e.g. the first pixel is shifted through about 1000 pixels. This may lead to a charge loss of the order of 1%. This charge is distributed across other pixels, thus adding to the cross-talk.

Comparison of the Different Solid-state Detectors: As outlined above, PDA and CCD detectors have their strengths and weaknesses. All allow the detection of light signals at the limit of photoelectron shot noise, if conditions are carefully chosen. The margins for shot noise limited detection are much wider for CCD detectors, provided the ADC resolution is sufficient. Some characteristics are compared in Fig. 7.41. For instance, if there are fewer than about 3000 photoelectrons recorded in a CCD detector with 12-bit ADC, the S/N ratio will be determined by the ADC and no longer by photoelectron statistics (intersection of fat, solid line with dashed line b).

7.6.6 CMOS Detectors

Complementary metal–oxide–semiconductor (CMOS) arrays are a relatively new addition to the family of spectroscopic detectors. Little is currently known

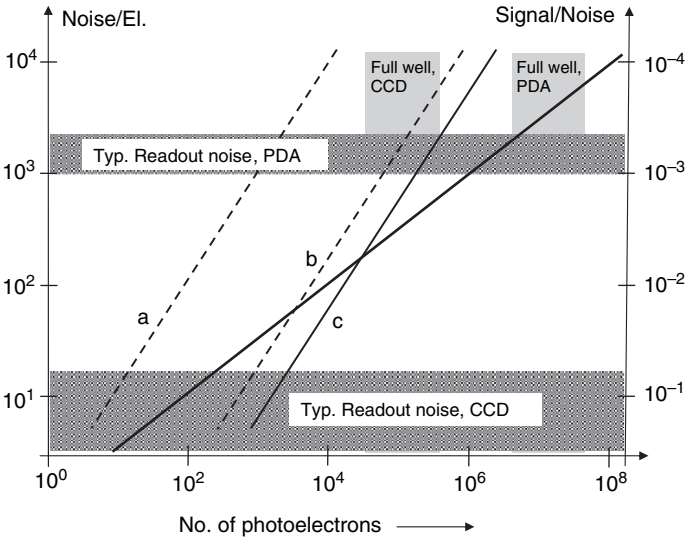

Fig. 7.41. Sketch of signal-to-noise (S/N) ratios as a function of the number of photoelectrons and characteristics of typical CCD and PDA detectors. Fat line: S/N ratio from photoelectron statistics alone; Lines a–c: contribution of the ADC to the S/N ratio of the detector system. (a) 16-bit ADC for a typical CCD detector (6×10^4 photoelectrons full well); (b) 12-bit ADC for a typical CCD detector; (c) 16-bit ADC for a typical PDA (6×10^7 photoelectrons full well)

about their performance in DOAS applications. However, the fact that the detector elements can be integrated on the chip with other electronic components, such as amplifiers and ADC converters, makes them an interesting option. Table 7.9 gives details of currently available CMOS sensors.

7.7 Telescope Designs

In DOAS systems, telescopes are used for two purposes: to collect light from (natural or artificial) light sources and, in active DOAS applications, to transmit a collimated beam of radiation from the light source through the open atmosphere. Basically, the telescopes designs either employ refracting elements, i.e. lenses (refractors) or reflecting elements, i.e. mirrors (reflectors). For DOAS applications, reflectors are often chosen due to absence of chromatic aberrations. Reflectors also need fewer large optical surfaces, which are expensive to manufacture. Traditionally, there are several design choices for reflecting telescopes, which are known as Newtonian, Cassegrain, or Gregor arrangements, as shown in Fig. 7.42. A popular design is the Newtonian, which combines compact and simple optics with easy adjustment. Also, Newtonian telescopes usually form the basis of transmitting–receiving

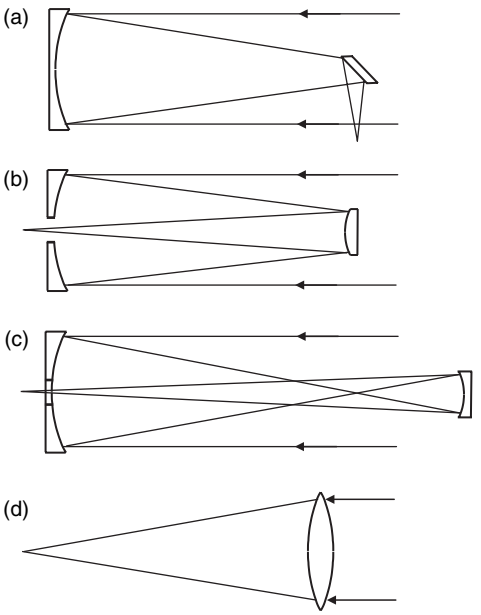

Fig. 7.42. Different telescope designs in use for DOAS applications. Reflectors: (**a**) Newtonian, (**b**) Cassegrain, (**c**) Gregor type telescope, (**d**) Refractor

telescope combination (see Fig. 7.49, Sect. 7.9.3). In contrast, Cassegrain-type telescopes are much more compact, but difficult to manufacture and require strict tolerances in adjustment.

7.8 Optical Multi-pass Systems

In principle, an attractive alternative light path arrangement is to fold the absorption light path in a multiple pass (or multiple reflection) cell (MRC), where the probing beam of radiation traverses the same volume (the 'base path') many times. There are several optical arrangements that allow the multiple folding of light beams. The most widely used are:

- White Cells (White, 1942, 1976)
- Herriot Cells (Herriot et al., 1964; Herriot and Schulte, 1965)
- Passive resonators (Engeln et al., 1998; Ball et al., 2004)

For each design, a number of variants were developed (Horn and Pimentel, 1971; Schulz-DuBois, 1973; Chernin and Barskaya, 1991; Ritz et al., 1992; MacManus et al., 1995; Vitushkin and Vitushkin, 1998; Grassi et al., 2001).

Multi-reflection systems have two main advantages. First, the measurement volume is greatly reduced, thus making the assumption of a homogeneous trace gas distribution much more likely to be fulfilled. Second, the

length of the light path can be changed (typically in certain increments of small multiples of the base path, depending on the particular design of the cell). Therefore, it is possible to keep the length of the light path close to its optimum (see Sect. 7.13) for the respective atmospheric conditions.

Disadvantages of multi-reflection cells include the relatively complicated optical design, the requirement for extreme mechanical stability and small reflection losses. Typically, high reflectivity ($R > 0.99$–0.9999) of the cell mirrors over spectral intervals of several 10 nm is required, but difficult to obtain and to maintain in the field (e.g. due to dust settling on the surfaces), in particular for large area mirrors and in the UV. In some applications, the high-radiation intensity inside the folded light path can cause photochemical reactions that may change the concentration of the species to be measured. In addition, the level of stray light originating from the light source is difficult to measure in multi-reflection cells. Another problem can be due to the reaction of the trace gases with the surfaces of optical or mechanical parts of the cell, although 'open path' cells can reduce this effect.

7.8.1 White Multi-reflection Cells

The basic White multi-reflection system (Fig. 7.43; White, 1942) consists of three spherical, concave mirrors of identical radius of curvature (and thus focal length). The distance between the mirror sets is twice the focal length. The front mirror A faces the two side by side back mirrors B and C. Radiation from the light source is focused in point F_0 such that it illuminates back mirror B, which images point F_0 into F_1 on mirror A. Mirror A is oriented such that the radiation originating from F_1 illuminates back mirror C, which in turn images F_1 into F_2. This completes a round trip of the radiation traversing the system four times. F_2 can be thought of acting as a new entrance to the system, with the next round trip producing foci F_3 and F_4. Since F_2 is closer to the axis of the system, F_3 and F_4 will be as well. Ultimately, there will be

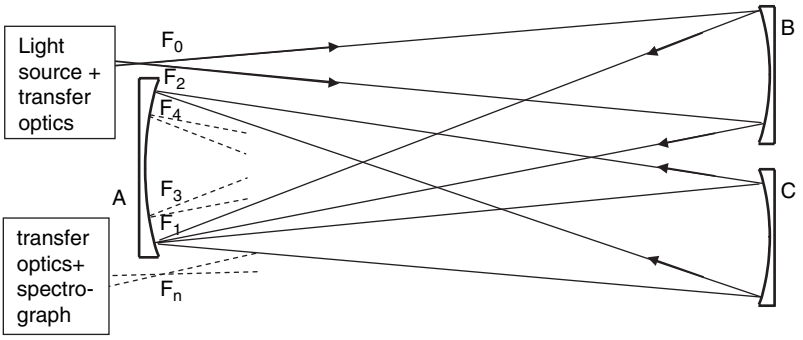

Fig. 7.43. Schematic diagram of a basic White system (adapted from J.U. White, 1942)

two sets of foci F_0, F_2, F_4, ... and F_1, F_3, ... across the surface of 'nesting mirror' A. Usually, mirrors B and C will be tilted slightly such that even and odd numbered reflections of mirror C form two separate rows on mirror A. Finally, one of the images F_N (not shown) falls off the surface of mirror A, thus, leaving the system. Therefore, the number of passes can be adjusted in steps of 4.

In the more advanced White system (White, 1976) in addition to the basic optics, two or three quartz prisms are set up near the front mirror, as shown in Fig. 7.44. In its basic function, the system functions as the 'basic' White system (White, 1942) described earlier. However, the radiation leaving the mirror system after N traverses near the bottom of mirror A is reflected back by prism P1. After making another N traverses, it is returned again by prism P2, giving rise to another $2N$ traverses. Finally, prism P3 reverses the entire set of light paths for a total of $8N$ traverses. Thus, the number of passes can be adjusted in steps of 32 traverses. This scheme not only multiplies the number of passes by 8, but more importantly also considerably increases the stability against mis-alignment of the system. This is due to the fact that each prism acts as retro-reflector, returning the radiation (nearly) exactly back to its original direction in one plane. However, the planes of P1 and P2 are perpendicular to each other, thus compensating misalignments within the system only as long as they do not become too large.

In fact two prisms would be enough to accomplish this effect, as originally described by White (1976). The vertex angle of the prisms is actually slightly smaller than 90° (Ritz et al., 1992). Further optimisations of the design were suggested by Hausmann et al. (1997) and Grassi et al. (2002).

The transmission of radiation through a multi-reflection system is given by the transmission of the transfer optics, the reflectivity R of the mirrors, and the extinction of the air inside the system. The transfer optics consists of

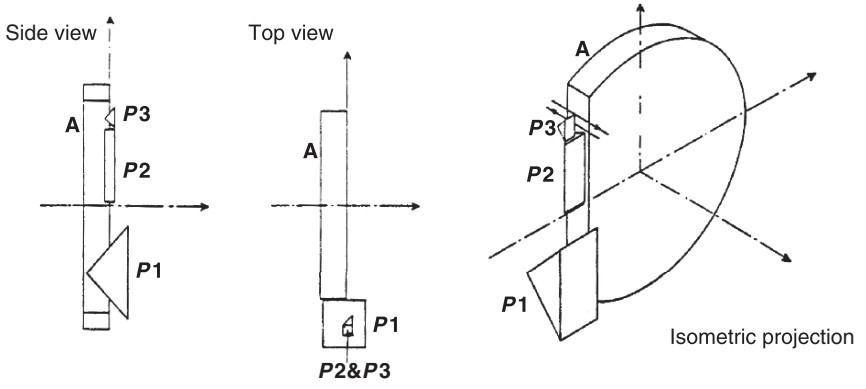

Fig. 7.44. Schematic diagram showing the nesting mirror (**A**) and the prisms P1, P2 and P3 (from Ritz et al., 1992)

two parts. First, optics matching the aperture of the light source to that of the entrance of the multi-reflection cell, and second, optics matching the exit aperture of the multi-reflection cell to the entrance of the DOAS spectrometer. Typically, the desired aperture from a Xe-arc lamp might correspond to an f-number of $\mathrm{F}_1 \approx 1$, while a White cell might have $\mathrm{F}_2 = 100$ (i.e. $2f$ divided by the diameter of the mirrors B and C). Transfer optics would then image the Xe-arc at a magnification of $\mathrm{F}_2/\mathrm{F}_1 \approx 100$. At the exit side (assuming the exit $f/\#$ of the white cell to be the same as the entrance $f/\#$), matching the white cell to the entrance of a spectrometer with $\mathrm{F}_3 = 5$ would require a reduction in image size by $\mathrm{F}_3/\mathrm{F}_2 \approx 20$. Given a diameter $d \approx 0.2\,\mathrm{mm}$ of the brightest spot in the arc (see Sect. 7.3.1), the images on nesting mirror A of the White cell (Fig. 7.43) would be 20 mm in diameter; thus, in order to accommodate many reflection mirrors, A has to be quite large. Alternatively, the aperture of the light source (F_1) could be reduced or that of the White cell (F_2) increased.

Overall, the (broadband) transmission of a White multi-reflection cell is given by:

$$T = \frac{I}{I_0} = G \cdot \mathrm{R}_\mathrm{M}^N \cdot e^{-\varepsilon_\mathrm{B}}, \tag{7.36}$$

where G denotes the transmission of the transfer optics, R_M the mirror reflectivity, N the number of reflections, and ε_B the broadband extinction of the air (see Chap. 6).

7.8.2 Herriott Multi-reflection Cells

The optical design of a Herriott-type multi-reflection cell (e.g. Herriott et al., 1964; Herriott and Schulte, 1965; McManus and Kebabian, 1990; McManus et al., 1995; Zimmermann, 2003) is shown in Fig. 7.45. A collimated beam of radiation enters through a hole in (circular) mirror A at a certain distance R_0 from the centre of the mirror. The radiation is then reflected N times between mirrors A and B and leaves through the same hole. The reflections are located

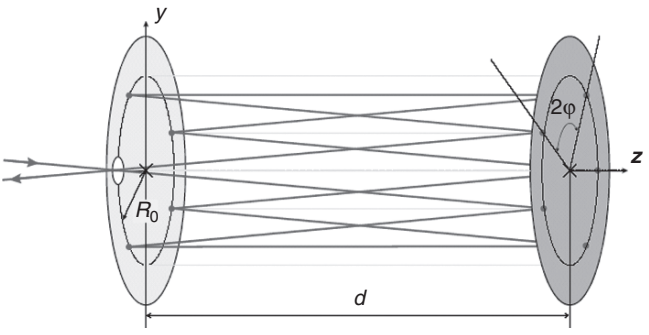

Fig. 7.45. Schematic diagram of a Herriott cell (from Zimmermann, 2003)

on either mirror on circles (or more general on ellipses) with radius R_0. The vertex angle θ in a triangle formed by the centre of mirror A and the locations of two consecutive reflections is given by $\theta = 2\pi M/N$, where M denotes the number of times the reflections circle around the optical axis of the system. The angle θ is determined by the ratio of the distance d between the mirrors and their radius of curvature R:

$$\cos\Theta = 1 - \frac{d}{R}. \tag{7.37}$$

The total absorption path L is given by $L = d \cdot N$. Advantages of Herriott cells are their simple optical setup combined with a good stability of the beam profile due to the re-focussing properties of the optics. In addition, there is some immunity against tilt of the mirrors against each other and lateral translation of the mirrors. A major disadvantage is due to the need for collimated beams. More details on the theory of Herriott cells can be found in Herriott and Schulte (1965), and some details for applications in Zimmermann (2003) and McManus and Kebabian (1990).

7.8.3 Passive Resonators (CEAS, CRDS)

Passive resonators can also provide long optical paths (e.g. Engeln et al., 1998; Brown, 2003; Ball et al., 2004; Fiedler, 2005). This technique has become known as cavity enhanced absorption spectroscopy (CEAS). The basic idea is to introduce white light (intensity I_L) into an optical resonator (see Fig. 7.46) consisting of two mirrors with reflectivity R. Initially, averaged over a wavelength interval larger than the free spectral range, only the fraction $\rho = 1 - R$ will enter the resonator. However, once in the resonator the radiation will be reflected $1/(1 - R)$ times (neglecting other losses) on average. Finally, half the radiation will leave the resonator through mirror 1, the other half through mirror 2, with each fraction having the intensity:

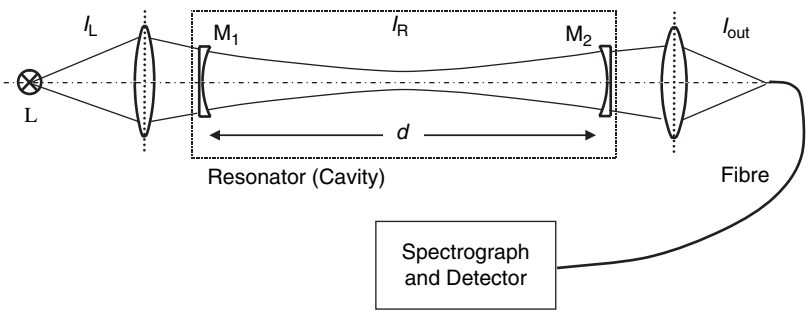

Fig. 7.46. Sketch of a cavity-enhanced absorption-based DOAS system (Ball et al., 2004; Fiedler, 2005). The resonator would be set up in the open atmosphere

$$\mathrm{I_{out}} = \mathrm{I_L} \times \frac{(1-R)}{2} = \mathrm{I_L} \cdot \frac{\rho}{2}. \tag{7.38}$$

If additional (broadband) extinction ε_B is present, the average length of the absorption path will be:

$$\bar{L} = \frac{d}{\rho + \varepsilon_\mathrm{B} d}, \tag{7.39}$$

where ε_B denotes all broadband extinctions (due to Rayleigh and Mie scattering, and broadband trace gas absorption). Presently, mirrors with $R > 0.9999$ over a spectral range of several 10 nm can be manufactured, leading to $\rho = 1 - R < 10^{-4}$, and consequently average light paths $\bar{L} > 10^4 \cdot d$ if extinction is neglected. At a base path $d = 1\,\mathrm{m}$ this would correspond to $\bar{L} > 10\,\mathrm{km}$. The transmitted light would be $\mathrm{I_{out}} \approx 5 \times 10^{-5} \cdot \mathrm{I_L}$. While this looks small, it is comparable to losses in 'long path' DOAS system using light beams in the open atmosphere, see Sect. 7.11.

Practical problems with CEAS include the need to determine the actual light path, accumulation of dust on the mirrors, and the fact that highest transmission occurs outside the range of high mirror reflectivity.

As can be seen from (7.39), the light path depends not only on the mirror reflectivity, but also on the (broadband) atmospheric extinction, and it can thus vary widely as atmospheric conditions change. Moreover, the reflectivity is likely to change, e.g. due to dust deposition on the mirrors. Typically the length of the light path has to be determined by recording absorption lines of species with known concentration such as O_2, O_4, or water vapour (if the humidity is simultaneously measured), or by cavity ring down spectroscopy (CRDS) (Brown, 2003).

7.9 Active DOAS Systems

Active DOAS systems employ their own light source; therefore, they have to include suitable optics to transmit light through the atmosphere to the spectrometer. The most basic arrangement of a light path in the open atmosphere (see Fig. 7.47) consists of a light source (search light type) defining one end of the light path and a receiving telescope coupled to a spectrometer defining the other. Earlier DOAS instruments (e.g. Perner and Platt, 1979; Platt et al., 1979) were based on this arrangement and they are still in use (in particular in commercial instruments). However, in recent years a series of variants was developed which have clear advantages over the original active DOAS setup.

7.9.1 'Classic' Active Long-path System

The original design of active DOAS systems (see Fig. 7.47) consisted of a receiving telescope (coupled to a dispersing device, e.g. a spectrometer and a telescope) 'looking' into the light beam emitted from a light source, e.g. a

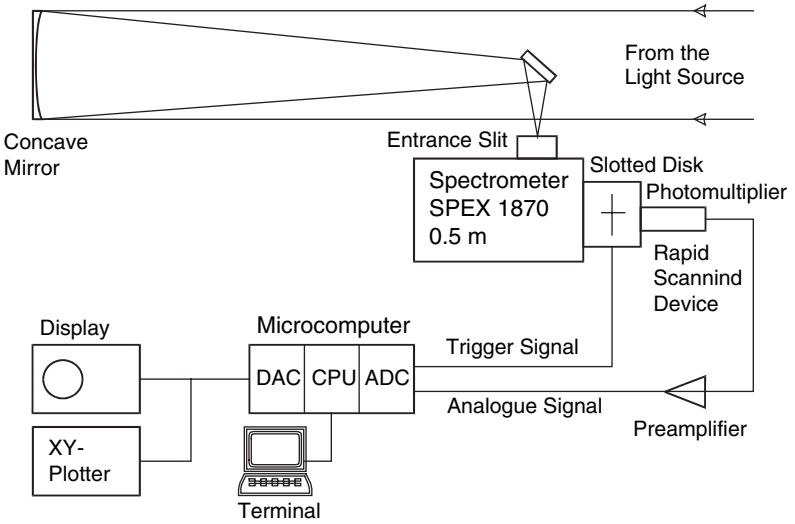

Fig. 7.47. Schematic setup of a 'classic' DOAS system using separate transmitting and receiving telescopes and an optomechanical (rotating 'slotted disk' + photomultiplier) scanning system

search light. This type of setup has been used in many investigations since the 1980s (Perner and Platt, 1980; Platt et al., 1979, 1981; Harris et al., 1982). The instrument averages trace gas absorptions over the extended volume of air. Disadvantages of this arrangement include the requirement to align the optical elements at either end of the light path, and the necessity of power at two location, which frequently complicates the logistic requirements in field campaigns.

In active long-path DOAS systems, a receiving telescope of sufficiently large aperture, usually 150–300 mm, is required to collect the light. The telescope has to be precisely pointed at the light source or retro-reflector array (see Sect. 7.4.9). This can usually only be accomplished by active control of the telescope. Note that even a very rigid mounting of the optical building blocks of the system will usually not solve the problem. Due to an 'El Mirage' effect, the light path will 'bend' due to changing thermal gradients in the atmosphere.

The aperture ratio of the telescope must match that of the spectrometer (or of the connecting Quartz fibre), see Table 7.10.

7.9.2 High-resolution DOAS Spectrometers

Some species, in particular atoms and certain small molecules, exhibit narrow absorption lines (see Table 7.10), which dictate the use of a light source with high spectral intensity. A prominent case is the OH radical, which was

Table 7.10. Data pertinent to high resolution and low resolution DOAS systems for the spectroscopic detection of OH radicals and NO_3 radicals

Radical parameter	OH	NO_3
Wavelength of strongest band or line l/nm	308	662
Line width Γ/nm	0.0017	3.2
Effective abs. cross section σ/cm^2	1.3×10^{-16}	1.8×10^{-17}
Minimum detectable optical density D_0	10^{-4}	10^{-4}
Detection limit C_0 molecules/cm^3 ($L = 5\,\mathrm{km}$)	1.5×10^6	1.1×10^7
Interfering molecules	SO_2, CH_2O, CS_2, $C_{10}H_8$	H_2O

reliably detected in the atmosphere for the first time by DOAS (Perner et al., 1976). The required high-spectral energy density can, at present, only be supplied by a laser. Its emission bandwidths can either be broad or narrow compared to the OH lines. The former approach has a fixed laser emission wavelength, but requires combination with a high-resolution spectrometer (Perner et al., 1976, 1987; Hübler et al., 1984; Platt et al., 1987, 1988; Dorn et al., 1988; Hofzumahaus et al., 1991; Mount, 1992). The latter variety of the technique uses a narrowband laser scanning the OH line (Zellner and Hägele, 1985; Amerding et al., 1990, 1992).

As an example, an experiment following the broadband approach is shown in Fig. 7.48. A frequency-doubled dye laser coupled to a beam-expanding telescope serves as a light source. To keep interference at negligible levels, the beam is expanded to about 0.2 m diameter (Perner et al., 1976). The laser emission bandwidth (FWHM) of about 0.15 nm is large compared to the width of the OH line ($\approx$0.0017 nm). The received light is dispersed by a 0.85-m double spectrometer with a resolution comparable to the OH line width (Perner et al., 1987a; Hofzumahaus et al., 1991). Table 7.10 lists some key parameters of a long-path OH spectrometer in comparison to a 'classical' low-resolution DOAS instrument. An important consideration is the amount of self-produced OH, since the intense UV radiation of the laser beam photolyses ozone, yielding O^1D atoms that can react with H_2O to produce OH in the beam.

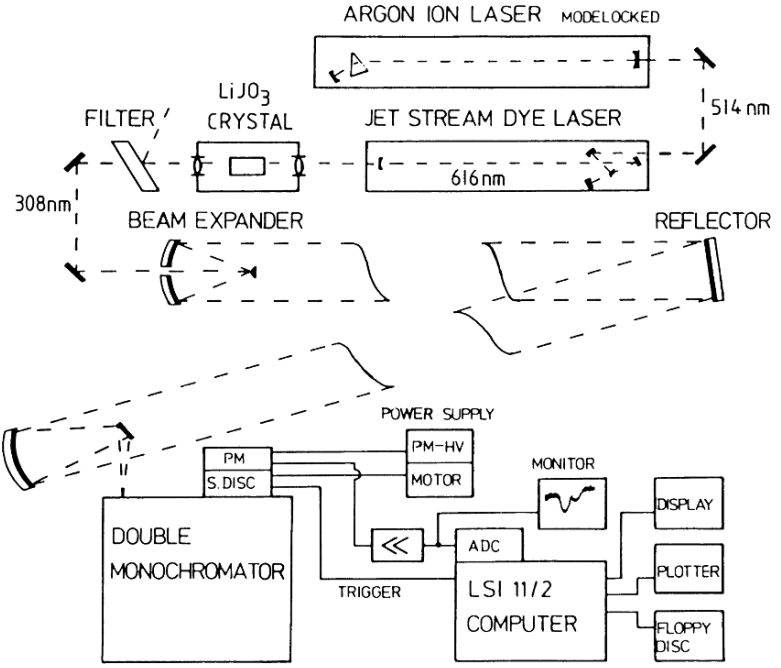

Fig. 7.48. Optical setup of a high-resolution long-path spectrometer. A laser system supplies the high-spectral intensity required due to the high resolution of 0.002 nm (instead of about 0.5 nm for a low-resolution DOAS) (adapted from Platt et al., 1987)

Later designs of this instrument coupled the high-resolution spectrometer to a multi-reflection cell (see Sect. 7.8) to allow more localised measurements and better control of the optical path (Brauers et al., 1996; Dorn et al., 1993, 1996, 1998; Hausmann et al., 1997; Hofzumahaus et al., 1991, 1998; Brandenburger et al., 1998).

7.9.3 Recent Designs of Active Long-path DOAS System

A variation of the basic active DOAS design uses a reflector (usually a corner cube retro-reflector as indicated in Fig. 7.49) to return the light of a source located next to the spectrometer. Thus the total light path length is twice the distance between light source/spectrometer and reflector. Usually, a coaxial merge of transmitting and receiving telescope as shown in Fig. 7.49 is used. This setup was first described by Axelsson et al. (1990). Advantages and limitations are similar to the classic arrangement described in Sect. 7.9.1. However, power and delicate alignment is only necessary at the spectrometer/light source site (Plane and Nien, 1992; Edner et al., 1993; Hausmann

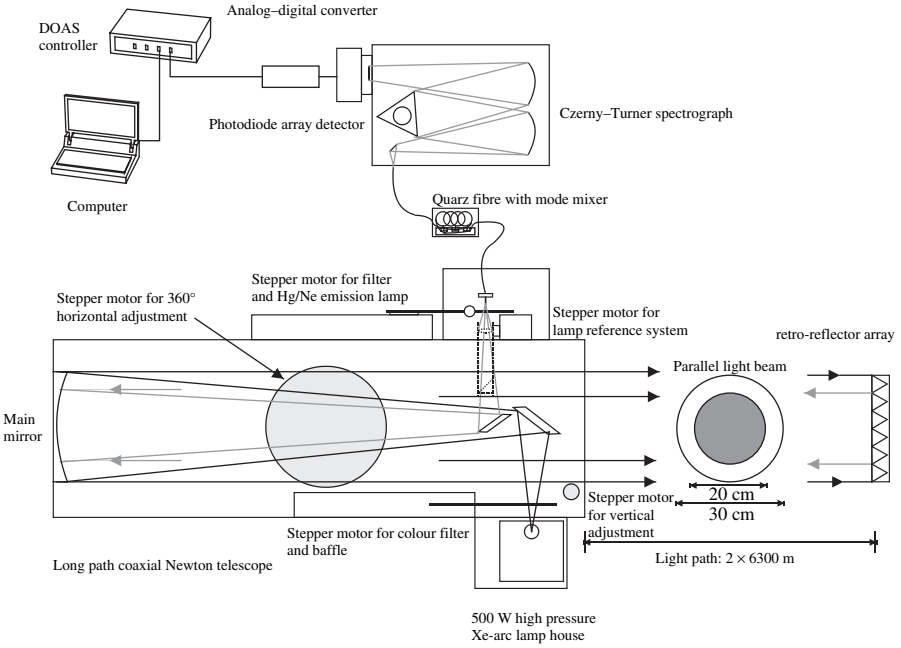

Fig. 7.49. Schematic setup of a DOAS system using a coaxial arrangement of transmitting and receiving telescope in conjunction with a retro-reflector array (Geyer et al., 2001). This type of setup, pioneered by Axelsson et al.(1990), has become the standard for active DOAS systems for research in the recent years (from Geyer et al., 2001)

and Platt, 1994; Heintz et al., 1996; Alicke et al., 2002; Geyer et al., 1999; Allan et al. 1999, 2000). The introduction of retro-reflectors also has the advantage of reducing the effect of atmospheric turbulence on the light beam (see Sect. 7.4.9). This is due to the capability of corner cube retro-reflectors to return the incident light exactly (although with some lateral offset) into the direction of incidence. In addition, the light collected by the receiving section of the telescope is transmitted to the spectrometer via quartz fibre, allowing the introduction of a 'mode mixer' (see Sect. 7.4.7; Stutz and Platt, 1997a), which further reduces the effect of atmospheric turbulence. Because of these advantages, the arrangement shown in Fig. 7.49 has become the standard setup for active long-path DOAS instruments.

Variations of this design use two telescopes for transmitting and receiving the light mounted side by side at close distance. Thus, only a small fraction of the transmitted light is actually collected by the receiving telescope. This drawback can be partially overcome by covering half of the aperture of each retro-reflector element by a wedged window with a very small (fraction of a degree) angle (Martinez et al., 1999). In this way, the light returned by the

retro-reflectors is deflected from its initial direction by a small angle. Thus, two beams are reflected, one at either side of the incident beam on the retro-reflector. The receiving telescope is mounted at the position of one of the beams.

7.9.4 DOAS Systems with Optical Multi-pass Systems

The absorption light path may be folded in a multiple reflection cell. The optical arrangements are described in Sect. 7.8. Figure 7.50 shows a typical setup of a DOAS system using a White type open multiple reflection cell. Main elements are the light source, and entrance transfer optics to match the large aperture of the light source to the small aperture of the White multiple reflection system. After traversing the multiple reflection system, secondary transfer optics match the aperture to that of the fibre and spectrometer. Spectrometer, mode-mixer, and detector are of the same design as in the long-path system described in Sect. 7.9.3.

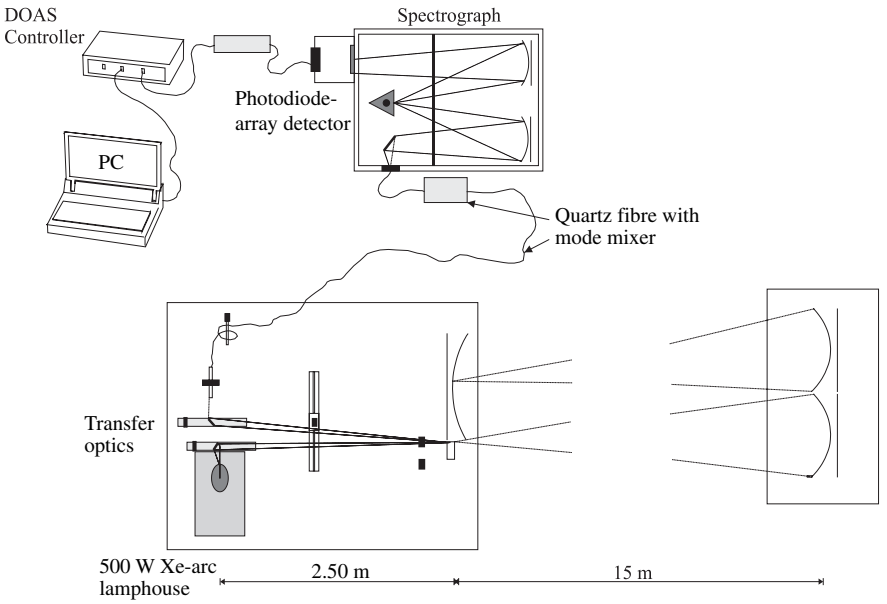

Fig. 7.50. Schematic optical setup of the 'White' multi-pass system with a base path of 15 m, as used during a field campaign in Pabstthum/Germany

7.10 Passive DOAS Systems

Passive DOAS systems measure atmospheric trace gases by using extraterrestrial light sources, e.g. sunlight or moonlight. As described in detail in Chaps. 9 and 11, radiation from these sources traverses the entire atmosphere, and thus the measured 'apparent column density' (ACD) or SCD always contains contributions from all layers of the atmosphere. However, suitable choices of the observation geometry can enhance the contributions of certain layers compared to others. In this way, stratospheric trace gases can be measured, as well as trace gases close to the ground. In fact, to some extent atmospheric trace gas profiles can be derived from passive measurements made with instruments located at the ground. Since a relatively large aperture angle of the telescope can be tolerated (on the order of 0.1–1° instead of 10^{-3}–10^{-2}°), short focal length are sufficient. Consequently, much smaller telescopes (aperture 25–50 mm) compared to typical active instruments are usually sufficient. Depending on the wavelength and sensitivity requirements, a wide variety of detector designs is used, ranging from non-dispersive semiconductor or photomultiplier detectors, to spectrograph – photodiode array combinations. A number of spectrometer designs are in use, as outlined in Sect. 7.5.

7.10.1 Direct Sun/Moon Setup

Measurements of direct sun or moon light provide information on the trace gas concentration integrated along the light path. The instruments typically consist of a spectrometer-detector combination coupled to a telescope. An optical and mechanical setup is needed to follow the apparent movement of these celestial bodies in the sky. These solar trackers can be quite complex, depending on their pointing accuracy. Care must be taken to reduce the solar light intensity in order to avoid damaging the instrument.

7.10.2 Zenith Scattered Light DOAS

A spectrograph directed to the zenith (Fig. 7.51) observes the optical density of trace gas absorption bands indirectly via the scattering process of the sunlight in different layers of the atmosphere (assuming that the instrument located is north or south of the respective tropic so that it never receives direct sunlight).

DOAS of scattered rather than direct sunlight has been applied by many authors to the determination of vertical column densities (VCDs) of O_3, NO_2 (e.g. Brewer et al., 1973; Noxon, 1975; Pommereau, 1982; Mount et al., 1986; Pommereau and Goutail, 1987; Wahner et al., 1990; Johnston et al., 1992), NO_3 (Sanders et al., 1987; Solomon et al., 1989), OClO (Solomon et al., 1987b; Schiller et al., 1990; Perner et al., 1991; Kreher et al., 1996; Otten et al., 1998),

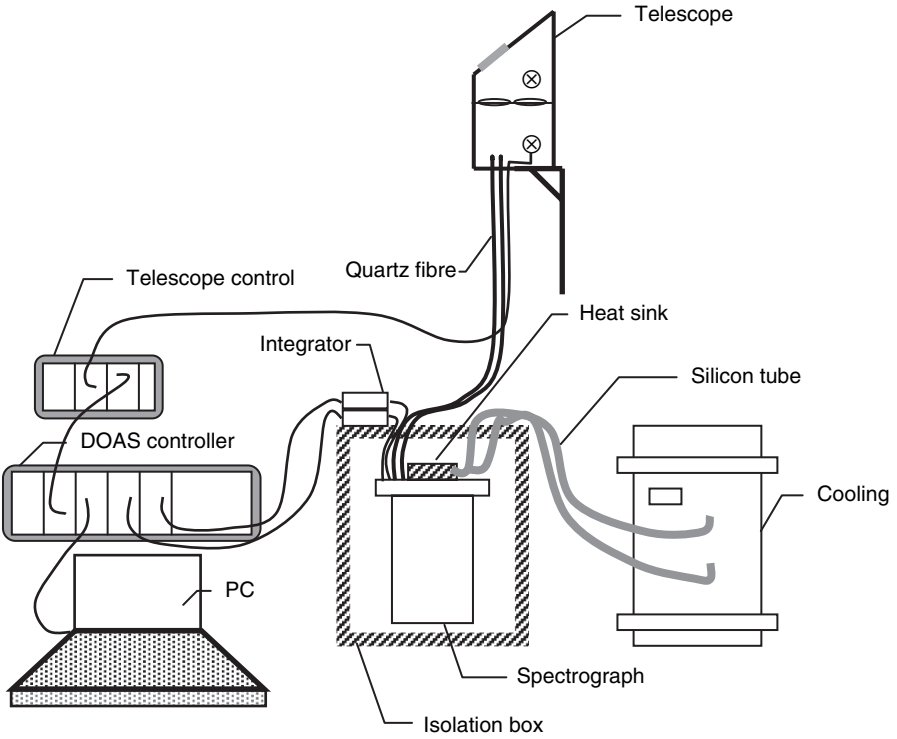

Fig. 7.51. Schematic setup of a ZSL-DOAS system (from Hönninger, 2002)

BrO (Solomon et al., 1989b; Kreher et al., 1997), and $(O_2)_2$ (e.g. Sarkissian et al., 1991; Erle et al., 1995). Examples can be found in Chap. 11.

There are three major advantages of this technique:

1. No adjustment of the telescope direction is required.
2. Stratospheric species can be detected by ground-based instrumentation, even in the presence of (tropospheric) cloud cover.
3. Tropospheric species can be measured, even if they are distributed over the entire troposphere (see off-axis measurements, Sect. 7.10.3).

These advantages come at the expense of relatively difficult calculations of the effective light path length. In addition, several effects of light scattering in the atmosphere have to be carefully compensated for, as outlined in Chap. 9.

Figure 7.51 shows the schematic setup of a ZSL-DOAS system. In this example, two telescopes, each coupled to its own spectrometer, were used to cover different wavelength ranges. Quartz fibres conduct the light from the telescopes to the spectrometers. The quartz fibres also remove the polarisation sensitivity of the instrument.

7.10.3 Off-axis, MAX-DOAS Instruments

A recently developed variant of the ZSL-DOAS technique is off-axis spectroscopy. In off-axis spectroscopy, the instrument is pointed away from the zenith by an 'off axis' angle α. There are several azimuth configurations possible. Frequently an observation direction away from the sun is chosen (e.g. Hönninger et al., 2004a). Advantages of this arrangement are better sensitivity at very large SZAs ($>95°$) and better sensitivity to trace gases close to the instrument. At an instrument location at the ground, this means better sensitivity to trace species in the boundary layer and lower troposphere. However, as detailed in Chap. 9, the radiation transport calculations for off-axis viewing geometries are more complex than in the case of ZSL-DOAS.

When making a series of off-axis observations at different observation angles $\alpha_1 \ldots \alpha_n$, the growth of the observed trace gas slant column as a function of increasing α gives information about the vertical distribution of the trace gas in the vicinity of the instrument (see Chap. 9). This approach became known as MAX-DOAS (e.g. Heismann, 1996; Hönninger, 2002; Hönninger and Platt, 2002; Leser et al., 2003; Wagner et al., 2004; Heckel et al., 2005) and has since been used in a large and growing number of applications. Some examples are given in Chap. 11.

MAX-DOAS systems are employed for the measurement of atmospheric trace gases by several authors using different technical approaches. Sequential observation at different elevation angles is shown in Fig. 7.52. This approach has the advantage of a relatively simple setup, requiring only one spectrometer and a mechanism for pointing the telescope (or the entire spectrometer–telescope assembly) in different directions. It has therefore been in several studies (Sanders et al., 1993; Arpag et al., 1994; Miller et al., 1997; Kaiser, 1997; Hönninger and Platt, 2002; Leser et al., 2003; Bobrowski et al., 2003; Löwe et al., 2002; Heckel et al., 2005; Bobrowski, 2005). One disadvantage is that the measurements are not simultaneous. Typically, a complete cycle encompassing several observation directions may take several minutes (e.g. Hönninger and Platt, 2002). This can be a problem during periods of rapidly varying radiation transport conditions in the atmosphere, e.g. varying cloud cover, aerosol load, or during sunrise/sunset. In addition, the instrument contains mechanically moving parts, which may be a disadvantage in adverse environments and during long-term operation at remote sites.

The simultaneous observation at different elevation angles solves this problem. However, one disadvantage is the increased instrumental requirement, since a spectrometer and a telescope for each of the observation directions is needed. However, recent development of very compact, low-cost spectrometer/detector combinations, as used in the "Mini-MAX-DOAS" instrument, shown in Fig. 7.53, can be of help here. Alternatively, some simplification may come from using 'two-dimensional' spectrometry, where a single spectrometer is equipped with a two-dimensional (CCD) detector, where one dimension is

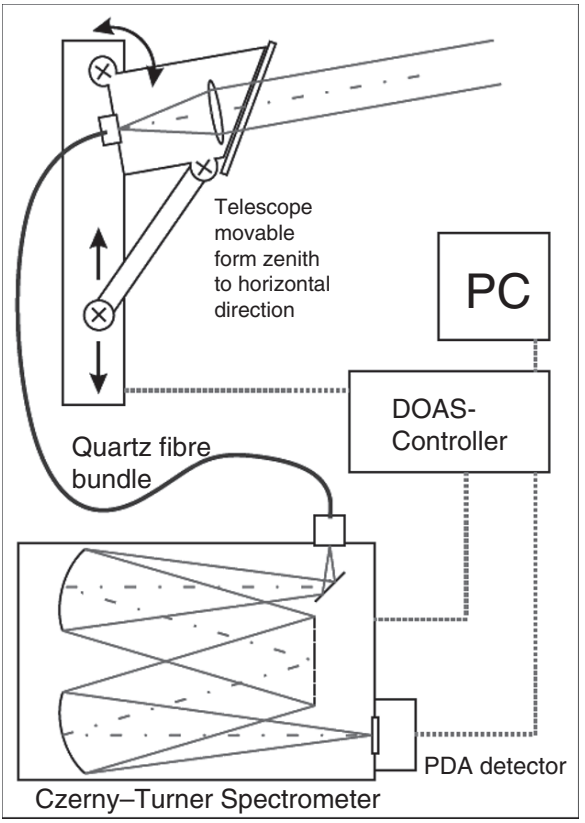

Fig. 7.52. Schematic setup of a MAX-DOAS system. A small telescope coupled to a spectrometer can be pointed to any elevation between horizon and zenith (from Hönninger, 2002)

used for dispersion, and the other for spatial resolution, i.e. different viewing angles, as outlined in Fig. 7.31 (Heismann, 1996; Wagner et al., 2002b; Wang et al., 2003, 2005; Heue et al., 2005).

A more severe problem lies in the fact that the different instruments have to be ratioed against each other in order to eliminate the solar Fraunhofer structure (see Chap. 9). This proves extremely difficult if different instruments with different instrument functions are involved (e.g. Bossmeyer 2002). Although the situation can be somewhat improved by 'cross convolution' (i.e. convoluting each measured spectrum with the instrumental line shape of the respective spectrum it is to be compared with), it appears that, with present instrumentation, the highest sensitivity is reached with sequential observation.

A solution lies in the combination of techniques (1) and (2), i.e. the use of multiple spectrometers (one per observation direction) and moving telescopes (or spectrometer–telescope assemblies). While this approach appears

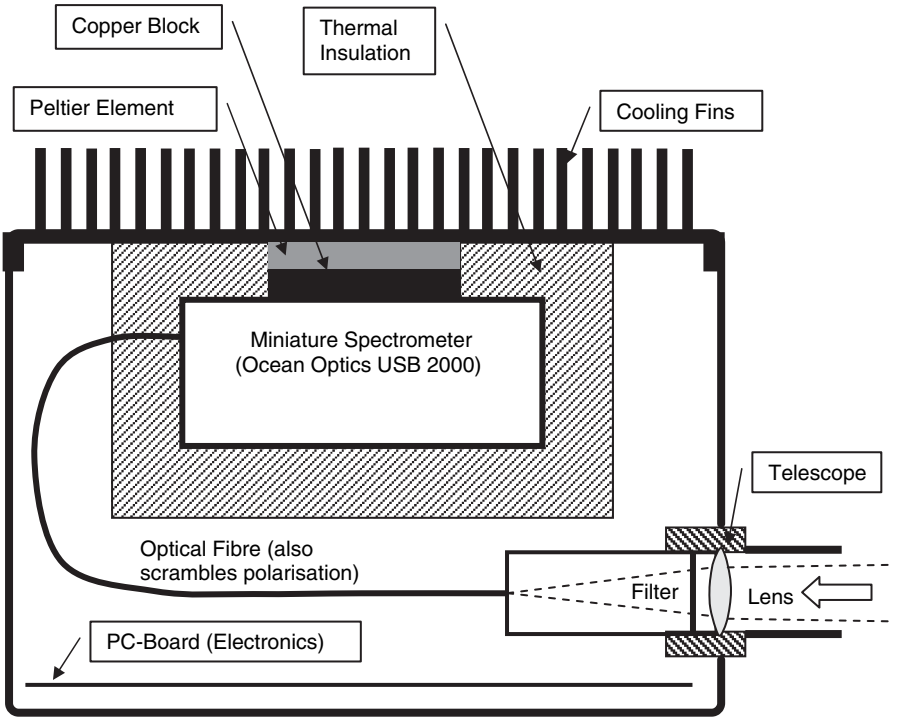

Fig. 7.53. Schematic cross-section through a miniature MAX-DOAS system (Bobrowski, 2005). The entire instrument, including the telescope, can be pointed to any elevation between horizon and zenith

to combine the disadvantages of the two above setups, it also combines their advantages. If each individual instrument sequentially observes, at all elevation angles, and the observation are phased in such a way that at any given time one instrument observes each observation direction, then not only simultaneous observation at each angle is achieved, but also each instrument regularly observes the zenith to record a Fraunhofer spectrum for reference. Instruments based on this approach have been used on the German research vessel Polarstern (see Leser et al., 2003; Bossmeyer, 2002).

7.10.4 Imaging DOAS (I-DOAS) Instruments

Imaging spectroscopy is characterised by acquiring an absorption spectrum on each spatial pixel in a two-dimensional array. The additional, spectral 'dimension' contains information about wavelength-dependent radiation intensities. Thus, the measurement results in a three-dimensional data product with two spatial dimensions and one wavelength dimension, which could be called a 'super colour' or 'hyperspectral' image, in contrast to ordinary colour images containing intensity information of only three wavelength ranges.

There are two commonly used techniques to obtain this information, distinguished by the temporal sequence of acquiring data of the three dimensions. 'Whiskbroom' imaging sensors acquire the spectrum of one spatial pixel at a time. Hence, each of the two spatial dimensions needs to be scanned consecutively. Extending non-imaging sensors with a mechanical (two axis) scanning mechanism leads to this type of instrument. While preserving the major advantage of relatively simple design of the diffractive optics and photon detector elements, the disadvantage of the whiskbroom scanning principle is a linear dependence of total measurement time on the total number of spatial pixels, i.e. the time increases proportional to the square of the desired (linear) image resolution. 'Pushbroom' sensors simultaneously image one spatial direction (vertical in Fig. 7.54) and spectrally disperse this light in order to obtain a spectrum of each pixel of the investigated object. Doing this simultaneously requires a two-dimensional detector. Since scanning is needed only in the one spatial direction (horizontal in Fig. 7.54), the total measurement time is greatly reduced (Lohberger et al., 2004).

Sunlight, which is scattered by atmospheric molecules and particles in the viewing direction of the instrument, serves as the light source. Radiative transfer is characterised by typically small distances between the instrument and the object of investigation, compared to scattering lengths by atmospheric Rayleigh and Mie scattering. Typical extinctions due to Rayleigh and Mie scattering (at e.g. 400 nm) are $4.6 \times 10^{-7}\,\mathrm{cm}^{-1}$ and $4 \times 10^{-7}\,\mathrm{cm}^{-1}$, which result in scattering lengths of 22 km and 25 km, respectively (see Sect. 4.2) In contrast, the typical range of gas plumes being visualised is a few hundred

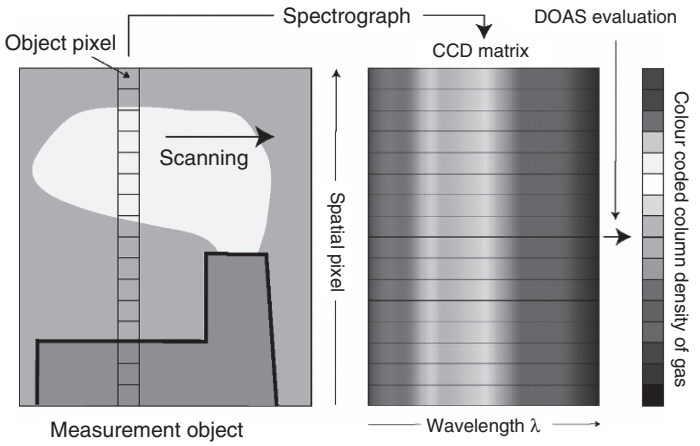

Fig. 7.54. Measurement principle of an I-DOAS instrument. The instrument utilises pushbroom imaging to simultaneously acquire spectra of one spatial direction (i.e. vertical). Spectral information along the second spatial dimension (horizontal) is obtained by scanning the scene using a scanning mirror. The spectra are evaluated using the DOAS technique (from Lohberger et al., 2004)

metres. In many applications, the contribution of photons that are scattered into the instrument without passing the gas cloud are therefore negligible.

7.10.5 Aircraft-based Experiments

DOAS instruments have been used on aircrafts in many applications, primarily using ZSL geometries (Wahner et al., 1989a,b, 1990a,b; Schiller et al., 1990; Pfeilsticker and Platt, 1994; Pfeilsticker et al., 1997a). Advantages of this platform are mobility, and the ability to make measurements at many places in a short period of time and over inaccessible places. In addition, the viewing geometry from an elevated platform provides some altitude information (see Chap. 11). The recently developed variants of the ZSL-DOAS technique, the off-axis and MAX-DOAS techniques are also being used for aircraft measurements (e.g. Wang et al., 2003, 2005; Heue et al., 2004a,b).

As outlined in Fig. 7.55, there are usually a large number of viewing directions. Simultaneous measurements are of great advantage here since, on a rapidly moving platform, the time for an individual measurement is very short if a reasonable spatial resolution is desired. In a recent implementation

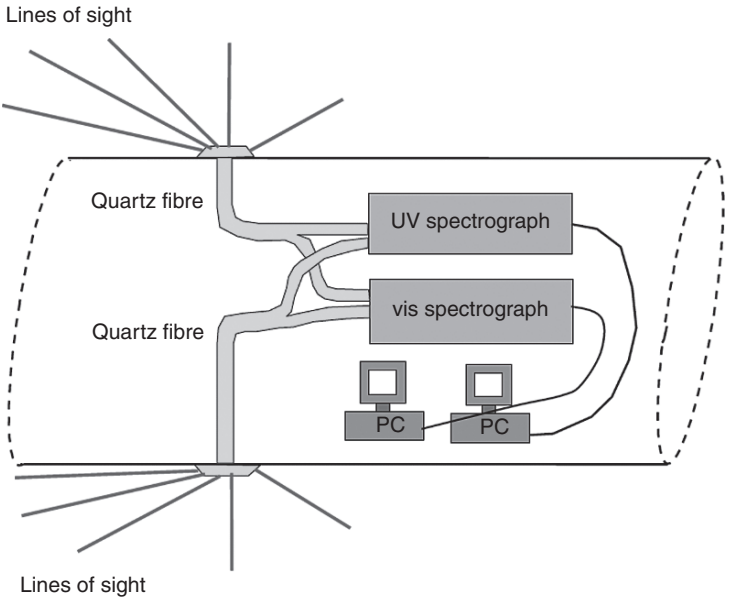

Fig. 7.55. Schematic setup of an airborne MAX-DOAS system (AMAX-DOAS). The scattered sunlight is observed using a set of small telescopes mounted at the upper and lower side of the aircraft body, respectively, and pointing to several elevation angles between zenith and nadir. The light is transmitted via quartz fibre bundles to two spectrographs, where it is analysed. The spectra are then saved on a PC (from Heue et al., 2005)

of the principle (Heue et al., 2005; Bruns et al., 2004), two groups of telescopes were mounted at the top and bottom of the aircraft body. Besides nadir- and zenith-looking telescopes, several telescopes collecting radiation at small angles (e.g. $\pm 2^\circ$) above and below the aircraft were installed. The latter telescopes gave good resolution at atmospheric layers above and below the aircraft, see Chap. 11.

While it is possible to employ a separate spectrometer for each viewing direction, an approach using an imaging spectrometer, as described in Sects. 7.5.2 and 7.10.3, can be of advantage. The fibres from the different telescopes would then be mounted along the entrance slit, as shown in Fig. 7.31. Design goals of aircraft instruments are low weight, resistance to vibration, and unattended operation. Particular problems for aircraft instruments include provisions for continued operation during short-time power interruptions and compensation of the effect of ambient pressure change.

7.10.6 Balloon-borne Instruments

An interesting application of this technique is the determination of vertical trace gas concentration profiles by taking a succession of spectra from a balloon-borne spectrometer. From these spectra, trace gas vertical profiles can be derived in two ways:

1. From a series of spectra recorded at different altitudes during ascent, a series of the column densities $S(z)$ above the balloon altitude z can be derived. After conversion to vertical column densities and differentiation of the concentration profile, $c(z)$ can be derived (e.g. Pommereau and Piquard, 1994a; Pundt et al., 1996; Camy-Peyret et al., 1995, 1999; Ferlemann et al., 1998; Fitzenberger et al., 2000; Bösch, 2002; Bösch et al., 2003).
2. From a balloon floating at high altitude, a series of spectra is taken during sunset (or sunrise). From the derived trace gas column densities $S(\vartheta)$, as a function of SZA and ϑ, the concentration profile $c(z)$ can be derived by an 'onion peeling' approach (Weidner et al., 2005; Dorf et al., 2005).

The required hardware is shown in Figs. 7.56 and 7.57. Figure 7.56 illustrates the mechanical setup of a balloon-borne direct-sunlight DOAS system, which is housed together with an FT-IR instrument on a three-axis stabilised balloon gondola (Camy-Peyret et al., 1995). A moveable mirror directs the sunlight into the spectrometers. Figure 7.57 depicts a cross-section of the pressurised dual spectrometer module.

7.10.7 Satellite Instruments

Given the successful application of differential absorption techniques on the ground and on board aircrafts, satellite-based systems appeared attractive.

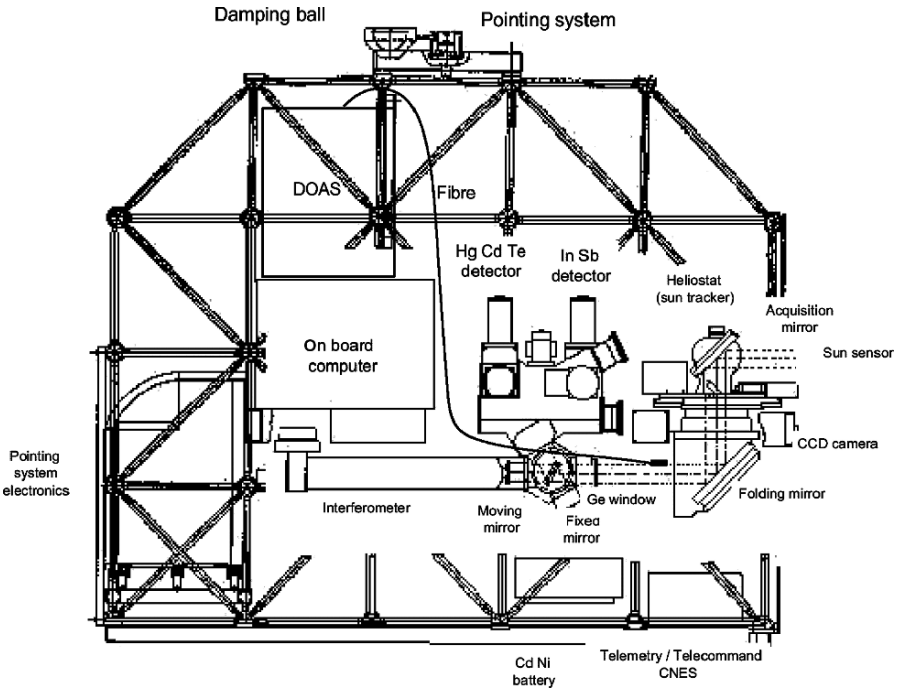

Fig. 7.56. Setup of a balloon-borne direct-sunlight DOAS system. The DOAS instrument is housed together with an FT-IR instrument on a three-axis stabilised balloon gondola (from Camy-Peyret et al., 1995)

Earlier instruments such as the Solar Backscatter UV (SBUV) (Dave and Mateer, 1967) measured the ozone column density by taking the ratios of a few wavelength pairs, essentially bringing the concept of the Dobson spectrometer (Dobson and Harrison, 1926; Dobson, 1968) to space. However, with the launch of the Global Ozone Monitoring Experiment (GOME) on the ESA satellite ERS-2 (GOME Users Manual, 1995) in 1995, DOAS principles have been applied to satellite instruments with great success. Since GOME, several further DOAS-type instruments, in particular the SCanning Imaging Absorption spectroMeter for Atmospheric CHartographY (SCIAMACHY) (e.g. Burrows et al., 1991; Noël et al., 1999) on the ESA ENVIronmental SATellite (ENVISAT), OSIRIS on ODIN (Murtagh et al., 2002), the ozone monitoring instrument (OMI) on the NASA Earth Observing Satellite Aura (EOS-Aura), and others (see Table 7.11) have been launched. Three viewing geometries are utilised for DOAS measurements (see Chap. 11):

1. Nadir view: Looking down from space towards the nadir direction, the sunlight reflected from the earth's surface or atmosphere (called the 'earthshine' in analogy to 'moonshine') can be utilised to obtain information

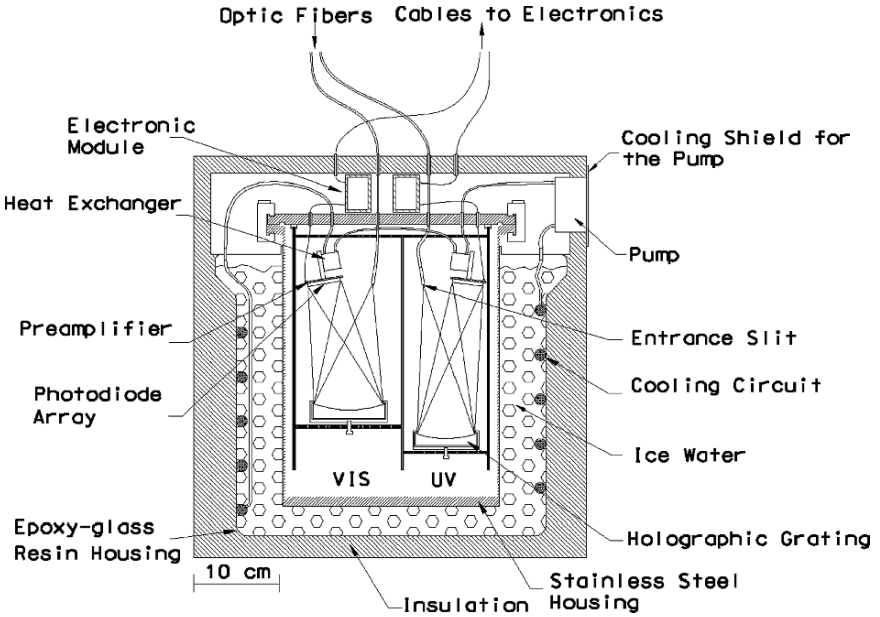

Fig. 7.57. Spectrometer of a balloon-borne direct-sunlight DOAS system (Bösch, 2002). Two spectrometers (one for the visible (VIS) and the other for the ultraviolet (UV) spectral range) receive direct sunlight through a heliostat (see Fig. 7.56) and quartz fibres. The spectrometers are sealed in a stainless steel housing and thermostated to 0°C by a ice-water package inside a Styrofoam insulated housing (from Bösch, 2002)

on atmospheric trace gas column densities. Examples of satellite instruments using this geometry include GOME, ILAS, SCIAMACHY, ODIN, and OMI, as shown in Table 7.11.

2. Limb view: In this geometry, light scattered from the earth's terminator is analysed. By observing the limb at different tangent altitudes, vertical trace gas concentration profiles can be inferred.
3. Occultation: By observing the light of the rising or setting sun, moon, or stars through the atmosphere, vertical trace gas concentration profiles can be deduced.

In addition, there are several types of orbits which are particularly suited for probing the atmospheric composition from satellite:

1. Low earth orbit (LEO), where the satellite circles earth at an altitude around 800 km. Particularly advantageous are sun-synchronous polar orbits, from where the satellite instrument can observe the whole earth each day or within a few days. In the latter case, the time for one orbit can be adjusted such that the instrument will see a specific point on earth at

Table 7.11. DOAS-type satellite instruments and some characteristics

Instrument/platform	Launch - operation until	No. of spectrometers	Spectral ranges nm	No. of pixles	Spectra resolution nm	Viewing geometries
Global ozone monitoring experiment (GOME)/ ERS-2	1995–today	4	237–316	1024	0.22	Nadir
			311–405	1024	0.24	
			405–611	1024	0.29	
			595–793	1024	0.33	
OSIRIS/ODIN	20 February 2001–today	1	280–800	1353×286	1.0	Limb
ILAS-I/ADEOS	1 November 1996–30 June 1997	1	753–784	1024	0.1	Solar Occultation
SCIAMACHY/ENVISAT	2002–today	8	240–314	1024	0.24	Nadir, Limb, Solar Occultation, Lunar Occulation
			309–405	1024	0.26	
			394–620	1024	0.44	
			604–805	1024	0.48	
			785–1050	1024	0.54	
			1000–1750	1024[a]	1.48	
			1940–2040	1024[a]	0.22	

(continued)

Table 7.11. continued

Instrument/platform	Launch - operation until	No. of spectrometers	Spectral ranges nm	No. of pixles	Spectra resolution nm	Viewing geometries
			2265–2380	1024[a]	0.26	
Ozone Monitoring Instrument (OMI)/EOS-AURA	15 July 2004–today	1	350–500	780 × 576	0.45–1.0	Nadir
GOME-II/METOP	2006	4	240–315	1024	0.24–0.29	Nadir
			311–403	1024	0.26–0.28	
			401–600	1024	0.44–0.53	
			590–790	1024	0.44–0.53	

[a]InGaAs detectors

essentially the same local time (e.g. 10:30 in the morning in the case of ERS-2)
2. Geostationary orbits where the satellite circles earth in synchronicity with the rotation of earth at an altitude of 36000 km.

An example of the LEO is GOME on board the second European Research Satellite (ERS-2). A schematic outline of the instrument is shown in Fig. 7.58. It consists of a scanning mirror, a set of four spectrometers, and thermal and electronic sub-systems (Burrows et al., 1991, 1999). Light backscattered from earth is collected by the scan mirror, then focused on the entrance slit of the spectrometer by an off-axis parabolic telescope. After being collimated, the light passes through a pre-dispersing prism, which produces an intermediate spectrum within the instrument. The pre-dispersing prism is arranged in such a way that internal reflection results in a polarised beam which is directed towards three broadband detectors monitoring the polarisation state of the light (the polarisation monitoring device, PMD). The PMD observes radiation from the atmosphere in the wavelength ranges 300–400 nm, 400–600 nm, and 600–800 nm. The main beam from the pre-dispersing prism is then directed towards the four individual spectrometer gratings of GOME. Each

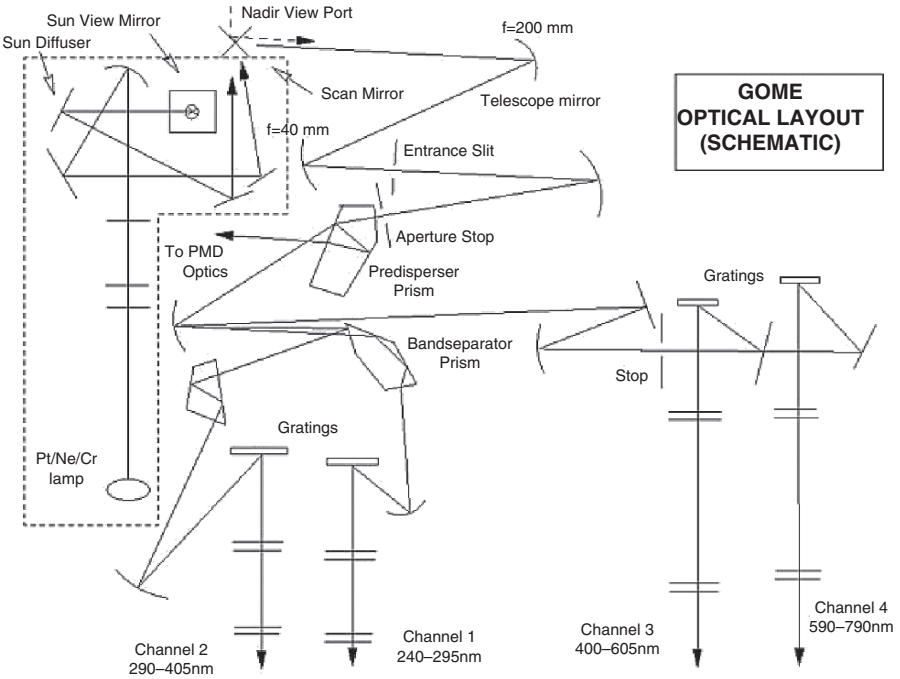

Fig. 7.58. Schematic setup of a satellite DOAS system: GOME on ERS-2 (from Burrows et al., 1999)

spectrometer uses refractive optics and a 1024-element diode array detector. Thus the entire spectral range between 232 and 793 nm can be observed at a spectral resolution of about 0.2 nm and 0.33 nm, below and above 400 nm, respectively.

The GOME instrument is optimised for the collection of the upwelling radiation from earth (nadir view) directly by the scan mirror. The direct, extraterrestrial solar irradiance (the Fraunhofer reference spectrum, FRS) is measured by GOME over a diffuser plate to reduce its intensity prior to being reflected by the scan mirror into the instrument. The spectra and other signals recorded by GOME are transmitted to the ESA ground station at Kiruna. These data are processed for ESA by the GOME data processor at the DLR-PAC (German Atmospheric and Space Research Processing and Archiving Centre). The resulting 'level 1' products, essentially calibrated radiances, and level 2 total ozone column data product are subsequently distributed to the scientific community. ERS-2 was launched on 20 April 1995 into a nearly polar, sun synchronous orbit, having an equator crossing time of 10:30 am in a descending node. The scan strategy of GOME yields complete global coverage at the equator in 3 days. The swath width of GOME is 960 km, divided into three pixels of $320 \times 40\,\mathrm{km}^2$ for the array detector ($20 \times 40\,\mathrm{km}^2$ for the PMDs, which are read out 16 times faster than the arrays; Burrows et al., 1999, and references therein).

Besides ozone, GOME can measure a wide variety of atmospheric trace gases, including bromine monoxide (BrO) (e.g. Hegels et al., 1998; Richter et al., 1998; Wagner and Platt, 1998), chlorine dioxide (OClO) (Burrows et al., 1998; Burrows et al., 1999; Wagner et al., 2001), formaldehyde (HCHO) (Burrows et al., 1999; Chance et al., 2000) sulphur dioxide (SO_2) (Eisinger and Burrows, 1998, and references therein), nitrogen dioxide (NO_2) (Burrows et al., 1998; Leue et al., 2001), and water vapour (H_2O) (Noël et al., 1999; Maurellis et al., 2000b). In addition, ozone and aerosol profiles may also be retrieved (e.g. Hoogen et al., 1999, and references therein).

7.11 Light Utilisation in a Long-path Spectrometer

The spectral noise, and thus detection limit and accuracy of DOAS instruments, usually depends on the amount of light reaching the detector (see Sect. 7.6). Thus, it is important to maximise the fraction of light provided by the light source that reaches the detector. This section describes light throughput of a typical long-path spectrometer. For simplicity, we take the dimension of a single-path DOAS system, as sketched in Fig. 7.59. The results are also valid for folded-path systems (see Sect. 7.9.3).

The fraction x_1 of light emitted from the radiating surface of the light source, e.g. from the filament of an incandescent lamp or arc of a Xe high-pressure lamp (see Sect. 7.3.1), transformed into a light beam, can be approximated as follows:

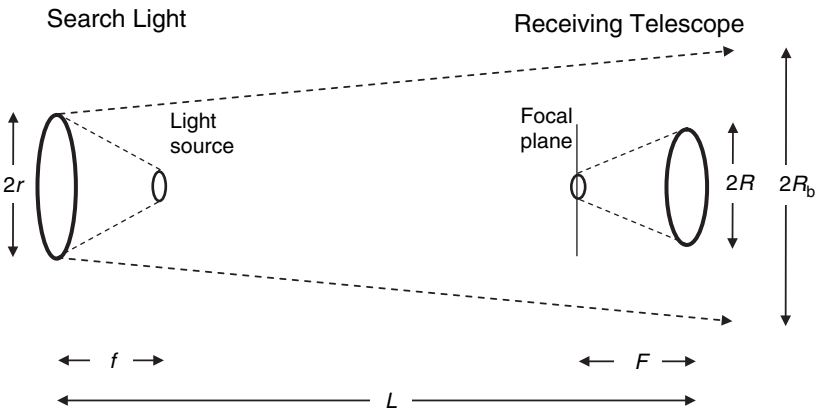

Fig. 7.59. Optical sketch of a single-path active DOAS system. The search light mirror of the transmitting system has radius r and focal length f, the corresponding quantities for the mirror of the receiving telescope are R and F

$$x_1 \approx \frac{r^2\pi}{4\pi f^2} = \frac{1}{4} \cdot \left(\frac{r}{f}\right)^2, \tag{7.40}$$

where r denotes the radius of the light-source (search light) mirror and f its focal length (see Fig. 7.59). Assuming the radiating surface of the lamp to be circular with the radius r_l (and thus the surface $r_\mathrm{l}^2\pi$), the divergence of the beam (half angle) is given by:

$$\alpha \approx \frac{r_l}{f}, \tag{7.41}$$

and the radius R_b of the light beam at the receiving telescope located at the distance L from the search light (assuming $R_\mathrm{b} >> r$ and setting $\alpha \simeq \tan\alpha$):

$$R_b \approx \alpha \cdot \ L = \frac{r_l \cdot L}{f}. \tag{7.42}$$

We obtain the fraction x_2 of the emitted light beam actually collected by the telescope:

$$x_2 = \left(\frac{R}{R_b}\right)^2 = \left(\frac{R \cdot f}{r_l \cdot L}\right)^2. \tag{7.43}$$

Combining (7.43) with (7.40) gives the fraction x_e of the total lamp output received by the telescope:

$$x_e = x_1 \cdot x_2 = \frac{1}{4} \cdot \left(\frac{R \cdot r}{r_l \cdot L}\right)^2. \tag{7.44}$$

Note that for a given radius r, x_e is independent of the focal length f of the search light mirror and thus its aperture. On the other hand, x_e is proportional to the product of the areas of the two mirrors and inversely proportional to the radiating area of the lamp, and thus its luminous intensity (radiated energy

per unit of arc area). The important quantity is the illumination intensity D_b in the focal plane of the receiving telescope (i.e. the brightness of the focal spot). It is given by:

$$D_b = \frac{P_\mathrm{l} \cdot x_e}{(r \cdot F/L)^2 \pi}, \tag{7.45}$$

where P_l denotes the lamp output power and $(r\,F/L)^2\pi = R_\mathrm{f}^2\pi$ the area of the focal spot (see below). Substituting x_e from (7.44) yields:

$$D_b = \frac{P_\mathrm{l}}{4\pi} \cdot \left(\frac{R}{r_\mathrm{l} \cdot F}\right)^2. \tag{7.46}$$

The illumination intensity of the focal spot neither depends on the length of the light path L (if light extinction in the atmosphere is neglected) nor on the properties of the search light optics. Of course the size of the focal spot (i.e. its radius R_f) will be proportional to the size (r) of the search light mirror, and inversely proportional to the light path length:

$$R_\mathrm{f} = \frac{r \cdot F}{L}. \tag{7.47}$$

From (7.46), it appears as if the light throughput of the system could be maximised by choosing the largest possible aperture $A_\mathrm{r} = 2R/F$ of the receiving telescope. However, the aperture A_r, must not be larger than the aperture A_s of the spectrometer (if $A_\mathrm{r} > A_\mathrm{s}$, a portion of the light received by the telescope will simply not be used). Thus, for a given value of A_s, the brightness of the focal spot has a maximum value given by substituting $R = A_\mathrm{s}F/2$ into (7.46):

$$D_\mathrm{b} = \frac{P_\mathrm{l}}{16\pi} \cdot (A_\mathrm{s}/r_\mathrm{l})^2. \tag{7.48}$$

The result is, that for a long-path spectrometer the size of the optical system does not matter, provided the aperture of the receiving system matches that of the spectrometer and the dimensions of the optical components exceed certain 'minimum sizes' given by (7.47).

Depending on the relative sizes of the focus R_f and the entrance slit ($w \cdot h$), three regimes can be distinguished (see Fig. 7.60):

1. w, $h < R_\mathrm{f}$: The amount of light entering the spectrometer will be independent of L (except for extinction). This is due to the independence of the illumination intensity from L stated in (7.46).
2. $w < R_\mathrm{f} < h$: The amount of light entering the spectrometer will vary nearly in proportion to L^{-1}.
3. $R_\mathrm{f} < w$, h: The amount of light entering the spectrometer will vary proportional to L^{-2}

Thus, it can be concluded that the product of the size of the search light mirror and the focal length of the receiving system (the aperture of which

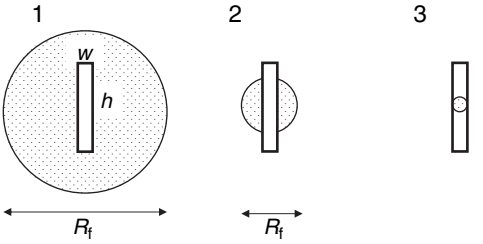

Fig. 7.60. Focusing the image of a retro-reflector or lamp on the spectrometer entrance slit there are three regimes: (1) For w, $h < Rf$, the radiation flux entering the spectrometer will be essentially independent of L (except for extinction); (2) For $w < Rf < h$ the radiation flux is approximately $\propto L^{-1}$; (3) If $Rf < w$, h, the radiation flux is approximately $\propto L^{-2}$

matches the aperture of the spectrometer used) should be chosen as sufficiently large as to allow the system to be in regime 1. Table 7.12 gives examples of the quantities derived earlier. Data are evaluated for typical DOAS systems with radii of search light and receiving telescope mirrors $r = R = 0.15\,\text{m}$, focal length of the search light mirror, $f = 0.3\,\text{m}$, and focal length of the telescope mirror $F = 1.5\,\text{m}$. Further assuming entrance slit dimensions (width w by height h) of 0.05 by 0.2 mm, the light paths for regimes 1–3 are obtained:

Regime 1: $L <$ about 2000 m
Regime 2: $2000 < L <$ about 9000 m
Regime 3: $L >$ about 9000 m

As seen in Table 7.12, the total loss factor from lamp output to the detector is close to 10^{-12} in the case of a optomechanic scanning device with a photomultiplier detector. The total number of photons per second and spectral interval (assuming a division of the spectrum in 400 intervals) reaching the detector can be estimated as follows: A 450-W Xe-arc lamp emits about 2.5 W, corresponding to $dN_0/dt \approx 6 \times 10^{18}$ photons per second, in the form of light in the spectral range 440–460 nm (Canrad-Hanovia). Taking the above loss factor from Table 7.12, about $dN/dt \approx 6 \times 10^6$ photoelectrons per second and spectral interval of 0.05 nm width are registered. This figure corresponds to a shot noise limit of about $4 \times 10^{-4}\,\text{s}^{-1/2}$ (1σ).

7.12 Software Controlling DOAS Instruments

The operating and evaluation software of a state-of-the-art DOAS system is a very essential part of the system; it is at least comparable in complexity to the hardware. The tasks of the DOAS operating software include:

(a) Record and store the spectra and associated information (meteorological data such as air pressure and temperature required to convert measured concentrations to mixing ratios).

Table 7.12. Light losses in a long path spectrometer system (10-km light path) using a 'slotted disk'-type optomechanical scanner

Optical element/process		Loss factor (optomechanical scanner)	Loss factor (multi-element solid state detector)
Light source into beam	x_1	0.08	0.08
Geometric losses ($\alpha = 10^{-3}$ radian, $R_b = 17\,m$)	x_2	3×10^{-4}	3×10^{-4}
Atmospheric attenuation (Mie and Rayleigh scattering)		0.2	0.2
Entrance slit		1.0	1.0
Spectrograph losses		0.2	0.2
Dispersion (fraction of total intensity received by individual pixel)		5.0×10^{-3}	5.0×10^{-3}
Multiplex losses (400 channels)		2.5×10^{-3}	1.0
Detector quantum efficiency		0.2	0.4
Total loss factor	I_{tot}	1.2×10^{-12}	10^{-9}
Total number N of photoelectrons recorded per pixel and second		$\approx 10^5$	$\approx 10^8$

(b) Cycle through measurement sequences (e.g. take atmospheric spectra, background spectra, and dark current, see Sect. 7.14) and calculate the true atmospheric spectra (see Chap. 8). Make measurements in different wavelength regions, switch to different light paths or observation geometries, etc.

(c) Align optics. For instance, in long-path systems the telescope has to be precisely pointed at the light source or retro-reflector array.

(d) Evaluate spectra and display trace gas concentrations following the principles outlined in Chap. 8. This is the most complex task, and is frequently performed off-line.

(e) Perform auxiliary functions, including calculation of sun and moon positions (e.g. SZA). Support wavelength calibration and instrument function determination procedures.

Table 7.13. Software packages developed for acquiring spectra and DOAS evaluation

Designation	Operating system	Functions	Remark	Reference
MFC	DOS	Acquisition, storage, instrument operation, evaluation		Gomer et al., 1995
WINDOAS	WINDOWS	Evaluation only		Fayt et al., 1992
XDOAS	Linux	Acquisition, storage, instrument operation, evaluation	Adoption of MFC to Linux	Grassi pers. comm., 2003
DOASIS	WINDOWS	Acquisition, storage, instrument operation, evaluation	Formerly 'WINDOAS Heidelberg'	Leue et al., 1999; Kraus, 2005

Several software packets have been developed to perform some or all of the above tasks, as summarised in Table 7.13. In addition, there are several software systems which have been developed for use by individual laboratories and suppliers of commercial DOAS systems.

7.13 Optimising DOAS Instruments

A central question of any DOAS system concerns the light throughput, i.e. the question how the amount of light reaching the detector can be maximised under the given boundary conditions.

The detection limit for a particular substance can be calculated according to (6.9), if the differential absorption cross-section, the minimum detectable optical density D'_0, and the length of the light path are known. In several applications, however, the goals of maximising light throughput and light path length can contradict each other, as is detailed below.

In general, D_0 is determined by: (1) Photoelectron statistics (shot noise), which is a function of light intensity only and (2) by any other noise sources including detector noise, induced 'background absorption structures', or 'optical noise' (see Sect. 7.3). This second class of noise sources, summarised in B, is on the order of $N/S \approx 10^{-4}$ for typical DOAS systems with solid state detectors or OSDs (see Sect. 7.6). Photoelectron shot noise is proportional to $N^{-1/2}$, where N is the total number of photons recorded around the centre

of the absorption line during the time interval t_m of the measurement. The number of photoelectrons N is related to the power P received by a detector pixel.

$$N = \frac{P \cdot t_m \cdot \eta \cdot \lambda}{hc}, \tag{7.49}$$

where η denotes the detector quantum efficiency (at the given wavelength λ), c the speed of light, and h Planck's constant. Thus, the minimum detectable optical density D_0 will be proportional to:

$$D_0 \propto \sqrt{\frac{1}{N} + B^2}. \tag{7.50}$$

If sufficient light is available (which is rarely the case), D_0 is limited by B (Platt et al., 1979; Platt and Perner, 1983). Using N from Table 7.12, ideally an integration time on the order of minutes for optomechanical detectors and around 1 s for array detectors would be sufficient to make $N^{-1/2} \approx$ B.

While for a given minimum detectable optical density the detection limit improves proportionally to the length of the light path, the actual detection limit, will not always improve with a longer light path. This is because with a longer light path the received light intensity $I(\lambda)$ tends to be lower, increasing the noise associated with the measurements of $I(\lambda)$, and thus increasing the minimum detectable optical density. More details are given in Sect. 7.13.1.

7.13.1 Optimum Light Path Length in Active DOAS Systems

An important consideration in the practical application of DOAS is the length (L) of the light path chosen. The value of L has a large influence on the performance of the system:

1. The optical density due to light absorption by trace gases (at a given concentration) is directly proportional to L.
2. The intensity (I) received from the light source generally decreases with the length of the light path (the decrease dI/dL will depend on the details of the setup and L itself, as discussed below). In addition, for folded paths (DOAS systems coupled to multi-reflection cells), I decreases with increasing L.
3. The volume over which the trace gas concentration is averaged (for long path systems) is proportional to L.
4. Long light paths (folded or unfolded) make the DOAS system more vulnerable to extinction by aerosol, haze, or fog.

In the following, we make a few simple considerations which may clarify this relationship and also allow the derivation of detection limits.

For a typical DOAS system, as described in Sect. 7.11, there are no geometrical light losses of path lengths upto ∼2 km. However, in addition to geometrical light losses, light attenuation due to atmospheric absorption, as

well as to scattering affect the magnitude of the received light signal, is described by:

$$I_{\text{received}} = I_{\text{source}} \exp[-\mathrm{L}(\Sigma(\sigma_{\mathrm{i}}(\lambda)c_{\mathrm{i}}) + \varepsilon_{\mathrm{R}}(\lambda) + \varepsilon_{\mathrm{M}}(\lambda))], \tag{7.51}$$

or simply:

$$I_{\text{recieved}} = I_{\text{source}} \cdot \exp\left(-\frac{L}{L_0}\right), \tag{7.52}$$

where the absorption length L_0 reflects the combined effects of broadband atmospheric absorption, Mie and Rayleigh scattering, as given in the second term of (5.7), i.e.:

$$L_0 = \frac{1}{\sum\limits_i (\sigma_{\mathrm{i}0}(\lambda)\, c_{\mathrm{i}}) + \varepsilon_{\mathrm{R}}(\lambda) + \varepsilon_{\mathrm{M}}(\lambda)}. \tag{7.53}$$

The noise level of a photodetector signal is essentially dependent on the number of photons received and thus is proportional to the square root of the intensity. The signal-to-noise ratio of a DOAS system as a function of the light path length L can be expressed as:

$$\frac{D'}{N} \approx L \cdot G(\lambda) \cdot \exp\left(-\frac{L}{2L_0}\right), \tag{7.54}$$

where $G(\lambda)$ is constant (regime 1), $G(\lambda) = L^{-1}$ (regime 2), or $G(\mathrm{i}) = L^{-2}$ (regime 3), respectively, as defined in Sect. 7.11 (see also Fig. 7.60). Relationship (7.54) yields optimum D'/N ratios for light path lengths of $L = 2L_0$ (regime 1), $L = L_0$ (regime 2), or a boundary maximum at the shortest light path (regime 3). While there are no lower limits for L_0 in the atmosphere (consider, for example, fog), the upper limits are given by Rayleigh scattering, and the scattering by atmospheric background aerosol, which indicate optimum light path lengths ($2L_0$) in excess of 10 km for wavelengths above 300 nm (see Table 4.6).

Another point to consider is the width G of the absorption line (or band). At a given spectral intensity of the light source $N(\lambda)$, the light intensity around the line centre will be $N(\lambda)d\lambda \approx N(\lambda)\ \Gamma$ (in photons per nanometre and second). Thus D_0 becomes:

$$D_0 \propto \sqrt{\frac{1}{N(\lambda) \cdot \Gamma \cdot t} + B^2}. \tag{7.55}$$

From (7.55), it becomes clear that the detection of a spectrally narrow absorption line requires a proportionally higher spectral intensity of the light source (see Sect. 7.9.2).

7.13.2 Optimum Spectral Resolution

For a given (grating) spectrometer, the light throughput varies in proportion the square of the spectral resolution, as shown in Sect. 7.5.4 (here expressed as the width Γ_0 of the instrument function in nm). Thus, the light intensity at the output becomes:

$$I \approx I_i \cdot {\Gamma_0}^2. \tag{7.56}$$

The 'signal' in the spectrum is the differential optical density D', which is (for a given species, wavelength, and light path) proportional to the concentration.

In the case of shot noise limitation, the minimum detectable optical density D_0 in the spectrum is inversely proportional to the square root of I, thus:

$$D_0 \sim \frac{1}{\sqrt{I}} \sim \frac{1}{\Gamma_0}. \tag{7.57}$$

In general, the signal as a function of the spectral resolution will vary proportional to the differential absorption cross-section as a function of resolution $\sigma'(\Gamma_o)$. Figure 7.61 (upper panel) shows an example for several bands of NO_2 in the visible spectral region. In principle, $\sigma'(\Gamma_0)$ can be an arbitrary function of Γ_0, which decreases with increasing Γ_0. In the example of Fig. 7.61, $\sigma'(\Gamma_0)$ can be approximated as a linear function:

$$\sigma'(\Gamma_0) \approx \sigma'_0 \, (1 - a\Gamma_0), \tag{7.58}$$

where a is a constant (in the example of Fig. 7.61; $\approx 2.4\,\mathrm{nm}^{-1}$). Thus, in this special case, the signal-to-noise ratio becomes:

$$\frac{D'}{N} = \sigma'_0 \cdot (1 - a\Gamma_0) \cdot \Gamma_0 \propto \Gamma_0 - a \cdot \Gamma_0^2. \tag{7.59}$$

The optimum D'/N is thus obtained at the resolution:

$$\frac{d}{d\Gamma_0}\frac{D'}{N} = 1 - 2a\Gamma_0 = 0 \text{ or } \Gamma_{0,\mathrm{opt}} = \frac{1}{2a} \approx 1.2\,\mathrm{nm}\ (a \approx 2.4\,\mathrm{nm}^{-1}, \text{ see Fig. 7.61}) \tag{7.60}$$

Note that, in general, the instrument function $H(\lambda)$ will not be of Gaussian shape. The spectrum of a given trace species (expressed as optical density), as seen by a particular spectrometer, is obtained by convoluting the true spectrum $D_\mathrm{T}(\lambda)$ with the instrument function $H(\lambda)$, as described in Chap. 6.

7.13.3 Optimum Measurement Time

The number of photons recorded in a DOAS spectrum is proportional to the integration time (either of a single detector exposure or as a sum of several co-added spectra). Consequently, the noise in the spectrum (and thus the minimum detectable optical density D_0) will be reduced proportionally to the square root of the integration time, see (7.55). This will not continue

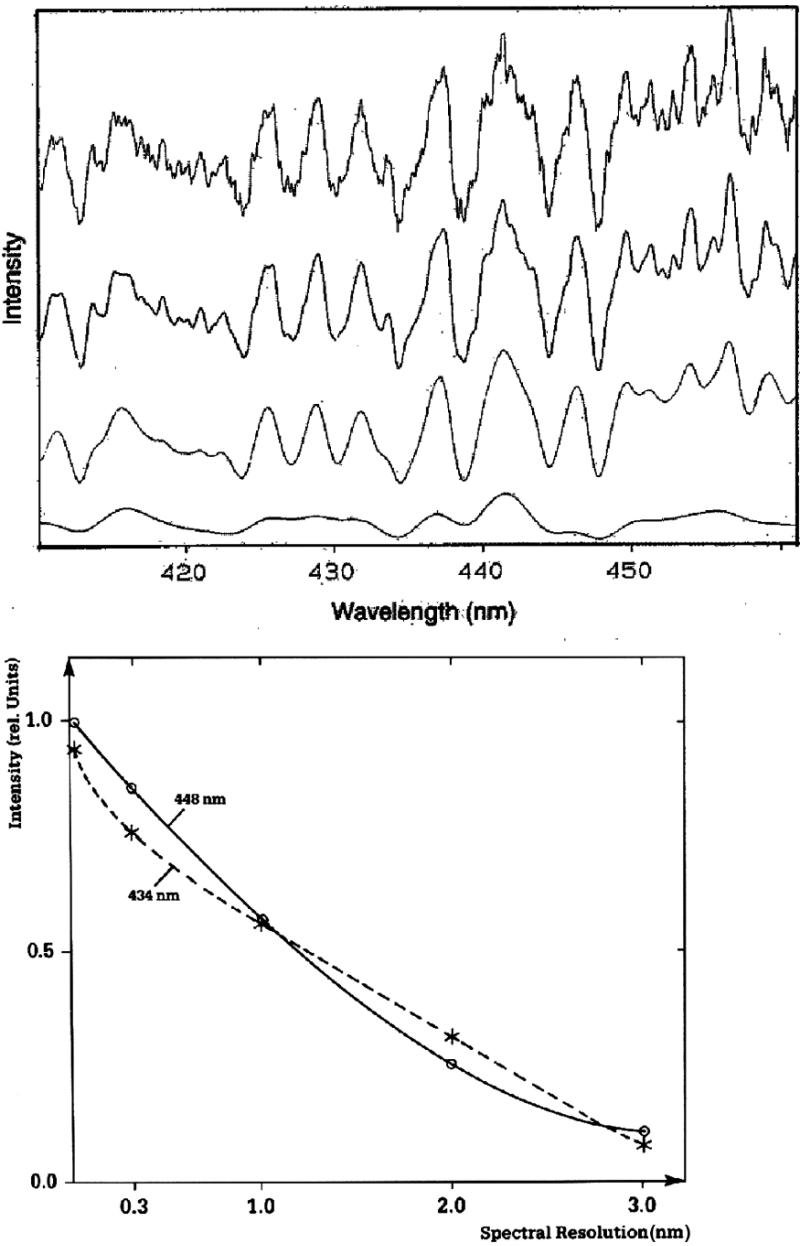

Fig. 7.61. Absorption cross-section of NO_2 as a function of spectral resolution, here expressed as the FWHM Γ_0 of the instrument function $H(\lambda)$. **Upper panel**: Absorption spectrum for different values of the spectral resolution Γ_0, from top to bottom $\Gamma_0 = 0.01$, 0.1, 1.0, 3.0 nm; **Lower panel**: Differential optical density for constant NO_2 column density as a function of the spectral resolution Γ_0. There is a nearly linear decay of the optical density as the spectral resolution is reduced, i.e. increasing Γ_0 (adapted from Platt, 1994)

indefinitely, but reach a system dependent minimum noise level B, which is determined by other noise sources in the system. An example for a typical active DOAS system (Tuckermann et al., 1997) using a diode array detector is shown in Fig. 7.62. With increasing signal (i.e. photoelectrons accumulated, given as total binary units), the noise levels are reduced proportionally to the square root of the signal. However, from $\sigma^2 \approx 10^{-8}$–10^{-7} the noise will not be further reduced. This observation shows that there are additional noise sources which are not signal dependent. Under laboratory conditions with a fixed optical setup, noise levels of at least two orders of magnitude lower are reached at sufficiently long integration times. This observation indicates that the noise source dominating long integrations times is not due to electronic noise but is more likely due to optical interference effects (Stutz, 1996; Stutz and Platt, 1997) or processes in the light source. The remaining noise is therefore called 'optical noise'. Obviously, it is of little use to continue a measurement to

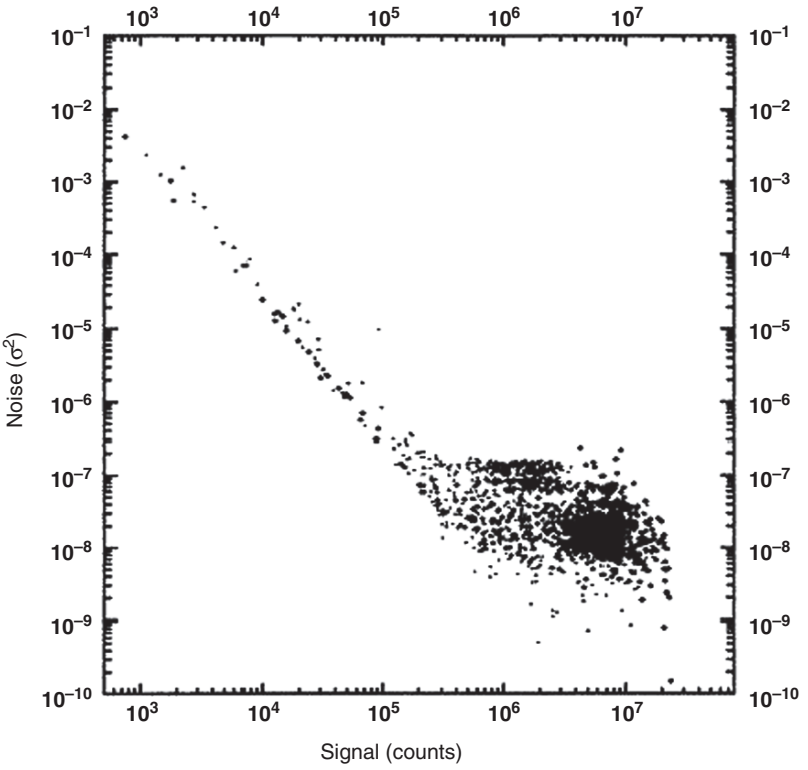

Fig. 7.62. Square of the noise level (σ) as a function of measurement time (log–log scale). Up to a certain limit, there is a linear decrease of σ^2 with the number of photoelectrons recorded (here 1 count signal $\simeq$ 1000 photoelectrons) (adapted from Tuckermann, 1996)

the point where the photoelectron-shot noise becomes much smaller than the combined effect of all other noise sources in the system.

7.14 Measurement Process Control

Like most techniques, DOAS measurements require a number of additional parameters besides the recording and evaluation of trace gas absorption spectra. Several supporting systems are needed for DOAS measurements, particularly if automatic operation is desired. These systems include mechanical actuators for optical alignment of the light path and change of measurement modes, recording of auxiliary parameters required for the interpretation of the measurements (length of the light path, air density, etc.), and monitoring of instrument performance.

In this section, we present a series of 'typical' measurement procedures. Generally, these procedures involve taking measurement spectra and a series of auxiliary spectra (background, dark current, direct light source, calibration, and sometimes scattered sunlight spectra).

7.14.1 Active DOAS Systems – Standard Approach

A complete DOAS measurement using radiation from an artificial light source encompasses taking a series of several different spectra. Here, we give an example for a system using a diode array detector (see e.g. Fig. 7.49), but other arrangements follow procedures similar to those outlined in Fig. 7.63. For a complete DOAS measurement, the following spectra are usually recorded:

1. Atmospheric raw spectrum [ARS, denoted $I_{\mathrm{M}}(i)$]. This is the spectrum of atmospheric absorbers (trace gases) superimposed on a lamp (light source) spectrum. Usually, several individual spectra (N_{M}) with integration time T_{M} are co-added.
2. Lamp intensity spectrum [LIS, $I_{\mathrm{L}}(i)$]. This spectrum is recorded by admitting direct light from the lamp to the spectrometer (using some optics to 'bypass' the light path).
3. Dark current (and electronic offset) spectrum [$I_{\mathrm{D}}(i)$]. This spectrum is taken with no light admitted to the detector e.g. by closing a shutter in front of the entrance slit of the spectrometer. By normalising the sum of N_{D} co-added dark current spectra, we obtain $I_{\mathrm{D1}}(i) = I_{\mathrm{D}}(i)/N_{\mathrm{D}}$.
4. A background spectrum [$I_{\mathrm{B}}(i)$] with integration time T_{B} is sometimes required. Since sunlight scattered into the receiving optics might disturb the measurements, a scattered sunlight or background spectrum is taken by blocking the lamp.
   As a result of steps 1–4, a true atmospheric spectrum I(i) is calculated from the above series of spectra (N_{B} and N_{L} denote the numbers of co-added background and LIS, respectively):

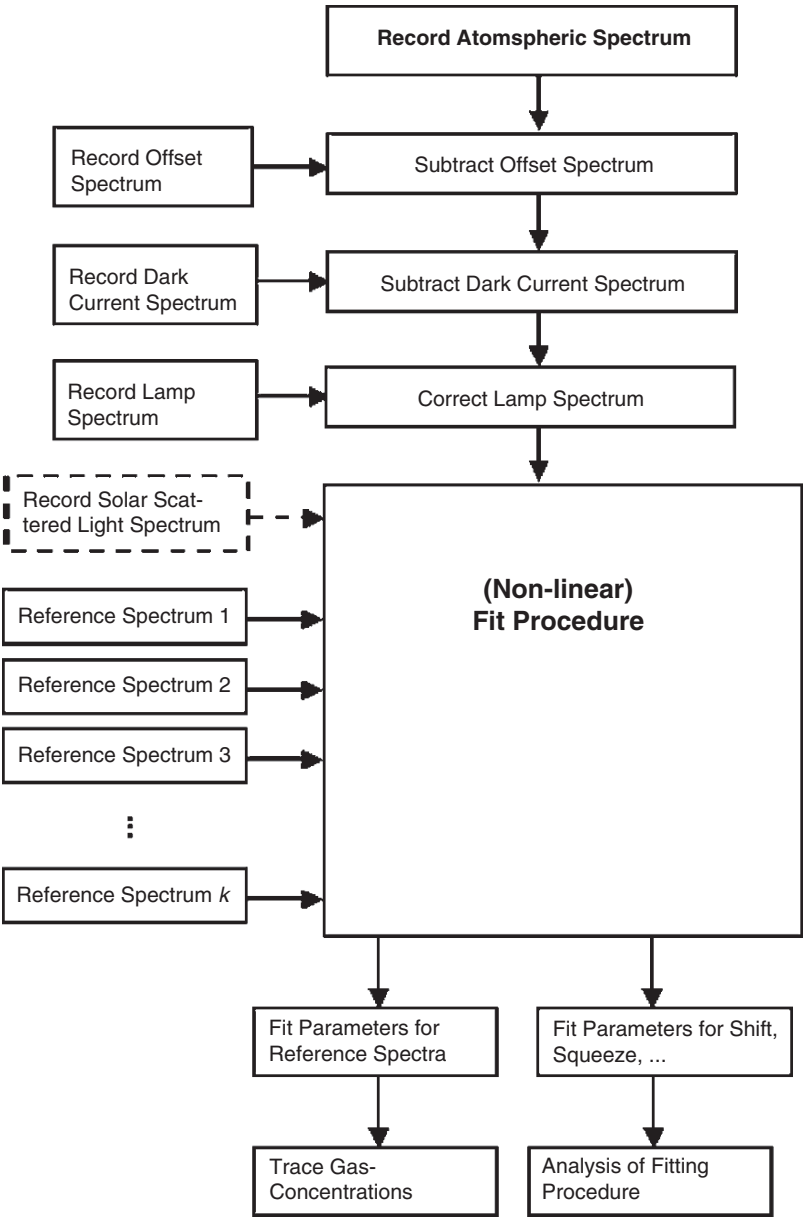

Fig. 7.63. Flowchart of a typical active DOAS measurement and evaluation procedure

$$I(i) = [(I_{\mathrm{M}} - N_{\mathrm{M}} \cdot I_{\mathrm{D1}}) - T_{\mathrm{M}}/T_{\mathrm{B}} \cdot (I_{\mathrm{B}} - N_{\mathrm{B}} \cdot I_{\mathrm{D1}})] \cdot (I_{\mathrm{L}} - N_{\mathrm{L}} \cdot I_{\mathrm{D1}})^{-1}. \quad (7.61)$$

Note that background spectra need not always be taken and compensated for (for instance, at night or at wavelengths below 300 nm where scattered sunlight levels are low). Also, while LIS are always required to compensate for diode-to-diode sensitivity variations (see Sect. 7.6.3), it might not be necessary to take one with each ARS.
In the final steps, the atmospheric spectrum $I(i)$ is evaluated for absorption signatures due to atmospheric gases.

5. A non-linear least squares fit of a series of reference spectra is performed. The reference spectra are usually taken from the literature, and must be adapted to the instrument function of the spectrometer used. This procedure is described in Chap. 8.
6. The resulting fit parameters describing the optical density of the reference spectra are used to calculate the respective trace gas column densities (and their uncertainties).
7. The desired trace gas concentrations are derived by dividing by the length of the optical absorption path. If desired, the concentrations can be converted to mixing ratios.
8. The fit parameters for 'shift' and 'squeeze' of the spectra, which are not directly relevant for deriving trace gas column densities or concentrations, can be used to improve the estimate of the uncertainties and to give general information about the quality of the measurement.

7.14.2 Active DOAS Systems – MCST

A different approach in removing the diode sensitivity variation than taking LIS is the Multichannel Scanning Technique, MCST, introduced by Knoll et al. (1990) (see also Brauers et al., 1995; Stutz, 1996; Alicke, 2000). The basic idea of the MCST is the combination of a multi-channel detection system (PDA) with the scanning technique generally used to cover a larger spectral region with a single-channel detection system. A series of (typically ≈10) ARS $[I_{\mathrm{MM}}(i)]$ is taken and stored. The individual spectra are successively shifted in wavelength (for instance by slightly rotating the grating) in such a way that the spectral information is essentially smoothed out when the ARS are co-added (after subracting I_{D}) to give LIS $[I_{\mathrm{LM}}(i)]$. Note that the wavelength difference must be smaller than any spectral structure like absorption bands; otherwise this structure not only remains in the sum spectra, but would also be duplicated near itself. Now, each ARS is divided by the obtained LIS and digitally shifted back to the same wavelength position (for instance of the first ARS in the series) to obtain a true atmospheric spectrum (according to (7.61), with $I_{\mathrm{MM}}(i)$ instead of $I_{\mathrm{M}}(i)$ and $I_{\mathrm{LM}}(i)$ instead of $I_{\mathrm{L}}(i)$). The advantage of the MCST is that the diode-to-diode sensitivity variations are even more precisely eliminated, since spectra taken to determine these variations are recorded

under precisely the same conditions as the ARS. In addition, measurement time is saved, since no separate LIS have to be taken.

7.14.3 Passive DOAS Systems

In passive DOAS systems the primary spectrum consists of absorption features of atmospheric molecules superimposed on a solar (or stellar) spectrum. Raw spectra of zenith scattered skylight (or moonlight or starlight) in the UV/visible are dominated by strong Fraunhofer lines with (in the near UV) optical densities sometimes exceeding unity. Thus, in order to make useful determinations of the weak absorption features of the trace gases in the earth's atmosphere (with optical densities on the order of 10^{-3}), the very accurate removal (with residuals of below 10^{-3} of its initial strength) of the solar spectral structure (LIS) is an indispensable prerequisite. Unlike the case of the artificial light DOAS, the direct solar spectrum is not accessible for ground-based instruments. Therefore, another approach is used:

In order to remove the Fraunhofer structure, spectra taken at different zenith angles of the observed celestial body, ϑ_1 and ϑ_2, are ratioed. The corresponding air mass factors are $A(\vartheta_1)$ and $A(\vartheta_1)$. The observed trace gas slant columns S are $\mathrm{S}(\vartheta_1) = V \cdot A(\vartheta_1)$ and $\mathrm{S}(\vartheta_2) = V \cdot A(\vartheta_2)$, where V is the vertical trace gas column. We obtain for the ratio of the measured optical densities:

$$\begin{aligned}\frac{D_2}{D_2} &= \frac{e^{-\mathrm{S}(\vartheta_2)\cdot\sigma}}{e^{-\mathrm{S}(\vartheta_1)\cdot\sigma}} = e^{-\sigma\cdot[\mathrm{S}(\vartheta_2)-\mathrm{S}(\vartheta_1)]} \\ &= e^{-\sigma\cdot V\cdot[A(\vartheta_2)-A(\vartheta_1)]}.\end{aligned}$$

In other words, the ratio of the optical densities is the optical density based on the difference in the air mass factors (see Chap. 9). For the slant column $\mathrm{S_D} = V\ [A(\vartheta_2) - A(\vartheta_1)]$ the term 'differential slant column' (DSC) is sometimes used, which should not be confused with the use of the term 'differential' in the context of DOAS evaluation of optical spectra.

A complete scattered light DOAS measurement thus consists of taking the following spectra (Again we give an example for a system using a diode array detector):

1. Two ARS (denoted $I_{\mathrm{M1}}(i)$ and $I_{\mathrm{M2}}(i)$) at different (solar) zenith angles. For each spectrum several individual spectra (N_{M}) with integration times T_{M} are usually co-added.
2. Dark current (and electronic offset) spectrum $[I_{\mathrm{D}}(i)]$. By normalising the sum of N_D co-added dark current spectra, we obtain $I_{\mathrm{D1}}(i) = I_{\mathrm{D}}(i)/N_{\mathrm{D}}$.

The procedure is also outlined in Fig. 7.64.

7.14.4 Off-axis Scattered Sunlight DOAS Systems

Off-axis DOAS measurements make use of scattered light spectra recorded at non-zero angles β between zenith and observation direction. If observations

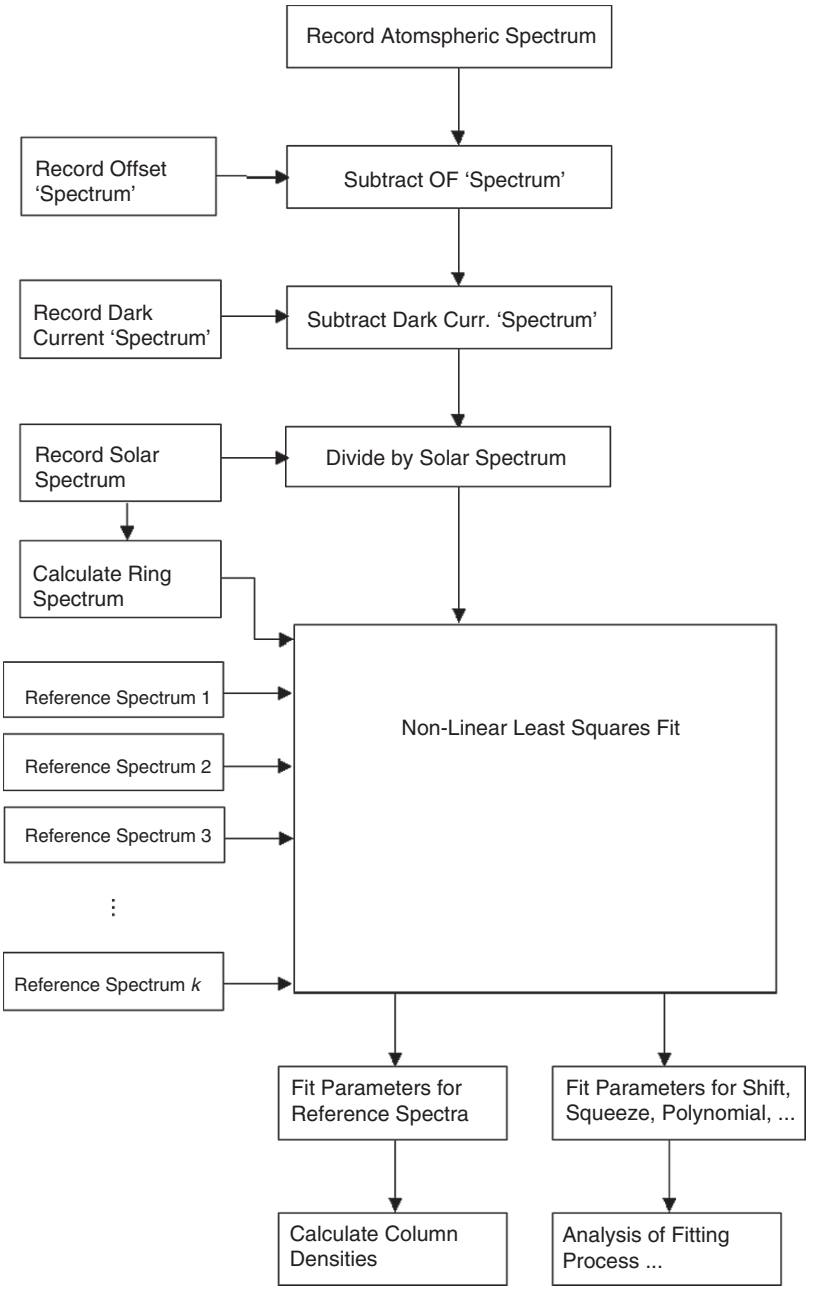

Fig. 7.64. Flowchart of a typical passive DOAS measurement and evaluation procedure.

are made at only one angle β, the difference to ZSL-DOAS lies in a different (usually more complex) air mass factor calculation, and essentially the same procedures for removing the Fraunhofer structure are applied.

On the other hand, observations at several off-axis angles $\beta_1 \ldots \beta_k$ can be made. Now, there are two variable angles β and ϑ. Generally, the absorption due to gases in the upper atmosphere (stratosphere) increases with increasing SZA ϑ, while the absorption due to gases in the lower atmosphere (boundary layer) strongly increases with higher off-axis angles β (see Chap. 9). Similar to the approach using different SZAs ϑ, the Fraunhofer structure can also be removed by ratioing spectra taken at different off-axis angles.

7.15 Mechanical Actuators

The DOAS operating procedures described in Sect. 7.14 require a number of supplemental data, such as offset, dark current and other spectra. These data can be measured manually, but will usually be acquired in an automatic sequence under computer control. In order to switch between the different measurement modes e.g. recording atmospheric spectra, dark current, or observing at different elevation angles, mechanical actuators are needed. In addition, in active DOAS systems (using artificial light sources), alignment of the receiving telescope is often required (due to mechanical instabilities of the optical setup, but also due to diffraction of the light path due to temperature gradients, and thus density and index of refraction, gradients in the atmosphere). These changes in the optical configuration required for the different measurement modes and the optical alignment tasks are usually performed by electrical motors coupled to appropriate mechanics like translation stages. When defined, absolute positions need to be reached. For example, when pointing a telescope to a retro-reflector array. Stepper motor-driven actuators are frequently the devices of choice, although DC-motor–encoder combinations might become important in the future.

For a typical active (artificial light) DOAS system, actuators are usually part of the system:

- 'Short circuit' optics which are moved into the light beam record the lamp emission spectrum.
- A shutter allows the recording of the dark-current spectrum.
- Motorised setting of the spectrometer wavelength allows measurement of spectra in several spectral intervals.
- A filter actuator inserts spectral filters (i.e. to block second order spectra or to reduce stray light) into the optical path.
- Actuators for alignment of the telescope pointing direction (azimuth and elevation) are usually required.
- Alignment of the telescope focus can be motorised in order to accommodate largely different light path lengths.

In summary, about six to seven or more actuators might be needed in a typical artificial-light source DOAS system.

For a typical passive (scattered-sunlight) DOAS system, fewer (about three to four) actuators are required:

- A shutter allows the recording of the dark-current spectrum.
- Motorised setting of the spectrometer wavelength allows measurement of spectra in several spectral intervals.
- A filter actuator inserts spectral filters (i.e. to block second order spectra or to reduce stray light) into the optical path.
- An actuator for aiming of the telescope, usually one but sometimes two axes (azimuth and elevation), may be required for multi-axis measurements.

7.15.1 Stepper Motors

Stepper motors move in precisely known increments. Typical incremental angles (or step sizes) are 1.8° (or 200 steps per revolution), but a wide range of different step sizes are available. Special drive electronics ensures that the correct current waveforms are supplied to the motor windings. Modern drive electronics also frequently support fractional steps; i.e. by driving the motor windings by different relative currents the steps can be further divided. Today, many drivers allow a 'half-step' mode, but much smaller 'micro-steps' are also sometimes possible.

Under computer control, such a motor can perform a precisely determined motion pattern. The positions of the motor are repeatable, for instance, different filters mounted on a wheel attached to the motor axis can be selected without further hardware, provided the initial position of the motor is known. This is usually ensured by driving each actuator to a limit switch (and thus to a known mechanical position) during the set-up period of the instrument. In addition, several different telescope pointing directions (i.e. towards several retro-reflectors or light sources) can be selected under software control when azimuth and elevation of the telescope are actuated by stepper motors.

If further mechanical gears are attached to a stepper motor slackness in the mechanics may be present. This is caused by thread clearance in a translation stage. A consequence is that the actuator will reach a different position when approached from different directions of motion. A possible solution is to always make the final move in the same direction, for instance in 'forward direction', which means that moving in the 'backward' direction consists of two phases: first, move backwards by the desired number of steps plus a number of n extra steps, then move 'forward' by n steps.

Disadvantages of stepper motors include their relatively low speed, high cost, and the possibility of 'loosing steps', which is usually not directly detectable by the driving electronics. Furthermore, there might be electrical interference from the rapidly changing currents in the motor windings (the

stepper motor is an inherently 'digital device'), for instance with the detector electronics. This problem can usually be avoided by not operating stepper motors during the actual measurement i.e. the recording of optical spectra. However, it should be noted that many commercial stepper motor drivers use a 'switch mode' approach to limit the current to the motor windings. Therefore, although the motor is not moving and the currents to the windings should be 'static', there might be high frequency modulated (usually in the 10 kHz range) currents on the windings. This is difficult to avoid in micro-step mode, but in full or half-step mode, when currents are off or have the same absolute magnitude, a series resistor to the winding might be chosen to limit the current to a point just below the 'desired' current of the motor driver.

In order to minimise the problems of losing steps, a motor should be selected that has sufficiently large torque for the particular application. Additionally, the motor should be operated at a sufficiently low speed.

Stepper motors have a recommended 'starting speed' (=step frequency) and a 'maximum speed'. These numbers are given by the manufacturer for the motor alone and are obviously smaller in any practical application where the motor shaft is connected to additional mechanical elements (like lead screws) which increase the inertia of the motor armature. Also, in practice the motor has to drive a load. A simple approach involves always operating the motor at a same margin below the starting speed. A more sophisticated approach, allowing faster motor operation, starts the motor at its starting speed, followed by a ramp of the step frequency up to the maximum speed. Towards the end of the motion, the frequency is ramped down to the starting speed again. In either case, care has to be taken to avoid motor resonance frequencies. Motor resonance effects can be the cause for errors that are difficult to diagnose later. Motor resonance frequencies are given by the manufacturer, but they apply to the motor alone and will be changed by added load. Note that frequently motor resonance is less pronounced if half-step mode rather than full-step mode is applied.

7.15.2 Other Actuators

Despite their limitations, stepper motors are most commonly used to drive actuators in DOAS systems. Alternatives include DC motors with or without angular encoders. Given a suitable drive electronics encoder, motors can perform almost like stepper motors, with the advantage of not missing steps (since the encoder always allows verification of the motor motion). However, resolution down to a single step is usually not possible.

In some cases, encoders might not be needed; for instance, the position of different filters does not need to be very precise, and thus DC motors with a series of position switches might be sufficient.

For small (linear) displacements piezo actuators might be useful. This type of actuator has seen rapid technological development in recent years.

7.16 Information Needed for Later Analysis

Besides the trace gas column density calculated from the spectra, additional information is required in order to use the data in an orderly way. This information includes obvious data:

- Site of measurement (i.e. geolocation, typically latitude and longitude of the measurement). Obviously, this information will always be required for measurements from mobile platforms (e.g. satellites, aircraft, or ships), but it is good practice to record this information for fixed sites.
- Time and date of measurement.
- Information on type of measurement (active, passive, long-path DOAS, ZSL, multi-axis, etc.).
- Light-path identification (for active systems), length of light path
- Viewing direction (for off-axis DOAS measurements), azimuth and elevation
- Solar (lunar) zenith angle (this information can also be calculated from time, date, and location of the measurement)
- Information on air density. This information is needed to convert the trace gas concentrations into mixing ratios. The air density can be readily determined by recording atmospheric pressure and temperature.
- Technical information, including number of pixels per spectrum, type of light source, type of spectrometer, grating used, type of detector, optical filter, wavelength, etc.